Ring Imaging Cherenkov Detectors and the Rare Decay $B_d \to K^{*0}\mu^+\mu^-$ at LHC*b*

Thomas Blake

Blackett Laboratory
Imperial College London

A thesis submitted for the degree of Doctor of Philosophy
in the Department of Physics at Imperial College London

August 26, 2008

Abstract

The LHCb experiment is one of four experiments at the Large Hadron Collider. It is the next generation of heavy flavour experiment, designed to study CP violating processes and rare decays in the B system and will benefit from the large b-quark production cross-section in $\sqrt{s} = 14\,\mathrm{TeV}$ proton-proton collisions. This will enable LHCb to record large numbers of events even for rare decay modes such as $B_d \to K^{*0}\mu^+\mu^-$, with a branching fraction $\mathcal{B}\left(B_d \to K^{*0}\mu^+\mu^-\right) = 1.22^{+0.38}_{-0.32} \times 10^{-6}$, that is discussed in this thesis.

This thesis is divided into two parts. The first part focuses on the photon detectors of LHCb's Ring Imaging Cherenkov (RICH) detectors and their associated front-end electronics, discussing measurements made on these photon detectors during laboratory testing and culminating in a series of beam tests. The beam tests measured the performance of a $1/10^{th}$ scale prototype RICH detector, providing an estimate for the combined efficiency of the HPD's binary readout and charge collection of $\varepsilon_{collection} \times \varepsilon_{readout} = 82 \pm 3\%$.

The second part of this thesis reports on LHCb's sensitivity to the decay $B_d \to K^{*0}\mu^+\mu^-$ in a Monte Carlo study with one nominal year ($2\,\mathrm{fb}^{-1}$) of data. With this data set (of 7000 events) LHCb should be able to make, for the first time, a precision measurement of the kinematic distribution of the particles in the decay that in many new physics models can have large departures from the Standard Model (SM) prediction. Particular attention is paid to the forward-backward asymmetry of the muons which changes with the invariant mass of the muon pair and crosses zero at a well defined value with small theoretical error in the SM. LHCb's precision on this zero crossing point is estimated at $\pm 0.43\,\mathrm{GeV}^2$.

Acknowledgements

During the past three years I have had the pleasure of working on a number of different aspects of the LHC*b* experiment. I spent much of the first two years involved with the hardware of the RICH, testing photon detectors at CERN and taking part in three different beam tests. Two of these in Frascati, near Rome, in Italy. I was also involved in the field mapping of the LHC*b* dipole magnet. It's amazing how much the experimental hall has changed since then. Much of this time was spent at CERN and the opportunity to travel and work outside the UK is something I will always be grateful for. The latter part of my PhD has been spent back in London performing the Monte Carlo studies presented in Chapters 7 and 8. As part of this work I both contributed code to the software framework and have been responsible for the generation of a large background data set. Undoubtedly much of this could not have been achieved without a lot of help and patient guidance. A lot of thanks are due, not in the least to Imperial College and PPARC/STFC, but I would like to extend special thanks to the following:

My supervisor, Dave Websdale for all his advice over course of my PhD . The other members of the Imperial College LHC*b* group, especially Peter Dornan, Ulrik Egede and Patrick Koppenburg for all your help.

Thierry Gys, Naoko Kanaya, Didier Piedigrossi and Gianluca Aglieri Rinella for their help with the HPD testing.

Ann van Lysebetten and Richard Plackett for their work on the RICH 1 magnetic field measurements. It's surprising how fast you can get out of the shielding box if you really have to.

Marco Adinolfi, Paolo Baesso, Tito Bellunato, Jeremy Dickens, Ulrich Kerzel, Mitesh Patel, Andrew Powell, Steve Wotton and Ken Wylie for their help and advice, but especially for keeping five weeks of beam tests fun.

My friends and fellow students for keeping me sane. You know who you are.

Finally, my parents, without your encouragement I wouldn't be where I am today.

Contents

List of Figures

List of Tables

Chapter 1

Introduction

The Large Hadron Collider (LHC) represents the new generation of colliding beam high energy physics accelerator. Located at the CERN accelerator complex, on the Swiss-French border, it will bring two counter rotating proton beams into collision with an un-precedented centre of mass energy of 14 TeV. The four main experiments at the LHC are ALICE, ATLAS, CMS and LHCb. ATLAS and CMS are general purpose detectors, with a cylindrical geometry, designed to make direct searches for new, more massive, particles produced in the collisions. The LHCb experiment, the main focus of this Thesis, is a precision experiment designed to make measurements of matter-antimatter asymmetries (CP violation) and rare decays in the decay of heavy flavour particles, primarily particles containing b-quarks. ALICE is a heavy ion experiment, the successor to STAR and PHENIX at the Relativistic Heavy Ion Collider (RHIC) at the Brookhaven National Laboratory that aims to create a new state of matter (the quark-gluon plasma). Whilst ALICE is running the LHC will swap from colliding intersecting beams of protons to ionised lead atoms. Each of the experiments is designed to test our Standard Model of the Universe on the particle scale and search for physics beyond it.

1.1 Particles and Fundamental Forces

The Standard Model (SM) represents our current understanding of the underlying theory that governs interactions on the particle level. It describes the particles and their interactions through electromagnetism, the weak force (that is responsible for β decay) and the strong force (that binds the nucleus together).

There are the fermions, spin one-half particles that are:

- Leptons: the electron and the heavier muon and tau and their accompanying neutrinos.
- Quarks: the up and down-type quarks that are constituents of the proton and neutron and two heavier families (the charm, strange and the top, bottom).

In the SM, forces are mediated through force carriers, the bosons. These are the photon for electromagnetism, two charged and one neutral massive boson that mediate the weak force and eight gluons from QCD (the strong force). As charged particles are separated the electromagnetic force between them falls ($\propto 1/r^2$), interstingly this is not the case for the strong force. One consequence is that there are no free quarks and instead they come bundled in quark-antiquark pairs or in threes. For example the proton is two up-type quarks and one down-type quark. The final ingredient in the Standard Model is a scalar particle, the Higgs boson. It is responsible for giving mass to the fermions and force-carrying bosons in what would otherwise be a massless theory and is the focus of a large amount of effort at ATLAS and CMS. An overview of the SM theory can be found in Chapter 2.

So far the Standard Model has been remarkably successful but at the same time we know that it is not a complete description of the Universe. It does not include Gravity or produce enough matter anti-matter asymmetry to explain the observable Universe. It provides no dark matter candidate, for which we have evidence from galaxy rotation curves [1]. Finally, there is a range of theoretical arguments for extending the Standard Model, in particular the Hierarchy problem that requires a high level of fine tuning of parameters to avoid divergences in the theory.

1.2 LHCb and Flavour Physics

The violation of both Charge Conjugation (C) and Parity (P) symmetries is one of the conditions[1] for producing a matter anti-matter asymmetry in our Universe [2]. Charge Conjugation is the interchange, for example, of a fermion for its anti-particle counter part. The Parity operator takes a mirror image of a system. If the laws of

---

[1] It is one of the three Sakharov conditions, along Baryon number violation and a breakdown of thermal equilibrium.

nature are insensitive to whether we are dealing with matter or anti-matter then C is conserved, likewise if the theory governing a system is unchanged under the P mirror reversal then we say that P is conserved. Electromagnetism remains unchanged under both the C and P transforms. The V-A (see Chapter. 2) structure of the weak interactions means that C and P are maximally violated. Experimental evidence for this was first observed by Wu et. al. in the β decay of Cobalt 60 [3].

Experimental evidence for violation of the product of the C and P symmetries was first seen in decays of the different mass eigenstates of the K^0 meson (a particle containing a down and a strange-type quark), the K_S^0 and K_L^0 to $\pi^+\pi^-$ [4]. If CP is conserved in the decay then $K_L^0 \to \pi^+\pi^-$ would be forbidden. Experimental evidence for CP violation in B decays from the B-factories (*BABAR* at the PEP-II accelerator and Belle at KEK in Japan) has allowed a detailed picture of CP violation to be built up in the b-quark sector. Unfortunately the level of CP violation is still too small to explain the matter anti-matter asymmetry in the Universe. CP measurements at the LHC will allow a detailed comparison between tree level processes and higher order loop processes. New phases coming from physics beyond the Standard Model can enter into these loops and increase the amount of CP violation in our Universe.

An alternative approach for new physics searches in heavy flavour decays is to look at rare SM processes. In these processes new physics can enter at similar levels to the SM process.

1.2.1 Rare Decays at LHC*b*

This type of indirect search is not new. There is a long history of indirect measurements leading to evidence for new particles; the c quark through the GIM mechanism [5], the Z^0 in neutral current interactions and predictions of the top quark mass through electroweak decays and B_d oscillations to name a few.

In the era of the LHC, indirect measurements through CP violation or rare decays will continue to constrain the SM and could result in new discoveries. These measurements are also complementary to numerous direct searches at the Tevatron and LHC and ultimately can help to provide a more complete picture of any new theory as they provide access to the underlying phases of that theory.

This Thesis focuses on the rare electroweak decays $B^+ \to K^+\mu^+\mu^-$ and $B_d \to K^{*0}\mu^+\mu^-$ with branching fractions, from reference [6], of

$$
\begin{aligned}
\mathcal{B}\left(B^{+} \rightarrow K^{+}\mu^{+}\mu^{-}\right) &= 3.4^{+1.9}_{-1.4} \times 10^{-7} \\
\mathcal{B}\left(B_{d} \rightarrow K^{*0}\mu^{+}\mu^{-}\right) &= 1.22^{+0.38}_{-0.32} \times 10^{-6}
\end{aligned}
$$

These are discussed in greater detail in Chapters 2, 7 and 8.

Chapter 2

Weak decays in the Standard Model

A principal aim of the LHCb experiment is the discovery of new physics in B decays, looking for features of the dynamics that do not conform to the Standard Model (SM). This chapter summarises the SM description of weak decays and CP violation and introduces the framework and motivation for studying rare flavour changing neutral current (FCNC) decays in the SM.

The SM is the Quantum Field Theory that describes the forces and interactions at the atomic and sub-atomic level that we see in nature. These are the weak, strong and electromagnetic (EM) interactions. Conspicuous by its absence from this list is gravity which is not described in the Standard Model and theoretically challenging to include within any Quantum Field Theory. The SM is constrained to be invariant under a local gauge group $\mathrm{SU}(3)_\mathrm{C} \otimes \mathrm{SU}(2)_\mathrm{L} \otimes \mathrm{U}(1)_\mathrm{Y}$. The groups describing this symmetry are unitary and lead to a renormalisable theory. Here the indices C, L and Y stand for the *colour* of the strong interaction, the *left* handedness of the weak interaction and *hypercharge* of the electroweak theory respectively. The groups have 8 + 3 + 1 “generators” that give rise to the 8 gluons, the charged and neutral vector bosons of the weak interaction and the photon (γ). In addition to the $\mathrm{SU}(3)_\mathrm{C} \otimes \mathrm{SU}(2)_\mathrm{L} \otimes \mathrm{U}(1)_\mathrm{Y}$ group symmetry the SM is invariant under the the Lorentz and Poincaré groups. These are responsible for rotations, translations and boosts in space-time and invariance under these groups naturally leads the SM Lagrangian to conserve energy and momentum.

The SM Lagrangian[1] can be broken down as,

$$\mathcal{L}_{SM} = \mathcal{L}_{EW} + \mathcal{L}_{Higgs} + \mathcal{L}_{QCD} \quad .$$

The second of these terms, $\mathcal{L}_{Higgs}$, is introduced to allow particles to have mass without destroying the $\mathrm{SU(2)_L} \otimes \mathrm{U(1)_Y}$ gauge symmetry and is defined in Sec. 2.2. Throughout this chapter Greek indices are used to imply space-time indices and it is assumed that the indices are summed throughout.

2.1 The Weinberg-Salam model of Electroweak Interactions

In the 1930's Fermi postulated a four-fermion interaction to explain nuclear $\beta -$ decay with a coupling constant $G_F \sim 10^{-5}\,\mathrm{GeV}^2$. This proved an accurate first-order picture and was later extended by Weinberg and Salam into the full electroweak theory [10] [11].

To fully explain the phenomenology of weak interactions the theory required massive charged and neutral vector bosons and a V-A (vector-axial) structure that only couples to the left-handed helicity states. There are several consequences of this; significantly that there is no right-handed neutrino in the Standard Model as this does not feel either the weak, EM (as the neutrino carries no charge and can not couple to the photon) or strong force. Another consequence is that the weak interaction violates both C and P maximally (both of which are conserved by the electromagnetic and strong force). Finally, it is the large mass of the vector bosons ($M_W = 80.403 \pm 0.029\,\mathrm{GeV}$ and $M_Z = 91.1876 \pm 0.0021\,\mathrm{GeV}$ [6]) that is responsible for the short range of the weak force.

The left-handed fermions form a doublet $L = \frac{1}{2}\left(1-\gamma^5\right) f$, where f is the fermion field and the right-handed fermions a singlet $R = \frac{1}{2}\left(1+\gamma^5\right) f$. For the leptons,

$$\begin{aligned} L &= \begin{pmatrix} \nu_e \\ e \end{pmatrix}_L , \begin{pmatrix} \nu_\mu \\ \mu \end{pmatrix}_L , \begin{pmatrix} \nu_\tau \\ \tau \end{pmatrix}_L \\ R &= e_R \ , \ \mu_R \ , \ \tau_R \end{aligned}$$

---

[1] There are numerous text books covering the Standard Model in all its glory. Over the course of the PhD the author has, amongst others, used the books in references [7], [8] and [9].

and for the quarks,

$$L = \begin{pmatrix} u \\ d\,' \end{pmatrix}_L \ , \ \begin{pmatrix} c \\ s\,' \end{pmatrix}_L \ , \ \begin{pmatrix} t \\ b\,' \end{pmatrix}_L$$

$$R = u_R \ , \ d_R \ , \ c_R \ , \ s_R \ , \ t_R \ , \ b_R \quad .$$

The primes indicate that these are the weak and not the mass eigenstates and are defined in Sec. 2.4. These left-handed doublets and right-handed singlets transform under the group $SU(2)$ in different ways. The SM interaction has charged current $j^{\pm}_{\mu}$, and neutral current j^{EM}_{μ} and j^{Z}_{μ} interactions. These lead to terms in the Lagrangian,

$$\frac{g}{2\sqrt{2}} j^{\pm}_{\mu} W^{\pm\mu} - e j^{EM}_{\mu} A^{\mu} + \frac{g}{2\cos\theta_W} j^{Z}_{\mu} Z^{\mu}$$

where the A^{μ} is the photon field, e is EM and g the electroweak coupling constant and θ_W is the Weinberg angle.

The Weinberg-Salam model unifies QED, responsible for EM and the weak interaction, into a single gauge group $\mathrm{SU(2)_L \otimes U(1)_Y}$. This group has three weak isospin currents and a single hypercharge current with a pair of coupling constants g and g', where $g' = g\tan\theta_W$. There are four gauge bosons $W^{i=1\ldots3}_{\mu}$ and B_{μ} (the gauge boson associated with $U(1)_Y$) that lead to the observed vector bosons for the weak interaction and the photon. The fields for these bosons can be expressed in terms of $W^{i=1\ldots3}_{\mu}$ and B_{μ} as,

$$\begin{pmatrix} Z_{\mu} \\ A_{\mu} \end{pmatrix} = \begin{pmatrix} \cos\theta_W & \sin\theta_W \\ -\sin\theta_W & \cos\theta_W \end{pmatrix} \begin{pmatrix} W^3_{\mu} \\ B_{\mu} \end{pmatrix} \ , \ \begin{pmatrix} W^+_{\mu} \\ W^-_{\mu} \end{pmatrix} = \frac{1}{\sqrt{2}} \begin{pmatrix} 1 & i \\ 1 & -i \end{pmatrix} \begin{pmatrix} W^1_{\mu} \\ W^2_{\mu} \end{pmatrix}$$

and the EM coupling constant is related to g and g' through $e = g\sin\theta_W = g'\cos\theta_W$. The photon field is a linear combination of W^3_{μ} and B_{μ} and the EM charge of the fermion is given by the hypercharge Y and the third component of the weak isospin T^3 (corresponding to the Pauli matrix σ^3),

$$Q = T^3 + \frac{Y}{2} \quad .$$

The charge, hypercharge and T^3 associated with each of the fundamental fermions is provided for reference in Table 2.1.

	ν_L	e_L	e_R	u_L	d_L	u_R	d_R
Q	0	-1	-1	$+2/3$	$-1/3$	$+2/3$	$-1/3$
T^3	$+1/2$	$-1/2$	0	$+1/2$	$-1/2$	0	0
Y	-1	-1	-2	$+1/3$	$+1/3$	$+4/3$	$-2/3$

Table 2.1: Electroweak charge Q, Y and the third component of the weak isospin T^3 for quarks and leptons in the SM.

The Lagrangian for the electroweak theory is a combination of terms describing the behaviour of the free fermions, the behaviour of the bosons and the interaction between the bosons and the fermions.

$$\mathcal{L}_{EW} = \mathcal{L}_{Boson} + \mathcal{L}_{Fermion} + \mathcal{L}_{Interaction} \quad .$$

The first term represents the propagation of the free boson fields. It also introduces the self interaction of the bosons. In terms of the $W_\mu^{a=1...3}$ and B_μ,

$$\mathcal{L}_{Boson} = -\frac{1}{4}W^a_{\mu\nu}W^{a\mu\nu} - \frac{1}{4}B_{\mu\nu}B^{\mu\nu}$$

where the $W^a_{\mu\nu}$ and $B_{\mu\nu}$ are tensors with,

$$W^a_{\mu\nu} = \partial_\mu W^a_\nu - \partial_\nu W^a_\mu + g\epsilon^{abc}W^b_\mu W^c_\nu$$

$$B_{\mu\nu} = \partial_\mu B_\nu - \partial_\nu B_\mu \quad .$$

It is the last term in $W^a_{\mu\nu}$ that leads to the self-interaction of the electroweak theory with both tri-linear and quartic couplings between the gauge bosons. These couplings are shown in terms of the observed bosons in Fig. 2.1 . For this reason the electroweak theory is said to be non-Abelian as the force carriers themselves carry the charge of the theory. The same is true of the gluons of QCD as these carry colour charge but not of electromagnetism as the photon is neutral.

The coupling of fermions to the vector gauge bosons and the propagation of the free fermions is included in the SM through,

$$\begin{aligned}\mathcal{L}_{Fermion} + \mathcal{L}_{Interaction} \quad &= \quad i\bar{R}\gamma^\mu\left[\partial_\mu - i\tfrac{Y}{2}g'B_\mu\right]R + \\ & \quad\quad i\bar{L}\gamma^\mu\left[\partial_\mu - i\tfrac{Y}{2}g'B_\mu - \tfrac{i}{2}g\sigma_a W^a_\mu\right]L\end{aligned}$$

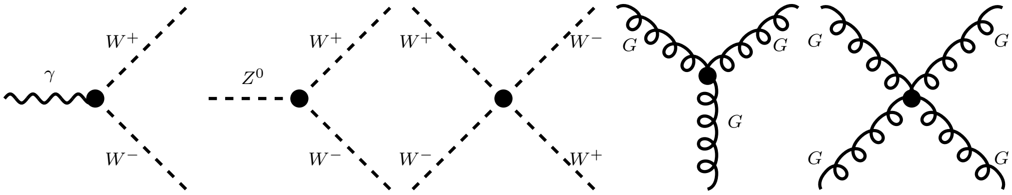

Figure 2.1: Trilinear and quartic couplings of the Electroweak theory and QCD. From left to right these are γW^+W^-, $Z^0W^+W^-$, $W^+W^-W^+W^-$ and the three and four gluon couplings.

where the σ_a are the Pauli Spin matrices and the γ^μ the Dirac matrices. The terms coupling the fermion fields to the bosons are prescribed by the invariance under the local gauge symmetry. This gauge invariance is a requirement that the theory is insensitive to phase changes. At tree level the couplings of the SM are shown in Fig. 2.2. The charged currents are flavour violating but there are no flavour-changing neutral currents at tree level in the SM.

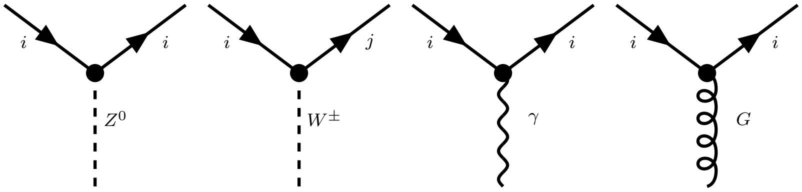

Figure 2.2: Coupling between the fermions and the bosons in the Standard Model. There are no flavour-changing neutral currents at tree level in the Standard Model.

For comparison the Lagrangian for electromagnetism can be written,

$$\mathcal{L} = i\bar{f}\gamma^\mu \left[\partial_\mu - ieA_\mu\right] f - \frac{1}{4}F^{\mu\nu}F_{\mu\nu} \quad .$$

where

$$F_{\mu\nu} = \partial_\mu A_\nu - \partial_\nu A_\mu \quad .$$

2.2 Spontaneous Symmetry Breaking

In the previous section the fields have, necessarily, been massless. Introducing mass terms for the fields by hand breaks the gauge symmetries. Instead an additional scalar field, ϕ is introduced along with a potential $V(\phi)$. If the potential takes the form,

$$V(\phi) = \mu^2 \phi^\dagger \phi + \lambda \left(\phi^\dagger \phi\right)^2$$

and $\mu^2 < 0$ then the theory remains invariant under the SU(2) ⊗ U(1) group symmetry but there is a ground state that breaks the symmetry. This can be used to introduce effective mass terms for the gauge bosons. This is known as the Higgs mechanism, details of which can be found in references [12] and [13]. The field, ϕ, has to be a scalar field as a fermion or vector field, with a vacuum expectation value, would break gauge invariance.

If the field ϕ is a doublet with a non-zero vacuum expectation value $\langle\phi\rangle$

$$\phi = \begin{pmatrix} \phi^+ \\ \phi^0 \end{pmatrix}, \ \langle\phi\rangle = \begin{pmatrix} 0 \\ v/\sqrt{2} \end{pmatrix}, \ v = \left(\frac{-\mu^2}{\lambda}\right)^{1/2}$$

and a term is introduced into the Lagrangian,

$$\mathcal{L}_{Higgs} = \left|\left(\partial_\mu - \frac{1}{2} i g \sigma_a W_\mu^a - \frac{i}{2} g' B_\mu\right)\phi\right|^2 + V(\phi)$$

then three of the gauge bosons acquire a mass (the W^+, W^- and the Z^0). The photon remains massless. There is also a coupling to a real, massive, scalar field, the Higgs (H^0). The mass of the W and Z are given by

$$m_W = \frac{gv}{2} \quad \text{and} \quad m_Z = \frac{m_W}{\cos\theta_W}$$

The mass terms for the fermions are introduced by Yukawa-type couplings (with coupling constants Γ^{ij}) to the scalar field. Expanding the scalar field ϕ about the vacuum expectation value in terms of the Higgs field,

$$\phi = \frac{1}{\sqrt{2}} \begin{pmatrix} 0 \\ v + H^0 \end{pmatrix} \quad .$$

For example for the down-type quarks ($i, j = d, s, b$),

$$-\Gamma^{ij} \bar{L}^i \phi R^j = -M^{ij} \bar{d}_L^i d_R^j \left(1 + \frac{H^0}{v}\right) \quad .$$

M^{ij} is a mass matrix. This has introduced a mass term and a coupling between the fermions and the Higgs proportional to the mass of the fermion. If the neutrino is treated as being massless, there are three Γ and three mass matrices; one for the up-type quarks, one for the down-type and one for the electron (μ and τ). Each mass matrix can then be diagonalised using a unitary matrix U, ${d'}^i_L = U^{ij}_L d^j_L$.

2.3 The Strong Interaction

The final term in the Standard Model Lagrangian comes from the strong force, described by Quantum Chromo Dynamics (QCD). QCD obeys the $\mathrm{SU}(3)_{\mathrm{C}}$ group symmetries, with

$$\mathcal{L}_{QCD} = -\tfrac{1}{4} G^a_{\mu\nu} G^{a\mu\nu} + \bar{q} i \gamma_\mu \left[\partial^\mu - i g \gamma_\mu T^a G^{a\mu} \right] q$$

$$G^a_{\mu\nu} = \partial_\mu G^a_\nu - \partial_\nu G^a_\mu - g f^{abc} G^b_\mu G^c_\nu$$

The T^a are 3×3 matrices in the fundamental representations of the group and f^{abc} are the group structure constants. SU(3) remains unbroken and the eight gluons ($G^{a=1\ldots8}$) remain massless. Unlike the EM coupling constant, the coupling constant of QCD becomes large at long-distances (small energies). The quarks and gluons are said to be confined and no free particle carries the colour charge.

2.4 CP violation and the Unitarity Triangle

In the previous sections the $d\,'$, $s\,'$ and $b\,'$, in the left-handed doublets, have been the eigenstates of the electroweak theory. These are related to the observed mass eigenstates through the Yukawa couplings. In charged current interactions mediated by the $W^\pm$ there are terms proportional to

$$\bar{L} \gamma^\mu \sigma_a W^a_\mu L$$

in the Lagrangian. These can now be written in terms of the mass eigenstates,

$$\bar{u}^i_L \left((U^u_L)^\dagger U^d_L \right) \gamma^\mu \sigma_a W^a_\mu d^j_L$$

with

$$(U_L^u)^\dagger U_L^d = V_{CKM}$$

and

$$\begin{pmatrix} d\,' \\ s\,' \\ b\,' \end{pmatrix} = V_{CKM} \begin{pmatrix} d \\ s \\ b \end{pmatrix} = \begin{pmatrix} V_{ud} & V_{us} & V_{ub} \\ V_{cd} & V_{cs} & V_{cb} \\ V_{td} & V_{ts} & V_{tb} \end{pmatrix} \begin{pmatrix} d \\ s \\ b \end{pmatrix} \quad .$$

The matrix V_{CKM} is a complex, unitary matrix named after Cabibbo, Kobayashi, and Maskawa the original proponents of the theory [14]. If there were only two generations of quarks in the Standard Model then this matrix would be a real rotation matrix (V) with a single rotation angle θ_C,

$$V = \begin{pmatrix} \cos\theta_C & \sin\theta_C \\ -\sin\theta_C & \cos\theta_C \end{pmatrix}$$

The presence of a third generation of quarks leaves the matrix with four free parameters; three angles and a single complex phase. This complex phase gives rise to an imaginary part of the V_{CKM} and in turn violates the invariance of the product of the C and P symmetries in the SM.

In the SM the equivalent matrix for the leptons is assumed to be a unit matrix. Evidence of neutrino oscillations indicates that the neutrinos have some small mass and so one can include an equivalent matrix for the leptons (the PMNS matrix [15]).

The CKM matrix, V_{CKM}, can be written as the product of three rotation matrices ($c_i = \cos\theta_i, s = \sin\theta_i$) with a phase ($\delta$).

$$V_{CKM} = \begin{pmatrix} 1 & 0 & 0 \\ 0 & c_2 & s_2 \\ 0 & -s_2 & c_2 \end{pmatrix} \times \begin{pmatrix} c_1 & s_1 & 0 \\ -s_1 & c_1 & 0 \\ 0 & 0 & 1 \end{pmatrix} \times \begin{pmatrix} 1 & 0 & 0 \\ 0 & 1 & 0 \\ 0 & 0 & e^{-i\delta} \end{pmatrix} \times \begin{pmatrix} 1 & 0 & 0 \\ 0 & c_3 & s_3 \\ 0 & -s_3 & c_3 \end{pmatrix}$$

and reduced to

$$V_{CKM} = \begin{pmatrix} c_{12}c_{13} & s_{12}c_{13}s_{13}e^{-i\delta} & s_{13}e^{-i\delta} \\ -s_{12}c_{23} - c_{12}s_{23}s_{13}e^{i\delta} & c_{12}c_{23} - s_{12}s_{23}e^{i\delta} & s_{23}c_{13} \\ s_{12}s_{23} - c_{12}c_{23}s_{13}e^{i\delta} & -s_{23}c_{12} - s_{12}c_{23}s_{13}e^{i\delta} & c_{23}c_{13} \end{pmatrix} \quad .$$

More commonly the CKM matrix is parametrised by the Wolfenstein parametrisation [16] as

$$V_{CKM} = \begin{pmatrix} 1-\frac{1}{2}\lambda^2 & \lambda & A\lambda^3\left(\rho - i\eta\right) \\ -\lambda & 1-\frac{1}{2}\lambda^2 & A\lambda^2 \\ A\lambda^3\left(1-\rho-i\eta\right) & -A\lambda^2 & 1 \end{pmatrix} + \mathcal{O}\left(\lambda^4\right)$$

where A, ρ and η are real parameters of $\mathcal{O}(1)$ and $\lambda = \sin\theta_C \simeq 0.22$. The unitarity of the CKM matrix $V^{\dagger}_{CKM}V_{CKM} = 1$, results in 3 normalisation and 6 orthogonality conditions. The orthogonality of the columns and rows map out triangles in the complex (ρ, η) plane. The most usefull of these for B decays is shown in Fig. 2.3. Here, $\bar{\rho}$ and $\bar{\eta}$ represent ρ and η scaled by $\left(1-\frac{1}{2}\lambda^2\right)$. This triangle corresponds to:

$$V_{ud}V^*_{ub} + V_{cd}V^*_{cb} + V_{td}V^*_{tb} = 0$$

with angles α, β and γ given by:

$$\alpha = -Arg\left(\frac{V_{td}V^*_{tb}}{V_{ud}V^*_{ub}}\right) \quad \beta = -Arg\left(\frac{V_{cd}V^*_{cb}}{V_{td}V^*_{tb}}\right) \quad \gamma = -Arg\left(\frac{V_{ud}V^*_{ub}}{V_{cd}V^*_{cb}}\right)$$

The current status of measurements of the elements of the CKM matrix, taken from the HFAG (the heavy flavour averaging group [17]) is:

- $|V_{ud}|$: Measured from β-decay to be

  $$|V_{ud}| = 0.9740 \pm 0.0001 \pm 0.0008_{theory}$$

- $|V_{us}|$: Extracted from the Kaon decays $K^0_L \rightarrow \pi^+ l^+ \nu_l$ and $K^+ \rightarrow \pi^0 l^+ \nu_l$

  $$|V_{us}| = 0.2228 \pm 0.0039 \pm 0.0018$$

- $|V_{cd}|$ and $|V_{cs}|$: Measured from charm production in electron deep inelastic scattering.

- $|V_{cb}|$: Measured from the branching fractions of inclusive or exclusive semi-leptonic $b \rightarrow cl\nu$ decays.

$$|V_{cb}|_{Exclusive} = (42 \pm 0.6_{stat} \pm 0.8_{theory}) \times 10^{-3}$$

$$|V_{cb}|_{Inclusive} = \left(40.2^{+2.1}_{-1.8}\right) \times 10^{-3}$$

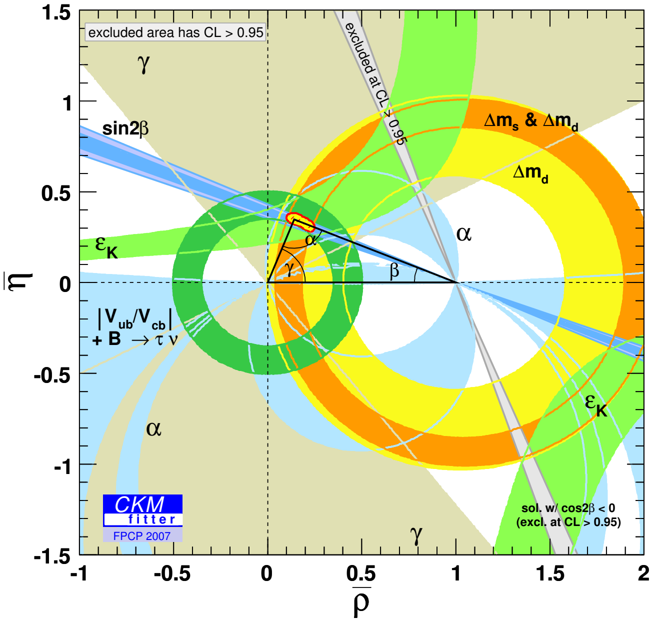

Figure 2.3: The present status of the measurements of the Unitarity triangle. From reference [18].

- $|V_{ub}|$: Measured from branching ratios of inclusive and exclusive semi-leptonic $b \longrightarrow ul\nu$ decays.

$$|V_{ub}|_{Exclusive} = \left(3.64 \pm 0.17_{stat} \underbrace{{}^{+0.16}_{-0.17}\ {}^{+0.53}_{-0.39}}_{theory}\right) \times 10^{-3}$$

$$|V_{ub}|_{Inclusive} = (4.45 \pm 0.19_{stat} \pm 0.68_{theory}) \times 10^{-3}$$

- Δm_d: The $B^0\overline{B}^0$ oscillation frequency depends on the mass difference Δm_d between the two B mass eigenstates. The oscillation comes from a FCNC box transition, see Fig. 2.4.

$$\Delta m_d = 0.502 \pm 0.006\,\mathrm{ps}^{-1}$$

- Δm_s: The mass difference between the B_s mass eigenstates. This has recently been measured by the CDF experiment [19] to be

$$\Delta m_s = 17.77 \pm 0.10 \pm 0.07\,\mathrm{ps}^{-1}$$

- ε_K: The CP violation parameter governing the K sector. This has been measured from the ratio of branching fractions for the decays $K^0_L \longrightarrow \pi\pi$ and $K^0_S \longrightarrow \pi\pi$.

$$\varepsilon_K = 2.280 \pm 0.013 \times 10^{-3}$$

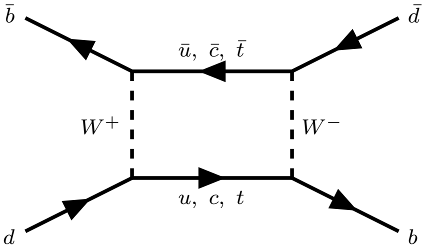

Figure 2.4: One of the two Standard Model diagrams which generate B_d oscillations. For B_s oscillation the d-quark is replaced by an s-quark.

- β: $\sin 2\beta$ can is measured from decays of $b \to c\bar{c}s$, in particular $B^0 \to J/\psi K^0_S$. The world average from *BABAR* [20] and Belle [21] is given in reference [17]:

$$\sin 2\beta = 0.739 \pm 0.048$$

- α: Extracted from measurements of time dependent CP asymmetries in $B^0 \to \pi^+\pi^-$, $B^0 \to \rho\rho$ and from an analysis of the Dalitz plot for $B^0 \to \rho^+\pi^-$ at *BABAR* ([22], [23]) and Belle ([24], [25]). The combined results is $\alpha = 93 \pm 4^\circ$.
- γ: Extracted from b decays to charm, e.g. $B \to D^{(*)}K$ at *BABAR* ([26], [27]) and Belle ([28]). The average, with a two-fold ambiguity is $\gamma = 88 \pm 16^\circ$ or $\gamma = -92 \pm 16^\circ$.

These measurements over constrain the unitarity triangle and are consistent - thus confirming the SM description of CP violation. Measurements at LHCb will hope to further constrain the triangle by comparing measurements from tree and higher order loop processes.

2.5 Operator Product Expansion

Flavour physics is governed by the interplay between the strong and weak interactions. As an example, the weak decay $b \to c\mu\overline{\nu}_\mu$ is dominated by a tree level Feynman diagram but the decay dynamics includes strong interactions and the situation is closer to the one in Fig. 2.5.

The remainder of this chapter focuses on new physics searches in rare FCNC $b \to s\ell^+\ell^-$ decays of B hadrons. They are mediated by box or penguin diagrams in the SM, an example of which is given in Fig. 2.7(a). The language used to describe

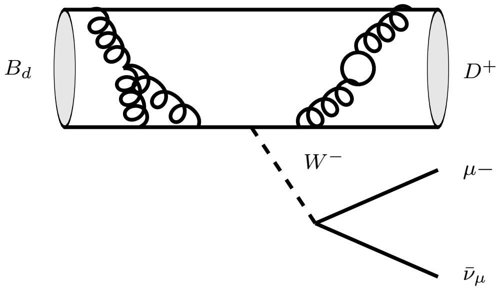

Figure 2.5: An example of the interplay of strong and weak physics in the semi-leptonic decay $B \to D\mu\nu$.

these decays is motivated by the operator product expansion (OPE). In the SM, the Hamiltonian describing these $b \to s\ell^+\ell^-$ decays can be written as

$$\mathcal{H} = -\frac{4G_F}{\sqrt{2}} V_{tb} V_{ts}^* \sum_{i=1}^{10} [\mathcal{C}_i(\mu)\mathcal{O}_i(\mu) + \mathcal{C}_i'(\mu)\mathcal{O}_i'(\mu)] \quad .$$

$\mathcal{H}$ is an effective Hamiltonian valid at an energy scale μ. For B-physics the energy scale, μ is $\mathcal{O}(m_b)$. It is expanded as a series of vertices represented by the local operators $\mathcal{O}_{i=1-10}$ and coupling constants given by the Wilson coefficients $\mathcal{C}_i$. The primed operators represent right-handed currents that are highly suppressed (by m_B/m_W) in the SM. The aim of this expansion is to separate the calculation into long and short range parts.

The short range parts are the heavy degrees of freedom, with large masses, in the penguin or box diagrams (the top quark, $W^\pm$ and the Z^0 in the Standard Model). These are integrated out and included in the coupling constants (the Wilson coefficients $\mathcal{C}_i(\mu)$) to leave a low energy effective theory with just five quarks. The Wilson coefficients can be calculated using perturbation theory due to the asymptotic freedom of QCD, that the coupling becomes small as the energy increases.

The long distance effects coming from the strong interaction contribute to the operator matrix elements. These can not be calculated perturbatively and are calculated using sum rules and Heavy Quark Effective Theory (which assumes the mass of the b quark $m_b \simeq m_B$).

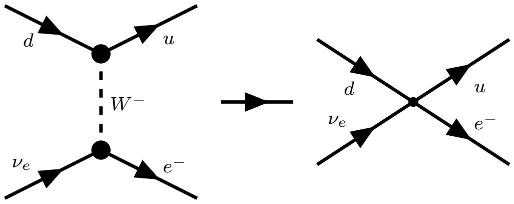

Figure 2.6: β-decay in the full and effective theory.

A good overview of the operator product expansion and its use in weak CP violating or rare decays can be found in reference [29]. The principles behind the OPE are neatly illustrated for β-decay in Fig. 2.6. In this case the effective Hamiltonian takes the familiar low energy form of the original Fermi theory:

$$\mathcal{H}^{eff} = \frac{G_F}{\sqrt{2}} \cos\theta_C \left(\bar{u}\gamma^\mu \left(1-\gamma^5\right) d\right) \left(\bar{e}\gamma_\mu \left(1-\gamma^5\right) \nu_e\right)$$

and the full dynamical (electroweak + QCD) theory is reduced to a four fermion operator with an effective coupling constant at the vertex.

2.6 Rare Decays as a Probe for New Physics

There are no FCNC processes at tree level in the SM as these can neither come from the photon, the Z^0 or the Higgs (the Yukawa couplings are flavour diagonal). This makes these processes an ideal place to search for new physics. Rare FCNC B decays such as the $b \to s\ell^+\ell^-$ decays described in this thesis can have sizeable new physics contributions that are not swamped by the competing SM process. The SM particles, for example the particles in the $t-W$ loop of Fig. 2.7(a), can be replaced by any new physics particle or particles running in the loop. One example is provided in Fig. 2.7(b) where the $t-W$ loop in the SM decay is replaced by a loop containing down-type supersymmetric particles and a neutralino from a supersymmetric theory [30].

Measurements of these FCNC are model independent and are sensitive to a wide variety of new physics scenarios be it supersymmetry, graviton exchange, additional Higgs doublets or extra dimensions, with mass scales up to $\mathcal{O}(10\,\mathrm{TeV})$. They also have the added benefit that they are sensitive to the chiral structure of the new physics model. New particles can modify the dynamics of the decay; changing the branching ratio, the amount of CP violation or the kinematic distribution of particles coming from the decay.

Practically, the new heavy degrees of freedom introduced into the loop by the new physics model will either modify the Wilson coefficients from their SM value, increase the contribution from right-handed operators or introduce a new set of four-fermion operators into the Hamiltonian. For the decay $B^+ \to K^+\mu^+\mu^-$, many supersymmetric models will increase the contribution from the scalar or pseudo-scalar operators. This increase comes from Higgs penguins in the supersymmetric model.

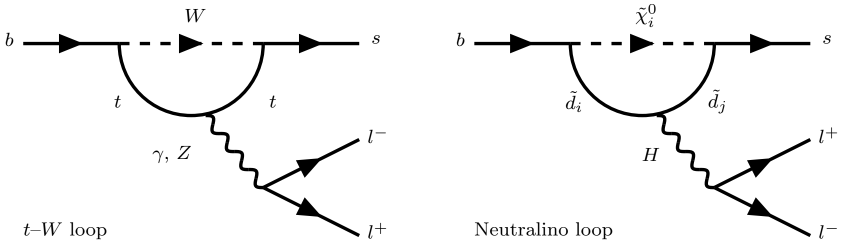

(a) (b)

Figure 2.7: Flavour changing neutral current transitions $b \to sl^+l^-$ in the Standard Model (electroweak penguins) and a competing diagram in a Supersymmetric theory (neutralino loop).

The dominant Standard Model contributions come from the four point operators,

$$\begin{aligned}
\mathcal{O}_7 &= \frac{e}{16\pi^2} m_b \left(\bar{s}\sigma_{\mu\nu}\tfrac{1}{2}\left(1+\gamma_5\right) b\right) F^{\mu\nu} \quad , \\
\mathcal{O}_9 &= \frac{e^2}{16\pi^2} \left(\bar{s}\gamma_\mu\tfrac{1}{2}\left(1-\gamma_5\right) b\right) \left(\bar{l}\gamma^\mu l\right) \quad , \\
\mathcal{O}_{10} &= \frac{e^2}{16\pi^2} \left(\bar{s}\gamma_\mu\tfrac{1}{2}\left(1-\gamma_5\right) b\right) \left(\bar{l}\gamma^\mu\gamma_5 l\right) \quad , \\
\mathcal{O}_7' &= \frac{e}{16\pi^2} m_b \left(\bar{s}\sigma_{\mu\nu}\tfrac{1}{2}\left(1-\gamma_5\right) b\right) F^{\mu\nu} \quad ,
\end{aligned}$$

where $\sigma_{\mu\nu} = \frac{i}{2}\left[\gamma_\mu, \gamma_\nu\right]$.

2.6.1 Constraints on New Physics

Currently some of the strongest constraints on new physics come from this type of indirect measurement; the measured branching fractions of $B_d \to K^{*0}\gamma$ [6], $B_d \to$

$K\mu^+\mu^-$ and $B_d \to K^{*0}\mu^+\mu^-$ at the B-Factories (and CLEO) and the measured value of Δm_s from the TeVatron. The branching ratio of $B_d \to K^{*0}\gamma$ and Δm_s in particular have been powerful in ruling out regions of parameter space in the new physics models.

$$\begin{aligned} \mathcal{B}\left(B_d \to K^{*0}\gamma\right) &= 4.01 \pm 0.2 \times 10^{-5} \\ \mathcal{B}\left(B_d \to K\mu^+\mu^-\right) &= 3.4^{+1.9}_{-1.4} \times 10^{-7} \\ \mathcal{B}\left(B_d \to K^{*0}\mu^+\mu^-\right) &= 1.22^{+0.38}_{-0.32} \times 10^{-6} \end{aligned}$$

The branching fraction for $B_d \to K^{*0}\gamma$ is linked to the Wilson coefficient $\mathcal{C}_7$ through,

$$\Gamma\left(b \to s\gamma\right) = \frac{G_F^2 m_b^5 \alpha}{32\pi^4} |V_{ts}^* V_{tb}|^2 \left(|\mathcal{C}_7|^2 + |\mathcal{C}'_7|^2\right) \quad .$$

There is no discernable difference between these measured values and the SM prediction.

2.6.2 Observables

At LHCb, due to the hadronic environment and the large background that this entails, it will be difficult to make fully inclusive measurements of the $b \to s\ell^+\ell^-$ transition. In particular it will be very challenging to reconstruct both neutral kaons and pions. Instead measurements will focus on the exclusive modes $B \to (K, K^{*0})\mu^+\mu^-$.

The existing branching fraction measurements from *BABAR* and Belle show no contribution from new physics. There is however a large uncertainty of $\mathcal{O}(30\%)$ on the theory predictions of these decays (coming from the form factors). These uncertainties can be cancelled by forming appropriate ratios to give theoretically clean observables. The most widely discussed of these is the forward-backward asymmetry

$$A_{FB}(q^2) = \frac{\int_0^1 d\cos\theta_L \frac{d^2\Gamma}{dq^2\ d\cos\theta_L} - \int_{-1}^0 d\cos\theta_L \frac{d^2\Gamma}{dq^2\ d\cos\theta_L}}{\int_{-1}^1 d\cos\theta_L \frac{d^2\Gamma}{dq^2\ d\cos\theta_L}}$$

This will be discussed in much more detail in Sec. 7. It is the asymmetry between the number of decays with the μ^+ in the forward and the backward direction with respect to the direction of the B (in the dimuon rest frame). The size of the asymmetry changes with the invariant mass squared (q^2) of the dimuon pair and strongly depends on the operators and couplings that are present in the effective theory. The A_{FB} as a function of q^2 in the Standard Model and several new physics scenarios, taken from reference [31], is given in Fig. 2.8.

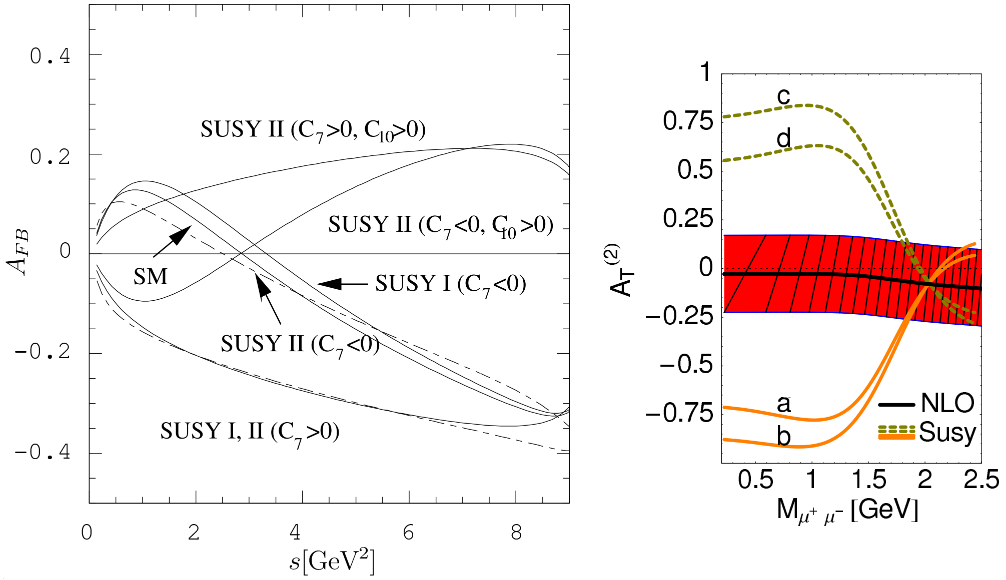

(a) (b)

Figure 2.8: Forward-backward asymmetry, the angle between the positive muon and the B in the decay $B_d \to K^{*0}\mu^+\mu^-$, versus $s = q^2 = m^2_{\mu\mu}$ in the Standard model and several New Physics scenarios (a) from [31] and the asymmetry of the transversity amplitudes $A_T^{(2)}$ (b) from [32].

Listed here, but not included in this thesis, are alternative observables that also have the potential to uncover new physics in the $b \to s\ell^+\ell^-$ decays:

- The asymmetry of the transversity amplitudes, $A_T^{(2)}$ [32].
- R_K and R_{K*}. The ratio of $B \to K^{(*)}\mu^+\mu^-$ to $B \to K^{(*)}e^-e^+$ [33] [34].
- CP asymmetries.
- Isospin asymmetries [35].

2.7 Summary

This chapter was intended as an introduction to the standard model theory and motivation for studying these rare processes. The rare decay $B_d \to K^{*0}\mu^+\mu^-$ looks particularly promising for new physics searches at LHCb. It is a FCNC $b \to s\ell^+\ell^-$ transition that can include sizeable contributions from new physics particles. It can also be cleanly reconstructed in the detector. The following chapters describe aspects of the detector hardware but Chapters 7 and 8 return to these $b \to s\ell^+\ell^-$ decays and emphasise LHCb's potential for making a measurement of the A_{FB} in $B_d \to K^{*0}\mu^+\mu^-$. The new physics scenarios in Fig. 2.8 are not ruled out by the indirect constraints that were discussed earlier (although having $A_{FB} < 0$ across the q^2 range has been ruled out to three standard deviations by measurements at *BABAR* and Belle). There are sizeable differences between the different scenarios, not just in the A_{FB} but also in the q^2 dependence, that LHCb will be sensitive to.

Chapter 3

The LHC*b* Experiment

The LHC*b* detector is a forward spectrometer covering polar angles, with respect to the LHC beam line, from 10 to 300 (250) mrad in the bending (non-bending) plane of the magnet. The required momentum coverage extends from 1-200 GeV/c and particle identification (ID) is optimised for the range 2-100 GeV/c.

The detector (as illustrated in Fig. 3.1 and described in the LHC*b* technical proposal [36]) has a silicon vertex detector around the interaction point, followed by a gas volume of a Cherenkov detector that aids particle ID. A second Cherenkov detector sits futher downstream. The tracking system of LHC*b* is compromised of the vertex detector, four layers of silicon strip detectors (labelled TT in Fig. 3.1) that sit upstream of a dipole magnet and three further tracking stations (labelled T1-T3) downstream of the magnet. These tracking stations have silicon strip detectors closest to the beam line where the rate is highest and straw tubes further out. Further downstream are electromagnetic and hadronic calorimeters that measure the energy of and provide particle ID for photons, electrons and hadrons. Finally, there is a muon filter, an instrumented series of iron walls that is used to identify the passage of muons in the detector.

3.1 The LHC Machine and Collision Kinematics

The Large Hadron Collider (LHC) is a 7 TeV on 7 TeV proton-proton collider located approximately 100 m under the French-Swiss border in the old LEP [37] tunnel. A detailed technical description of the LHC can be found in the LHC conceptual design

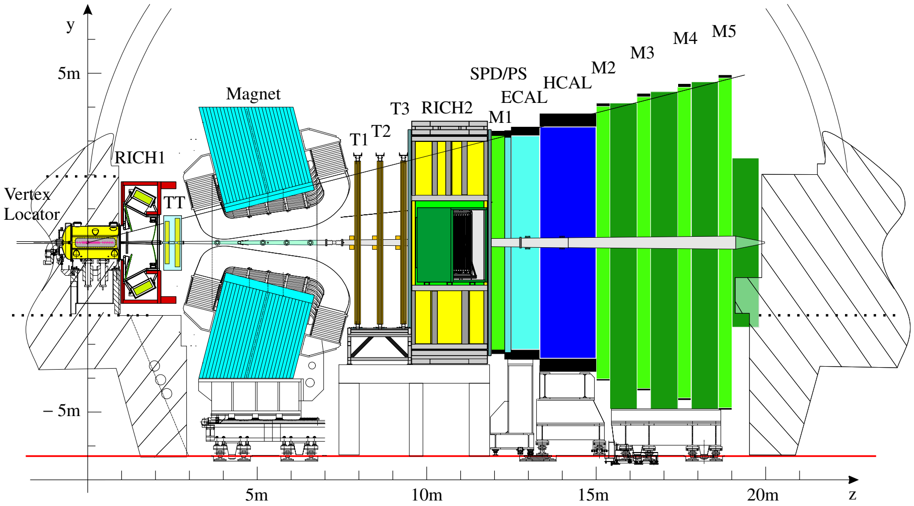

Figure 3.1: The LHCb detector. The Vertex Locator (VELO) sits closest to the interaction region and is followed downstream by the two gas volumes of the RICH detector the 4 tracking stations (the TT and T1-T3), the Scintillating Pad Detector (SPD), Pre-Shower (PS), the Electromagnetic and Hadronic Calorimeters and the 5 muon stations (M1-M5).

report [38]. The $\sqrt{s} = 14\,\text{TeV}$ centre of mass energy is achieved by accelerating the protons in stages. They are produced by ionisation of hydrogen atoms and then accelerated by a linear accelerator up to 50 MeV. The protons are then injected into a series of synchrotron accelerators; the PS-Booster which accelerates the protons up to 1.4 GeV, the PS which accelerates them to 25 GeV and finally the SPS. The SPS accelerates the protons up to 450 GeV where they are injected into the LHC main ring. An overview of the accelerator complex is shown in Fig. 3.2.

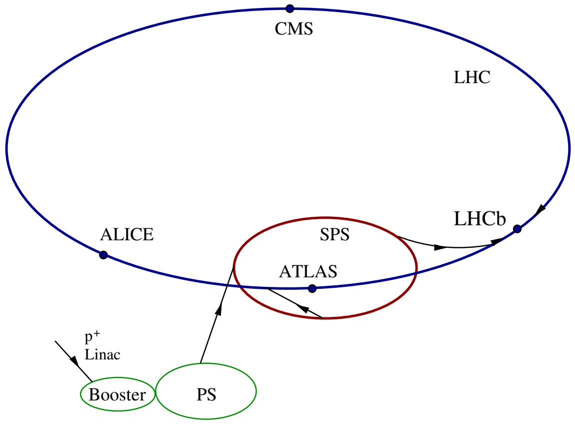

Figure 3.2: Overview of the CERN accelerator facilities used by the LHC showing the different accelerator complexes and the position of LHCb and the other principal experiments.

The LHC main ring is constructed from a series of radio-frequency (RF) cavities, 8.3 T dipole steering magnets, quadrupole focusing and defocusing magnets and sextupole and decapole corrector magnets. The RF cavities are responsible for accelerating the beam and provide an energy gain of $\simeq 0.5\,\mathrm{MeV}$ per turn. Unlike the other accelerators on the CERN complex, which use warm (room temperature) iron magnets, the magnets in the LHC main ring are super-conducting and operate at liquid Helium temperatures. A photograph of one of the first dipole magnets being installed at CERN is included in Fig. 3.3.

Figure 3.3: Photograph of one of the first LHC dipole magnets being installed in the LHC ring. From [39].

For rare decay measurements at the LHC*b* it is important to maximise the number of signal events whilst minimising any backgrounds. Reducing the background rate can be very challenging and consequently the luminosity at the LHC*b* interaction point is reduced from the design value $L = 10^{34}\,\mathrm{cm^{-2}s^{-1}}$ to about $2 \times 10^{32}\,\mathrm{cm^{-2}s^{-1}}$. This reduces the number of events containing pile-up where there are multiple inelastic collisions in a single bunch crossing. Fig. 3.4 demonstrates the typical rate of bunch crossings with zero, one, two, three and four inelastic collisions versus the beam luminosity. The luminosity is given by,

$$L = \frac{N_{Bunches.} \times N_{Protons} \times f}{4\pi \times (\beta^{*}\epsilon)_x^{1/2} (\beta^{*}\epsilon)_y^{1/2}}$$

where f is the revolution frequency (11.25 kHz) and ϵ the beams' phase space volume which is fixed at injection. The number of protons in each bunch $N_{Protons}$ is 1.15×10^{11} and results in a very large amount of energy (362 MJ) being stored in the circulating beams. The luminosity of the beam is tuned at the interaction regions

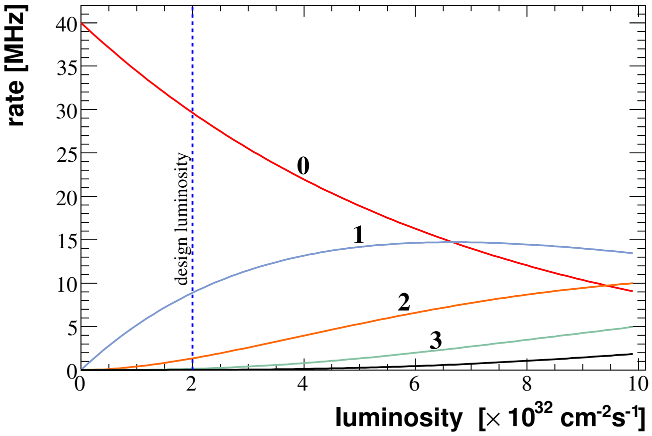

Figure 3.4: Rate of crossings with zero, one, two, three and four inelastic collisions versus the instantaneous luminosity, with $\sigma_{inelastic} = 60\,\text{mb}$.

by varying β^* which is determined by the focusing power of the quadrapole close to the interaction point.

The event yield (N per second) for a particular type of event is determined by the luminosity at the interaction point and the cross-section σ for the physics process involved ($N = L \times \sigma$).

LHC*b*'s primary focus is physics measurements in decays of *b*-Hadrons (B_d, B^+, B_s, B_c^+ and Λ_b and their antiparticles). The cross-section for *b*-quark production, $\sigma_{b\bar{b}}$, is expected to be $500\,\mu$b and leads to an annual yield of 10^{12} $b\bar{b}$ pairs. This cross section should be compared to the total cross-section for visible, inelastic, collisions which is expected to be 60 mb. The term visible is used to refer to inelastic collisions with at least two tracks in the vertex detector. The total cross-section, including elastic scattering is predicted to be 100 mb.

3.1.1 Heavy Flavour Production at the LHC

The geometry of the LHC*b* detector is determined by the physics of the *b* production at the LHC. The dominant production processes are illustrated in Fig. 3.5; these are [40]:

- Pair production. This is the leading order process and at the LHC is predominantly $gg \rightarrow b\bar{b}$. This differs from the production at the TeVatron where the presence of the $\bar{q}$ in the anti-proton increases the rate of $q\bar{q} \rightarrow b\bar{b}$ production.

- Heavy flavour excitation. A virtual heavy flavour quark that is off mass shell in one of the incoming particles is scattered by a parton from the other particle putting it on mass shell.

- Gluon splitting. The $b\bar{b}$ pair is not created in the hard scatter and is instead radiated by a gluon in the final state interactions.

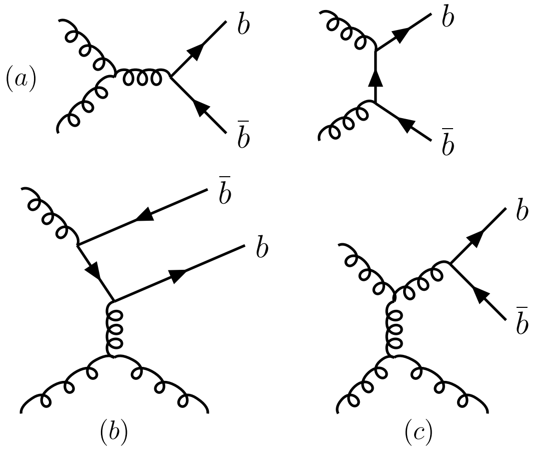

Figure 3.5: Feynman diagrams for the dominant production modes for $b\bar{b}$ pairs at the LHC. These are pair production *(a)*, heavy flavour excitation *(b)* and gluon splitting *(c)*.

The high LHC energy favours collisions with one hard and one soft parton which produce both the b- and $\bar{b}$ hadrons in the same forward or backward cone with a large boost. This is demonstrated in Fig. 3.6 and motivates the forward geometry of the LHCb detector. By offsetting the interaction region by 11.25 m (3× the inter-bunch spacing) in the cavern[1] the spectrometer is able to cover 20.088 m and provide a longer arm for tracking, which in turn provides a better momentum resolution.

3.1.2 Interface to the Machine

The interface between LHCb and the LHC accelerator is a combination of beryllium and stainless steel beam pipe sections. These are conical sections with opening half-angles of 25 mrad extending from the interaction region to the first tracking station, and 10 mrad further downstream. Beryllium is used closest to the interaction region, around the tracking stations and near the RICH detectors where it is critical to reduce the number of particles from secondary interactions in the beam pipe. In the

---

[1] LHCb sits at interaction point 8 on the LHC ring in the cavern previously occupied by the DELPHI experiment at LEP.

calorimeters and the muon stations where the rate from secondaries can be higher steel sections are favoured over (toxic, fragile and expensive) beryllium pieces. The beam pipe must be able to maintain ultra-high vacuums of $10^{-9} - 10^{-8}$ mbar.

3.2 Tracking in LHC*b*

Tracking of long-lived charge particles in LHC*b* is carried out by the combination of a vertex detector (the VELO) that sits close to the beam line around the proton-proton interaction region, a large dipole magnet with a field of 1.1T (and a bending power of 4 Tm) and tracking stations that sit downstream of the interaction point. These include the sub-detectors labelled as TT (the trigger tracker) and the tracking stations T1 through T3 in Fig. 3.1.

The track deviation in the magnetic field of the dipole magnet is used to determine the momentum of the reconstructed particles. A full track fit is carried out using a Kalman filter [41] with a description of the material in the detector to provide an optimum measurement of the track parameters. The momentum resolution of the LHC*b* detector is dominated by multiple coulomb scattering and is expected to be $\delta p/p = 0.38\%$. This corresponds to a precision of about 15-20 MeV in the reconstructed mass of a typical B decay. This is 18 MeV for reconstructed $B_d \to K^{*0}\mu^+\mu^-$ decays (with four charged tracks) discussed in chapters 7 and 8.

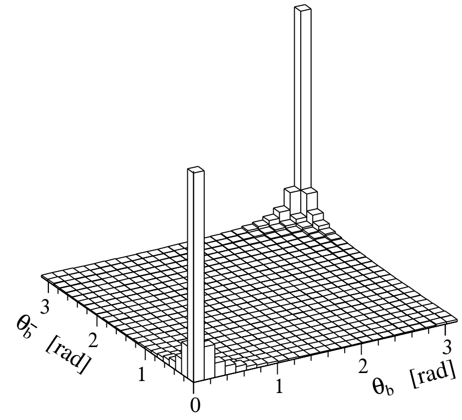

Figure 3.6: Simulated distribution (from PYTHIA) of the polar angle of b-hadrons from p-p collisions at the LHC. At 14 TeV both the b- and $\overline{b}$ are created in the same forward (or backward) cone.

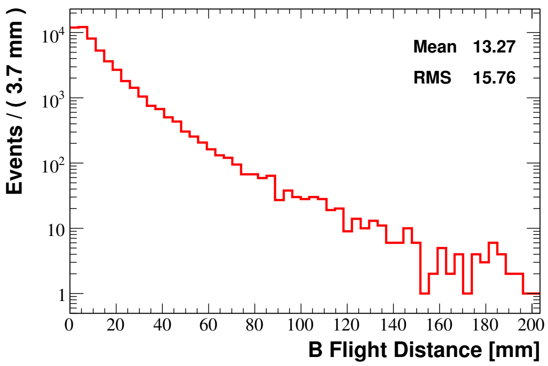

Figure 3.7: The reconstructed B_d flight distance in $B_d \to K^{*0}\mu^+\mu^-$ decays.

3.2.1 Vertex Locator (VELO)

The vertex locator (VELO) [42] sits closest to the interaction region and provides the location of secondary vertices coming from short lived particles in an event and track Impact Parameters (IP). B hadrons have a non-negligible lifetime $c\tau = 458.7\,\mu$m and due to the large boost are expected to fly distances of several mm in the detector before decaying. The flight distance, from the interaction point, of reconstructed $B_d \to K^{*0}\mu^+\mu^-$ decays in the LHC*b* Monte Carlo is shown in Fig. 3.7.

The VELO is a silicon detector with 21 stations mounted in a vacuum vessel and separated from the LHC beam by a 200 μm-thick aluminium foil. The inner edge of the detector comes within 8 mm of the LHC beam. It has an $r-\phi$ geometry with alternating semi-circular layers of radial and azimuthal strips. Each semi-circular sensor has 2048 strips with a strip pitch in the $r-$modules that ranges from 40 μm closest to the beam line to 100 μm further out. The $r-\phi$ geometry enables fast 2D tracking in the trigger [43]. An illustration of the VELO sensors from reference [42] along with a picture of one of the completed VELO-halves is shown in Fig. 3.8.

Two of the planes of the VELO that sit upstream of the interaction region are used as a pile-up detector. Each plane has two overlapping r sensors that detect backward going tracks and the two planes estimate the position and number of primary vertices. This information is then used in the L0 trigger (see Sec. 3.7).

The performance of the VELO has been studied in simulations and in beam tests. The tracking efficiency of the VELO has been estimated at greater than 96%, with a ghost rate of 6.8%, and the spatial resolution of the VELO as better than 10 μm [45]. The pitch of the radial strips ensures that measurements along a track in the VELO contribute with equal weight to measurements of the impact parameter (IP)

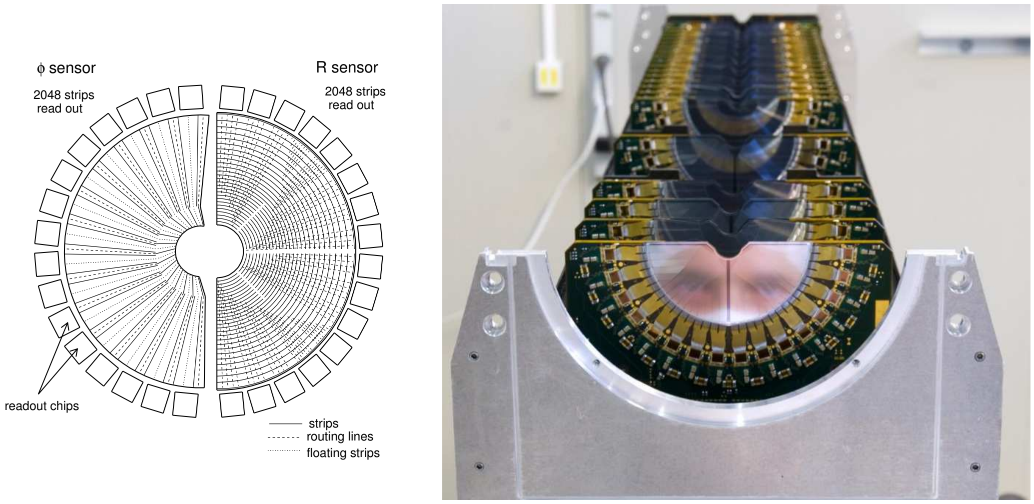

(a) (b)

Figure 3.8: Illustration of the $r - \phi$ geometry of the VELO sensor modules and a photograph of one of the completed VELO halves looking along the beam-line [44].

of the track. The IP resolution is expected to be $\sim 20\,\mu$m and the precision in the measurement of the lifetime of a B decay about 50 fs.

During injection and acceleration of the LHC beam, when the beam cross section is large, the VELO modules are retracted away from the circulating beam.

3.2.2 Trigger Tracker (TT)

Between the RICH 1 gas volume and the entrance to the magnet sits the Trigger Tracker (TT) [46]. It is a set of four planes of silicon strip detectors that are used in the early stages of the High-Level-Trigger (see Sec. 3.7) to make a transverse momentum measurement for tracks with large impact parameter. Hits in the VELO and TT are combined with the measured field integral between the VELO and the TT to estimate the momentum of charged particles to $\delta p/p \sim 20\%$. It is also invaluable for analysis of events with longer lived neutral particles (e.g. K_S^0) that will decay outside the VELO.

The TT covers the nominal LHC*b* acceptance of 300 mrad with silicon strip detectors, with a strip pitch of $183\,\mu$m. Silicon is used throughout the TT due to the high density of charged tracks. It also improves the granularity of measurements of high momentum tracks that only have a small magnetic deflection in the TT. In order to limit the amount of material in the detector and reduce radiation damage, the sensitive detector electronics are located outside the LHC*b* acceptance. The

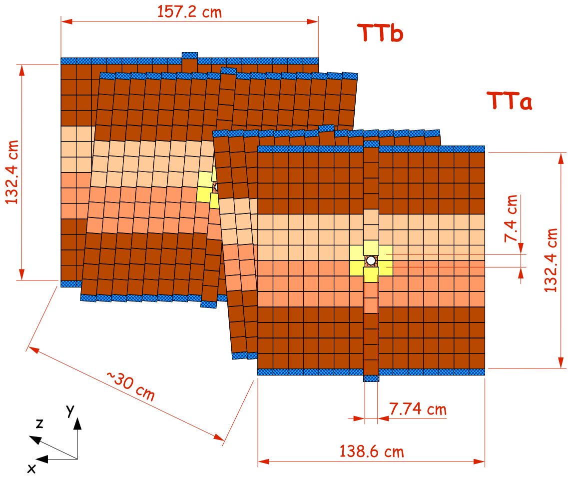

Figure 3.9: The position and orientation of the silicon strip detectors that make up the TT tracking station. There are 4 alternating planes oriented at 0°, 5°, -5° and 0°. From [46].

TT uses long Kapton cables to transfer signals from the silicon sensors outside the acceptance. Consequently, to maximise the signal-to-noise ratio, the sensors have a thickness of 500 μm.

The four layers of the TT are arranged at orientations of 0°, 5°, -5° and 0° with respect to the LHC*b* y-axis (the vertical axis), this is illustrated in Fig. 3.9. The tracking stations further down-stream have a similar orientation.

3.2.3 Tracking Stations

The tracking stations (T1-T3) sit downstream of the magnet and cover a large area (30m^2). The majority of this area is filled with straw tubes [47] but in the regions closest to the beam pipe where the occupancy is highest (20% of particles pass through just 2% of the area) silicon strip detectors are used instead. The silicon sensors are similar to those described for the TT in Sec. 3.2.2.

The straw tubes are 5 mm plastic tubes with a length of 2.4 m filled with an argon-carbon dioxide gas mixture. These have an average occupancy of 4.5% and a readout time of 75 ns, covering three LHC bunch crossings. The drift time for electrons to be collected at the central wire of the straw tube is measured with a precision of 2-3 ns. The resulting spatial precision of the outer region of the tracking stations has been measured at 200 μm in beam tests at both CERN and DESY [48].

3.3 RICH Detectors

For particle identification LHC*b* includes a pair of Ring Imaging Cherenkov Detectors that enable the separation of different long-lived charged hadrons (pions, kaons and protons). The RICH detectors of LHC*b*, RICH 1 and RICH 2, are described in detail in Chapter 4.

3.4 The Dipole Magnet

The dipole magnet [49] sits between the TT stations and tracking station T1. It is a warm coil magnet with an iron yoke and a 1.1T field pointing in the $\pm y$ direction[2] in the LHC*b* coordinate system (the z axis points along the LHC beam axis). This magnetic field will bend particles in the $x - z$ plane and provide a momentum estimate for charged particles. The acceptance of the magnet follows that of the LHC*b* detector. The vertex detector and muon chambers sit in a region of low magnetic field, providing straight track segments for the L0 and High-Level Trigger. A photograph of the LHC*b* dipole magnet, taken several years ago when the interaction region around interaction point 8 (IP8) was much emptier than it is now, can be seen in Fig. 3.10. A field map of the magnet field along z with $x = y = 0$ with both polarities is shown in Fig. 3.11. The field peaks at 1.1T at the centre of the magnet and the impact of the magnetic shielding of RICH 1 is clearly visible between 0 and 2 m. The position of the tracking stations and the VELO are also indicated on the figure.

3.5 Calorimetry

The main goal of the calorimeters in LHC*b* is to provide identification of electrons and hadrons for the trigger and analysis. The calorimeters comprise the following elements: upstream is the scintillating pad detector (SPD) followed by the preshower detector then the sampling electromagnetic calorimeter (ECAL) and finally the hadronic calorimeter. They are described in detail in reference [51]. The scintillating pad detector / pre-shower detector is two planes of 15 mm scintillator with 14 mm of lead sandwiched in between and is used to separate signals from electrons

---

[2] The polarity of the field can be swapped to reduce systematic effects in asymmetry measurements.

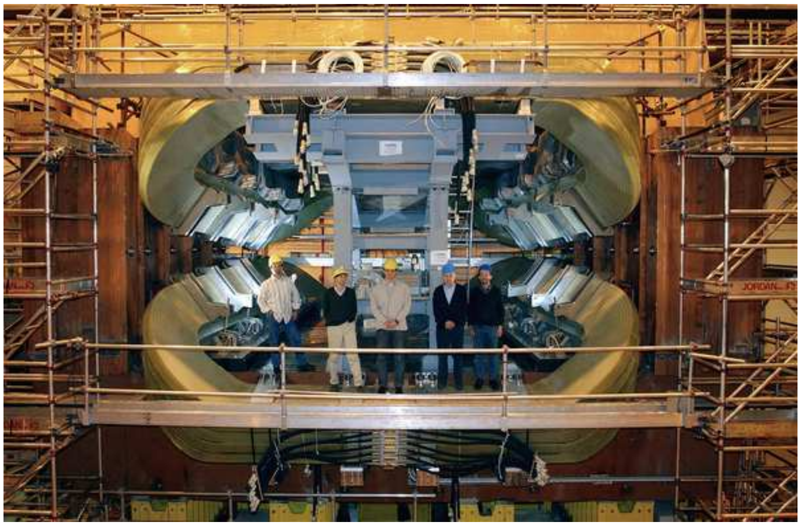

Figure 3.10: Photograph of the LHCb dipole magnet [50].

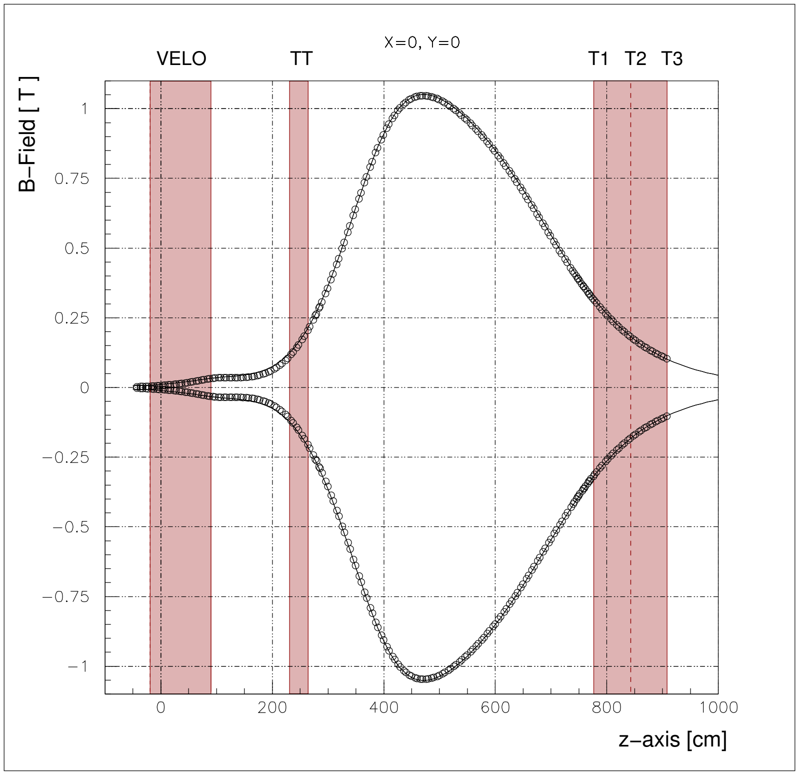

Figure 3.11: Measured B-field of the LHCb dipole magnet. The position of the VELO, TT and tracking stations have been indicated.

and photons with electrons leaving hits in both sets of scintillator and photons only in the second layer.

The ECAL is a Shashlik calorimeter with multiple layers of alternating lead absorber and plastic scintillator. Particle showers from the lead absorbers are sampled by the active, scintillator layer, and the signal read out through wavelength shifting fibres to photo-multipliers. With a thickness of 2 mm for the lead layers and 4 mm for the polystyrene scintillator the detector has a total thickness of 25 radiation lengths (X_0). The HCAL has a similar design with 6 mm iron plates and 3 mm scintillator layers for a total thickness of $\sim 65X_0$ and 7.3 interaction lengths (λ_I). Whereas the ECAL layers are oriented perpendicular to the beam direction, the HCAL layers are parallel. This is motivated by the significant lateral spread of hadronic showers compared with electromagnetic showers. For particle energy, E, in GeV the resolution of the calorimeters is expected to be:

$$\frac{\sigma_E}{E} \sim \frac{10\%}{\sqrt{E}} \oplus 1\%$$

for the electromagnetic calorimeter and

$$\frac{\sigma_E}{E} \sim \frac{80\%}{\sqrt{E}} \oplus 10\%$$

for the hadronic calorimeter. These have been verified in beam test measurements.

Neutral π^0, where both photons have a transverse momentum of $p_T > 200\,\text{MeV/c}$ relative to the beam line, can be reconstructed with an expected mass resolution of 10 MeV/c^2.

3.6 Muon System

There are five muons station, labelled M1 through M5 in Fig. 3.1. M1 sits between the second volume of the RICH detector and the pre-shower and M2-M5 behind the calorimeters. M2 through M5 are interleaved with iron absorbers to further reduce any background from charged hadrons (mainly pions) that may punch-through the back of the Calorimeters and into the Muon chambers.

Multi-wire Proportional Chambers (MWPC's) are used everywhere except in the inner region of M1 where the flux is highest (with a maximum rate around

500 kHzcm^{-2}). In the inner part of M1 triple-GEM (Gas Electron Multiplier) detectors are used instead.

The MWPC's are arranged in groups of four (anode) wires inside an Ar - CO$_2$ - CF$_4$ gas volume. The wires have a length of 20-30 cm, are spaced by 2 mm and sit between a pair of cathode plates separated by 5 mm. To maximise the efficiency of the detector the wires are ORed in pairs before reading them out. This provides an efficiency $\geq 95\%$ and a time resolution of 5 ns. The efficiency needs to be high as hits in four muon stations are required for the level-0 muon trigger.

The triple-GEM detectors contain three GEM foils sandwiched between anode and cathode planes. The anode is etched with read-out pads. Electrons are produced in the drift region between the cathode and first foil and are then accelerated by the electric fields between the three foils onto the readout pads at the anode. The GEM detectors have a typical efficiency above 96%.

The size of the pads in each of the stations is optimised to provide a precision measurement of the muon p_T for the level-0 trigger. Each station is divided into four regions with shorter wire chambers closest to the beam pipe and getting longer further out. The different stations are arranged to project back to the interaction region.

3.7 LHCb Trigger strategy

The LHC bunch-crossing rate is 40 MHz but due to the bunch structure and the LHCb design luminosity the rate of visible p-p collisions (those with one or more collisions and tracks from charged particles in the detector) is closer to 10 MHz. This 10 MHz is expected to contain roughly 100 kHz of events with $b\bar{b}$ pairs and only 15% of these will have the decay products of at least one of the b's in the LHCb detector acceptance. The job of the trigger is to cut the LHC event crossing rate of 40 MHz down to 2 kHz of events that are useful for physics analysis, control or calibration samples. These are written to tape for later analysis. Furthermore the interesting physics channels for many of the rare decays or CP violating channels have branching fractions $\mathcal{O}(10^{-4} - 10^{-9})$ and so the rate of B decays in exclusive channels must be cut even further.

The first level trigger, the so-called level-0 (L0) trigger, is a hardware trigger that cuts the rate to 1 MHz by cutting on the highest E_T clusters in the hadronic and

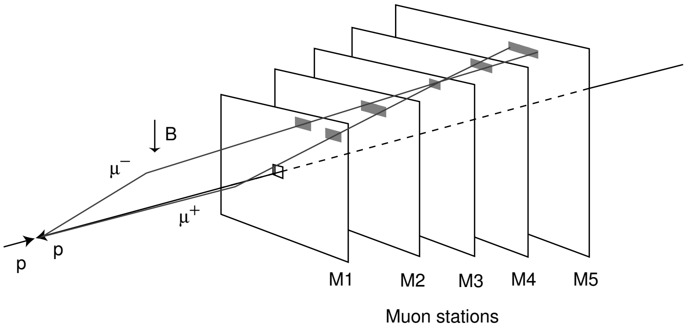

Figure 3.12: The L0 Muon Trigger. Hits are searched for in stations M2 and M3, these are then extrapolated to M4 and M5 using a field of interest about the track in M2 and M3. If hits are found in M4 and M5, then the track is confirmed then an extrapolation is made to M1. The straight track through M1 and M2 is used to determine the tracks p_T using a thin-lens approximation; that the track receives a p_T kick in x-z at the centre of the magnet.

electromagnetic calorimeters and the two highest p_T candidates in the muon system. It is described in detail in reference [52]. There is also a pile-up veto at L0 to veto events with more than one visible p-p interaction. The triggers are motivated by the relatively high mass and lifetime of the b-hadrons and their significant semi-leptonic branching fractions.

3.7.1 L0 Calorimeter Trigger

The L0 Hadron triggers make use of the SPD, the pre-shower, the ECAL and the HCAL. The aim is to search for large E_T particles; electrons, photons, π^0 or other hadrons. A distinction is made between each type of candidate particle using information from each sub-detector. Candidates are labelled as photons if they register hits in the Pre-shower but not in the SPD and electrons if they leave hits in the pre-shower and the scintillators of the SPD. Hadron candidates leave hits throughout the ECAL and also in the HCAL. The typical E_T cut on photons, electrons or hadrons in the L0 trigger is 2-3 GeV, i.e. about $m_B/2$.

3.7.2 L0 Muon Trigger

Events are triggered by the Muon Trigger if there is either a single high p_T muon candidate with a p_T greater than 1.3 GeV/c or a pair of muons with combined p_T greater than 1.5 GeV/c. Muon candidates are selected if they leave hits in M2 and M3 that can be matched to hits in M4 or M5 (see Fig. 3.12). Hits in M1 and M2 are then used to estimate the p_T of the muon candidate by projecting back towards the interaction region and assuming the track receives a p_T 'kick' in the $x - z$ plane at the centre of the magnet.

3.7.3 L0 Pile-up Veto

The L0 pile up system sits upstream of the VELO and uses a fast read out from four planes of silicon strip detectors. These planes of detector are used to estimate the number of primary interactions in a bunch crossing and reject events with multiple p-p interactions (where combinatorial backgrounds could fake a *b*-hadron decay). The pile-up system will also provide a measurement of the luminosity at IP8.

3.7.4 High-Level-Trigger, HLT

The second stage of the LHC*b* trigger is the High Level Trigger (HLT), a purely software trigger running on a PC farm. The HLT will receive events at 1 MHz from the L0 Trigger and to cope with this high rate the HLT will throw away events as soon as possible to minimise the amount of processing. The HLT selections are based on selecting high p_T, high E_T or high Impact Parameter (IP) objects. These cuts enrich the sample of particles with relatively high mass and displaced decay vertices.

The HLT is arranged in alleys, with each alley dealing with a different trigger type from the L0 trigger. For the majority of triggered events (85% for inclusive-b events) the event will have only passed a single L0 trigger and only this alley will be looked at. Within each of the alleys the structure is as follows:

- L0 confirmation. The result of the L0 trigger is confirmed by trying to match the L0 object to tracks in either the tracking stations or the VELO. Fast tracks are reconstructed in the VELO using the $r - \phi$ geometry to create 2D tracks using just the r-sensors. This is good for finding tracks with a high IP significance.

- The 2D candidates are combined with information from the ϕ-sensor to create 3D tracks. Muon candidates, using hits in the muon stations can be reconstructed with a momentum resolution of $\delta p/p \sim 4\%$. Tracks from other candidates (without hits in the muon stations) are reconstructed using hits in the TT to gain a momentum resolution of $\delta p/p \sim 20\%$.

Name	Rate	Description
Dimuon	600 Hz	Dimuon with an invariant mass above 2.5 GeV. These are used to estimate uncertainty on life-time measurements and for tracking studies
Inclusive-b	900 Hz	Events with a single high p_T or high IP muon. that can be used for systematic or tagging studies.
Inclusive charm	300 Hz	Including a D^* stream where the D^0 from the D^* decays to a pair of charged hadrons. These are used for calibration of the RICH detector.
Exclusive events	200 Hz	Core physics channels, including control channels and side bands

Table 3.1: Streams written to tape from the high level trigger.

- Pre-trigger. The 3D tracks (and a confirmed L0 object) are combined and the event passed if either a single track or combination of tracks has significant p_T or IP.
- Trigger; with an output rate of 10 kHz.

The principle is illustrated in Fig. 3.13. At this stage the tracks from the HLT are combined to form composite particles, e.g. $K^{*0} \to K^+\pi^-$ or $J/\psi \to \mu^+\mu^-$. The final rate to tape is 2 kHz and this is achieved by fully reconstructing the B (or other high mass) candidates that will later be used in the various physics analyses. The HLT reconstruction does not have access to particle ID information from the RICH, and the quality of the reconstructed tracks is lower than can be achieved offline ($\delta p/p \sim 1\%$ compared with 0.38% offline). This is due to the time constraints in performing the full track fit, unpacking the RICH information and performing the global particle ID online. There are four data streams written tape from the HLT, details of which are provided in Table 3.1.

3.7.5 Trigger Performance

Using the full detector simulation, described in Sec. 7.3, the L0 trigger efficiency to select events containing $B_d \to K^{*0}\mu^+\mu^-$ decays that can be reconstructed and selected offline can be estimated at 93%. This is typical of the performance on simulated events containing b-hadrons that decay with at least one muon. The

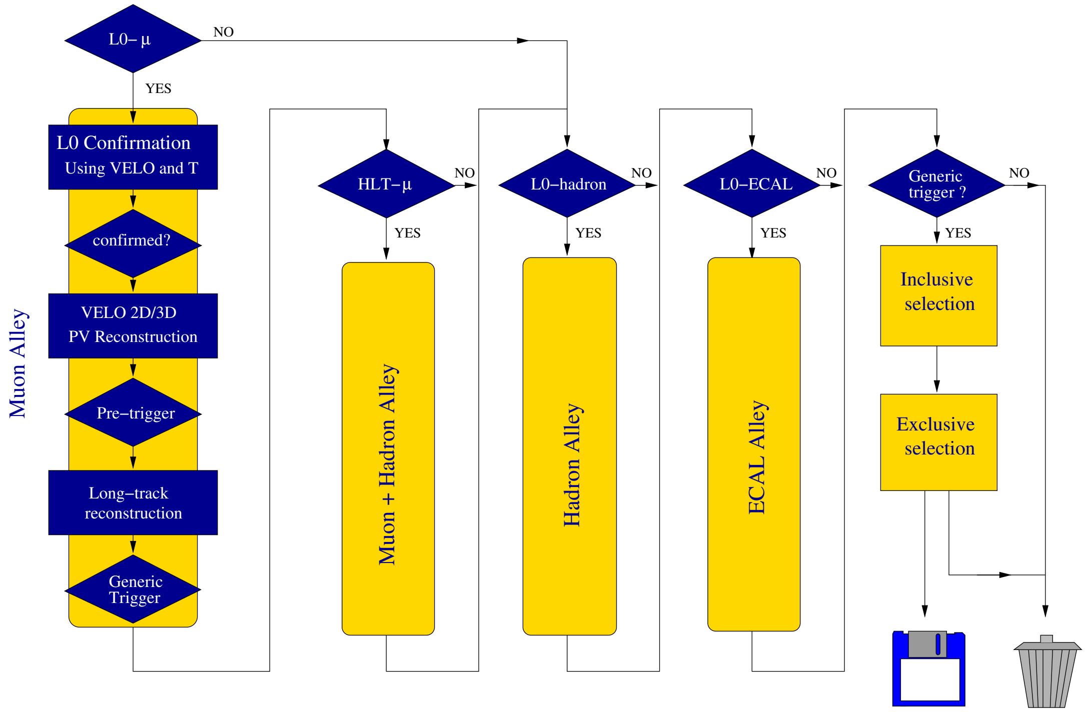

Figure 3.13: Overview of the alleys of the High Level Trigger.

efficiency for passing purely hadronic B decays at L0 is lower and is typically between 50 and 60%. One such example is the benchmark channel $B^0 \to \pi^+\pi^-$, used in CP measurements, which has a L0 efficiency of 54% [52]. At the time of writing, the HLT is in a constant state of flux, however some figures of merit can be found in references [52] and [53]. A large part of the HLT bandwidth is given to calibration samples to provide a high purity sample of $b \to \mu X$ and D^* events for tracking, particle ID calibration and flavour tagging studies. The exclusive selections for the specific physics analyses are designed to achieve a $\sim$ 90% efficiency with respect to the offline reconstructed and selected candidates whilst maintaining a purity around 90%. They apply a set of selection cuts that are similar to those used in the offline analysis. For $B_d \to K^{*0}\mu^+\mu^-$ and $B^0 \to \pi^+\pi^-$ decays the efficiency is $\sim$ 94%. When processing events generated as a minimum bias sample, more than 70% of events that are selected by the HLT contain a heavy quark (either b or c). This should be compared with just 6% of events before the HLT.

Chapter 4

The RICH detector

Charged Hadron identification, at the 3σ level (of separation), over the momentum range 2-100 GeV/c is provided by Ring Imaging Cherenkov (RICH) detectors. Fig. 4.1 shows the characteristic Cherenkov angle versus particle momentum for three radiators used in LHCb. These are a solid silica aerogel radiator and two gas radiators; C_4F_{10} and CF_4. As the particle momentum increases it becomes increasingly difficult to separate $\pi^{\pm}$ and $K^{\pm}$ in a single radiator. The combination of the three radiators allows $\pi - K$ separation over the desired range.

Two different RICH detectors are used to cover the desired phase space. At larger angles to the beam pipe the momentum spectrum of particles in LHCb is softer. This is demonstrated in Fig. 4.2. The figure plots the polar angle of $\pi^{\pm}$ from $B^0 \rightarrow \pi^+\pi^-$ decays against their momentum and shows that the full geometrical acceptance is only needed for the lower momentum particles.

The upstream RICH detector (RICH 1) covers particles with momentum between 2-60 GeV/c and the downstream detector (RICH 2) covers the high momentum particles from 17-100 GeV/c. RICH 1 covers the full LHCb acceptance of 25 mrad to (250) 300 mrad in the (non-) bending plane. RICH 2, which is located after the magnet and tracking stations has a smaller acceptance of (100) 120 mrad.

Particles entering the radiator volumes of the RICH detector produce Cherenkov light in a cone that is focused into a ring image and onto a plane of photon detectors located outside the detector acceptance by the combination of spherical and flat mirrors.

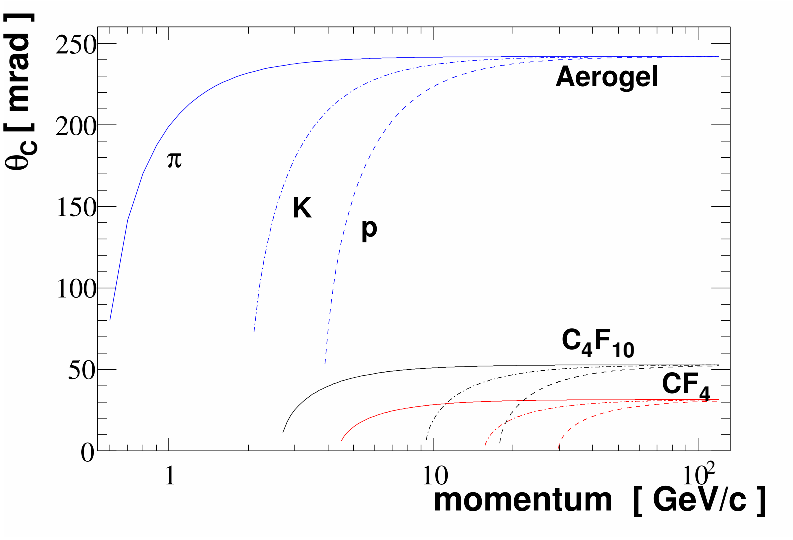

Figure 4.1: The Cherenkov angle associated with Cherenkov light produced by $\pi^{\pm}$, $K^{\pm}$ and protons in the three radiators used in the LHC*b* RICH detectors.

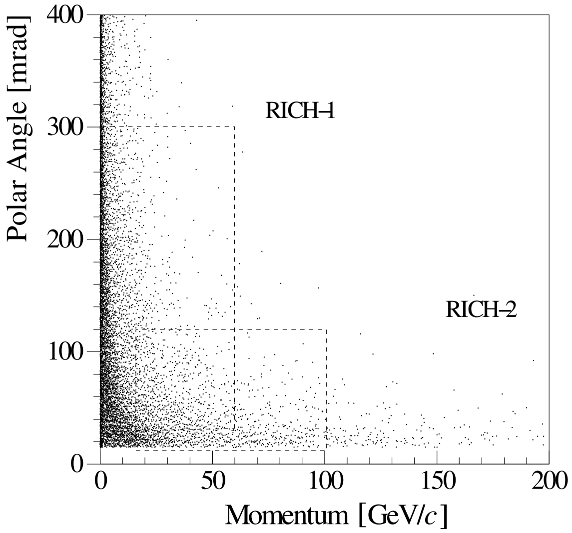

Figure 4.2: Polar angle θ versus momentum for $\pi^{\pm}$ from $B^0 \to \pi^+\pi^-$ decays in the LHC*b* detector.

4.1 Cherenkov Radiation

The Cherenkov effect occurs when a charged particle traverses a dielectric medium with a phase velocity ($v = \beta c$) greater than the velocity of light in that medium (c/n) where n is the refractive index. The material then becomes polarised, coherently emitting radiation with an emission angle

$$\cos\theta = \frac{1}{\beta n} \quad .$$

The spectrum of the emitted radiation is given by the Frank-Tamm relation

$$\frac{d^2N}{dE\ dx} = \frac{\alpha}{\hbar c} Z^2 (1 - \frac{1}{\beta n})$$

corresponding to the number of photons per unit length of material traversed with energies between E and $E + dE$, where Ze is the charge on the particle. In practice the optical medium will have a refractive index that depends on the photon energy.

4.2 RICH 1

The upstream rich detector is located close to the LHCb dipole magnet. To protect the photon detectors from the fringe field of the magnet they are surrounded by a 100 mm-thick iron shield. Without the shielding the magnetic flux density in the detector plane would be about 60 mT. With the shielding in place this is reduced to 2.4 mT.

A schematic diagram of the RICH 1 detector is shown in Fig. 4.3. RICH 1 employs two radiators to cover the lowest momentum particles; silica aeorogel and a C_4F_{10} gas radiator. These provide momentum coverage between 2-60 GeV/c. RICH 1 has a very light-weight construction with carbon-fibre reinforced plastic mirrors (that sit inside the acceptance) and a light-weight exit window. The entrance window is eliminated by sealing directly to the VELO vacuum tank outside the acceptance. Including the radiators it accounts for 8% of a radiation length. By the time particles pass through the last of the tracking stations they have passed through 60% of a radiation length (20% of an absorption length).

The low Cherenkov photon yield means that it is important to maintain a high reflectivity for the mirrors, particularly in the UV. The spherical mirrors have a coating of 160 nm-thick $\mathrm{Al} + \mathrm{MgF_2}$. The mirror is assembled in four segments around the beam pipe. The flat mirrors are located outside the detector acceptance as two planes of eight rectangular mirror segments. For this reason a light-weight construction is not necessary and 8 mm-thick glass is used with a coating of $\mathrm{Al} + \mathrm{SiO_2} + \mathrm{HfO_2}$. The optical quality of the RICH mirrors is such that they provide a negligible contribution to the Cherenkov angle resolution.

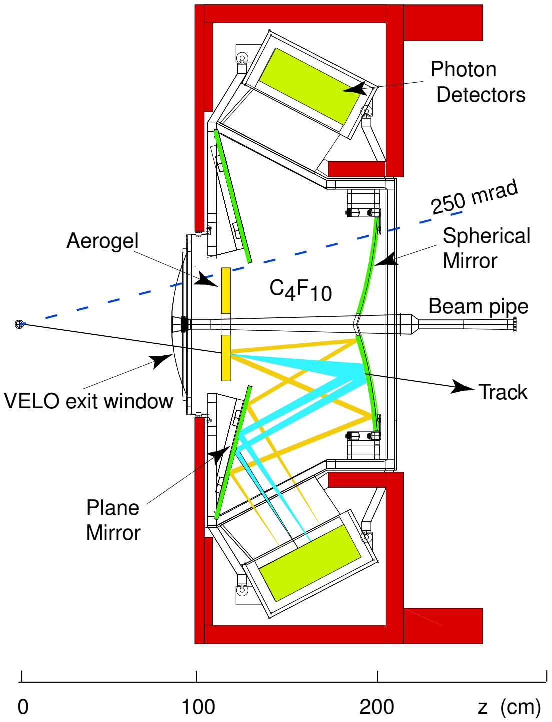

Figure 4.3: A schematic overview of the RICH 1 detector. Charged particles entering the detector from the VELO pass through a silica aerogel and C_4F_{10} gas radiator and coherently produce Cherenkov photons if they are above the Cherenkov threshold. These photons are focused by a combination of a spherical and plane mirrors onto a plane of photon detectors that sit outside the LHC*b* acceptance.

4.3 RICH 2

The second RICH detector, RICH 2 sits downstream of the magnet and tracking stations. It contains a CF_4 gas radiator and contributes to separation of higher momentum particles, up to and beyond 100 GeV/c. The RICH 2 detector has essentially the same geometry as RICH 1 (see Fig. 4.3) but rotated by 90° about the beam axis. The material requirements are less severe and 6 mm glass-substrate mirrors are used for the spherical and plane mirrors. The spherical mirrors comprise 56 hexagonal pieces and the plane mirrors 40 rectangular pieces with the same reflective coating that is used on the RICH 1 plane mirrors.

4.4 Hybrid Photon Detectors

The photon detectors for the LHC*b* RICH are pixel hybrid photon detectors (HPDs) [54] built in close collaboration with industry[1]. They are a vacuum device in which

---

[1] The main industrial partner is Photonis-DEP, NL-9300 AB Roden, Netherlands.

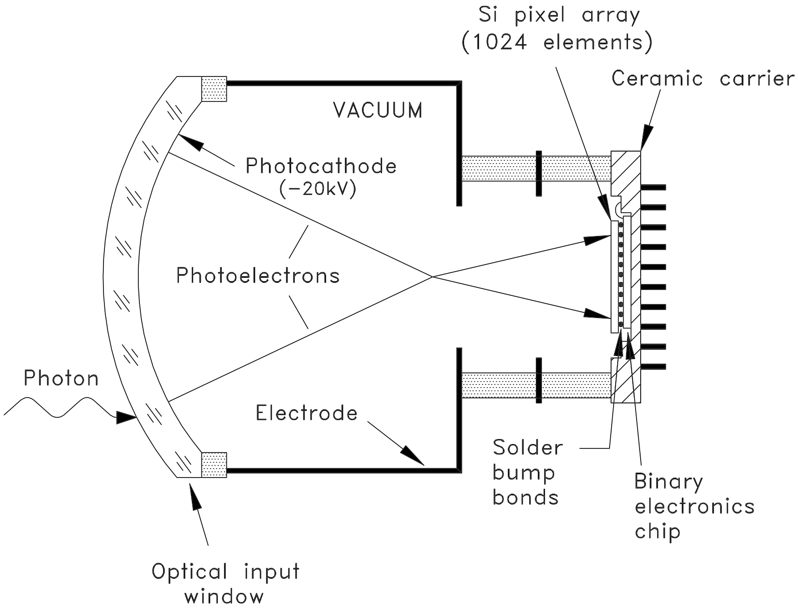

Figure 4.4: Schematic view of a HPD. Photoelectrons produced when photons strike the photocathode are accelerated through the HPD's electrostatic fields (with the photocathode at -20kV and two further electrodes at -19.7kV and -16.4kV) and focused onto a silicon pixel sensor with a binary readout.

photons are converted in a thin multi-alkali photocathode deposited on the inner surface of a quartz window. The photoelectrons are accelerated by a tetrode structure of electrodes onto a reverse-biased silicon pixel sensor that is encapsulated inside the vacuum tube. This provides an efficient, low-noise device that is single photon sensitive in the range 200-600 nm. A schematic of the HPD is given in Fig. 4.4. The outer diameter is 83 mm and the HPD length 110 mm.

The photocathode voltage is 20 kV with two further electrodes at 19.7 and 16.4 kV. This results in an image that is cross-focused and demagnified by a factor of 5 on the silicon anode. The image point-spread is estimated by simulation to be 80 μm in the red and 180 μm in the blue-near UV. This has been confirmed by laboratory measurements and is discussed in greater depth in Sec. 5.6.

The silicon pixel sensor is segmented into 8192 pixels that are arranged as an array of, 256×32, 62.5 μm by 500 μm pixels and is bump-bonded onto a digital binary-readout chip (the LHCbPIX1 chip [55]). For LHC*b* these 8192 pixels are grouped (logically-ORed) into 1024 'super-pixels'. Each super-pixel contains 8, 62.5 μm × 500 μm, sub-pixels to form a 32×32 array of square, 500 μm by 500 μm pixels. Each sub-pixel has its own readout electronics and individual sub-pixels can be read-out separately, albeit at a lower rate. The LHCbPIX1 chip will be used in this mode by ALICE for its inner tracker. When the demagnification of the HPD image is taken into account the HPD provides a spatial resolution of 2.5 mm by 2.5 mm in the photon detector plane.

The binary readout chip, the LHCbPIX1, is fabricated in a commercial 0.25 μm CMOS technology. A block diagram is given in Fig. 4.5. The basic functionality of the chip is to readout and digitize hit pixels where the charge deposited by the photoelectrons is above a preset threshold. The analogue components are a differential pre-amplifier followed by a shaper with a typical shaping time of 25 ns (one LHC bunch crossing) and a threshold discriminator with a three-bit threshold adjust.

The threshold adjust enables the individual pixel thresholds to be adjusted to optimise the efficiency of the HPD. One electron-hole pair will be produced per 3.6 eV deposited in the silicon sensor and taking the 150 nm n^+ ohmic contact into account (which acts as a dead layer), the typical signal size will be $5000e^-$. The global threshold is set by a DAC on the pixel chip and is measured by injecting charge through the test capacitor in Fig. 4.5. The pixel threshold at a particular voltage is taken as the 50% point on the S-curve turn on of the pixel sensor. The average threshold is measured as $1063 \pm 100e^-$ and is chosen to be well separated from the noise, measured as $145 \pm 12e^-$. It is also well below the typical signal size, even when charge sharing occurs between neighbouring pixels. The pixel noise is dominated by the electronics noise of the pixel readout.

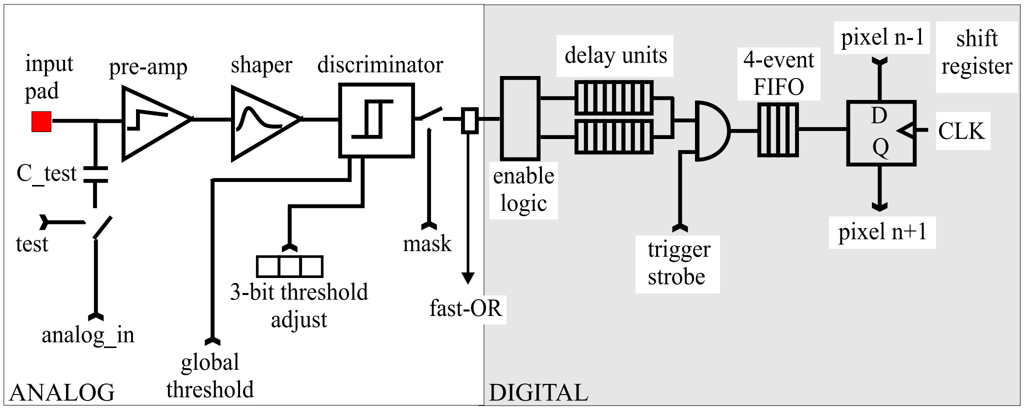

Figure 4.5: The block diagram for a single sub-pixel of the LHCbPIX1 chip. The analogue part is a shaping stage with a 25 ns peaking time and threshold discriminator. The digital part first makes a logical OR of sub-pixels and then delays the readout for the trigger latency of 4 μs. The event is read out on the receipt of a strobe.

The digital part of the pixel chip has a pipeline depth of 4 μs, that is compatible with the latency of the LHCb L0 trigger. The digital cell is clocked at the LHC bunch-crossing frequency of 40 MHz and triggered (through the strobe in Fig. 4.5) at the LHCb L0 trigger rate (1 MHz).

The photon-detector planes of the RICH detectors are hexagonally close-packed arrays of HPDs with a HPD pitch of 89 mm. They are arranged as 14 rows of 14 HPDs in RICH 1 and 18 columns of 16 HPDs in RICH 2. These columns contain all of the on-detector electronics (see Sec. 4.5). Each HPD is mounted inside a cylindrical Supra-36 (RICH 1) or Mumetal (RICH 2)[2] tube with kapton[3] insulating the grounded tube from the 20kV photocathode. This shielding is required to protect the HPDs from any residual field that remains inside the iron shield from the fringe field of the dipole magnet. This is described in more detail in Sec. 5.8.

4.5 Readout Electronics

On the columns of the RICH detector the HPDs are grouped in pairs. Each pair of HPDs shares a single 'Level-0' front-end readout board. Data from the HPDs is read out through a passive translator board and kapton cable. The Level-0 board [56] acts as an interface between the HPDs and the experimental control system, TFC (timing and fast control) and data readout system. It also sets the configuration of the pixel chip through a JTAG interface. The functionality of the Level-0 is implemented on a field programmable gate array (the PINT). The data from the pair of HPDs is then formatted by the Level-0 board, multiplexed onto two optical links and transmitted off detector at 1.6 GHz to the 'Level-1' electronics. The Level-0 board also incorporates a TTCrx (TTC receiver [57]) which receives the clock from the global TFC system and generates the 40 MHz clock, trigger and calibration systems for the pixel chip.

Low and high voltage distribution boards are also mounted at the front-end. The low voltage boards generate the reference voltages needed by the HPDs and the Level-0 boards. One in four low voltage boards has a SPECS slave [58] that provides an interface to configure the Level-0 boards and HPDs. The high voltage distribution boards, through a series of resistors, provide the three high voltages required by the HPDs (derived from a single 20kV input).

---

[2] Supra-36 and Mumetal are nickel-iron alloys with high magnetic permeability. Their high permeability makes them ideal for screening magnetic fields. Supra-36 is 36% nickel and Mumetal ∼80%.

[3] Kapton is a polyimide film developed by DuPont. It is used extensively in flexible printed circuits and as an electrical insulator.

	RICH 1 Aerogel	RICH 1 C_4F_{10}	RICH 2 CF_4
Chromatic error	2.4	0.9	0.5
Emission point error	0.4	0.8	0.4
HPD pixelisation	0.5	0.5	0.2
HPD image spread	0.5	0.5	0.2
Tracking error	0.4	0.4	0.4
Total	2.6	1.7	0.8

Table 4.1: Contributions to the Cherenkov angle resolution (in mrad) on a single photon in the RICH detectors.

The Level-1 electronics, implemented on the UKL1 board, sits off-detector in the counting room. This performs further data formatting and data reduction (in the form of zero suppression) and acts as the interface between the RICH detector and LHC*b*'s global acquisition system. Data from 36 HPDs, arranged as 3 × 12 fibre ribbons, is multiplexed out over four Gigabit ethernet cables. Information from the RICH detectors is not used in the HLT and will only be used in subsequent offline event reconstruction.

4.6 RICH Detector Performance

The performance of the LHC*b* RICH detectors has been evaluated by carrying out a full simulation of the detectors, using a realistic description of the materials in the detector and the physics processes involved. Details of this simulation can be found in reference [59]. The performance has also been verified in beam tests. Saturated tracks, where $\beta \sim 1$, produce an average of 6.8 photons in the aerogel, 21.9 in CF_4 and 30.3 in C_4F_{10}. The Cherenkov angle resolution (per photon) for each of the radiators is presented in Table 4.1. These resolutions receive contributions from: chromatic dispersion in the radiator, the uncertainty on the emission point of the photon (along the track), tracking missalignments and the HPD pixel size and image point spread. The image spread in the HPD electron optics will be discussed in Sec. 5.6.2. The resolution in aerogel is dominated by chromatic dispersion but for CF_4 and C_4F_{10} the contributions are more balanced. Chromatic dispersion determines the sensible, minimal, pixel size of the HPDs pixel sensor.

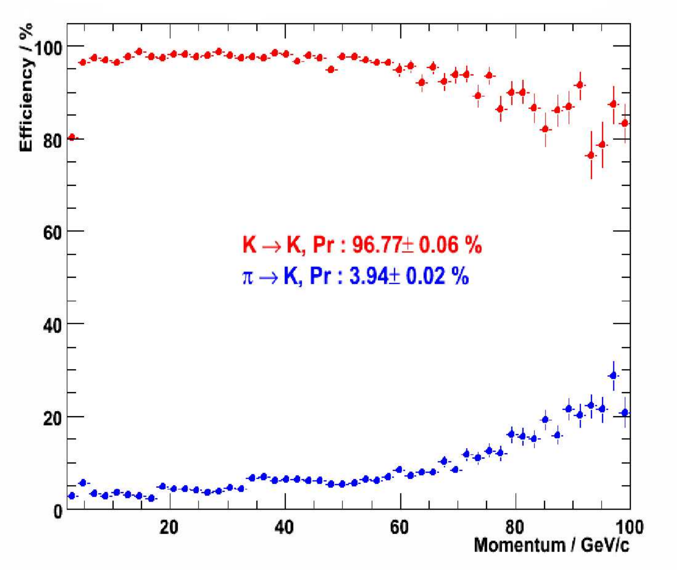

Figure 4.6: Particle identification performance of the LHCb RICH detectors to identify light ($e^{\pm}$,$\pi^{\pm}$) and heavier particles ($K^{\pm}$,p).

4.7 Particle Identification

There are two approaches to pattern recognition and particle identification in the RICH detectors [60], a local and a global approach. In the local approach each track is treated separately and hits from the photon detector plane are mapped by solving a quartic equation for the mirror system back to the photon emission point. This is assumed to be the centre of the radiator. The track trajectory is then used to estimate the Cherenkov angle θ_C. The velocity and momentum estimates are then used in a likelihood fit for the particle hypothesis.

In the global approach the trajectories of the particles, from the tracking, through the radiators is used to define an expected distribution of hits on the photon detector plane for each particle hypothesis. All tracks are considered simultaneously in a global maximum-likelihood fit and this takes into account background coming from overlapping rings from nearby tracks.

In both cases the dominant background in the RICH detectors is from real Cherenkov photons that have no associated track. The overall performance of the RICH detectors is illustrated by Fig. 4.6.

Chapter 5

HPD Performance in Laboratory Tests

This chapter describes a series of measurements, performed by the author, on the first production HPDs. These measurements address the requirements of the HPD, discussed in Chapter 4 and are used to provide data to inform the simulation of LHC*b*'s PID performance (Fig. 4.6), to predict the performance of the detector in beam tests (Chapter 6) and, along with measurements on a set of pre-series HPDs, to specify a programme of testing for the full production of HPDs. The production HPDs are characterised at one of two test centres in Scotland[1].

The HPD measurements described here include:

- Efficiency for photon detection.
- Charge sharing.
- Noise performance.
- Vacuum quality.
- Spatial precision of the electron optics.
- Magnetic field effects.

---

[1] The University of Edinburgh and the University of Glasgow.

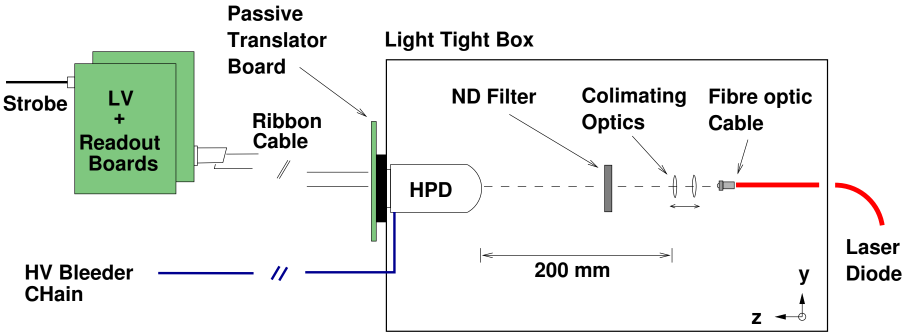

Figure 5.1: Laboratory setup for the HPD testing at CERN. The HPD is mounted inside a light-tight box and illuminated by a short pulsed laser diode or LED.

Throughout this chapter the terms LHC*b*-mode and ALICE-mode are used to distinguish the two different readout modes of the HPD. In ALICE-mode, all 8192 $62.5\,\mu\text{m} \times 500\,\mu\text{m}$ sub-pixels are read out, whereas in LHC*b*-mode the eight-fold OR of the sub-pixels results in 1024 super-pixels. Where appropriate the result of the full production testing is quoted. Details of the tests on the pre-series HPD's can be found in references [61] and [62].

5.1 Experimental setup

The laboratory setup for the HPD testing is shown diagrammatically in Fig. 5.1. It is essentially a light-tight box into which the HPD and a light source are mounted. A short fast-pulsed red laser diode ($\lambda = 628\,\text{nm}$), with a FWHM of 100 ps, is used to illuminate the HPD. This laser is situated outside of the light-tight box and the light is guided into it via a fibre optic cable. The end of the fibre is mounted, along with a set of collimating optics, on an *'x-y'* translation stage that allows the position and size of the laser spot on the HPD's quartz window to be adjusted. By adjusting the optics it is possible to achieve both a collimated beam with a waist of 0.3 mm and to illuminate the entire photocathode surface. For some of the measurements the fast-pulsed laser was replaced by a blue ($\lambda = 460\,\text{nm}$) DC LED. A neutral density (ND) filter, with a transmission of 1%, is placed in front of the translation stage to reduce the intensity of the light from the laser (which is nominally 0.5 mW).

The electronics in the laboratory setup is similar to that of the final RICH detectors; discussed in Sec. 4.5. The HPD sits in a zero-insertion force (ZIF) socket on a passive translator board and the three high-voltages to the HPD are provided by a resistive bleeder chain with a single input, variable up to 20 kV. A pair of electronics boards is used to provide the low voltage references to the HPD and the control signals to read out the data from the pixel chip. These boards sit outside the light-tight box and function in the same way as the Level-0 and low voltage boards of the final RICH electronics. Data from the pixel chip is then passed from the translator board to the readout board and then further onto a data acquisition card [63] in a PC running LabVIEW[2] [64]. This combination effectively performs the same role as the front-end Level-0 board, the Level-1 board and global acquisition system in LHC*b*.

Measurements have been taken in both the standard LHC*b* and the ALICE operating modes of the HPD, with both a 25 ns and a longer 50 ns or 500 ns readout strobe. In each of the configurations the same signal is used to generate both the strobe (the readout signal) and to trigger the laser diode. The delay between the laser emitting a pulse of light and the strobe was adjustable using NIM electronics.

Fig. 5.2(a) demonstrates the image formed in ALICE-mode when the laser is allowed to diverge and cover the entire photocathode and (b) when the laser is focused onto a small spot on the photocathode (the red spot that is offset from the centre of the HPD). The concentric rings in the Fig. 5.2(a) result from reflections from a chromium contact at the edge of the quartz window that connects the HV supply to the photocathode.

5.2 HPD simulation

In order to guide the interpretation of the experimental measurements a simulation of the HPD electron optics and charged particle trajectories was also carried out. The simulation of the field inside the HPD is carried out in a CERNLIB program, POISCR [65]. This program is designed to solve the Poisson and Laplace equations and provides a model for the electric field $\vec{E} = (E_r, E_\phi, E_z)$ in the HPD. This field map is then used in a separate stand-alone piece of code to calculate the trajectory of electrons through the electrostatic field.

The trajectories of photoelectrons (or ions) inside the vacuum tube are calculated by solving the equation of motion, in cylindrical polar coordinates.

---

[2] LabVIEW is a trademark of the National Instruments.

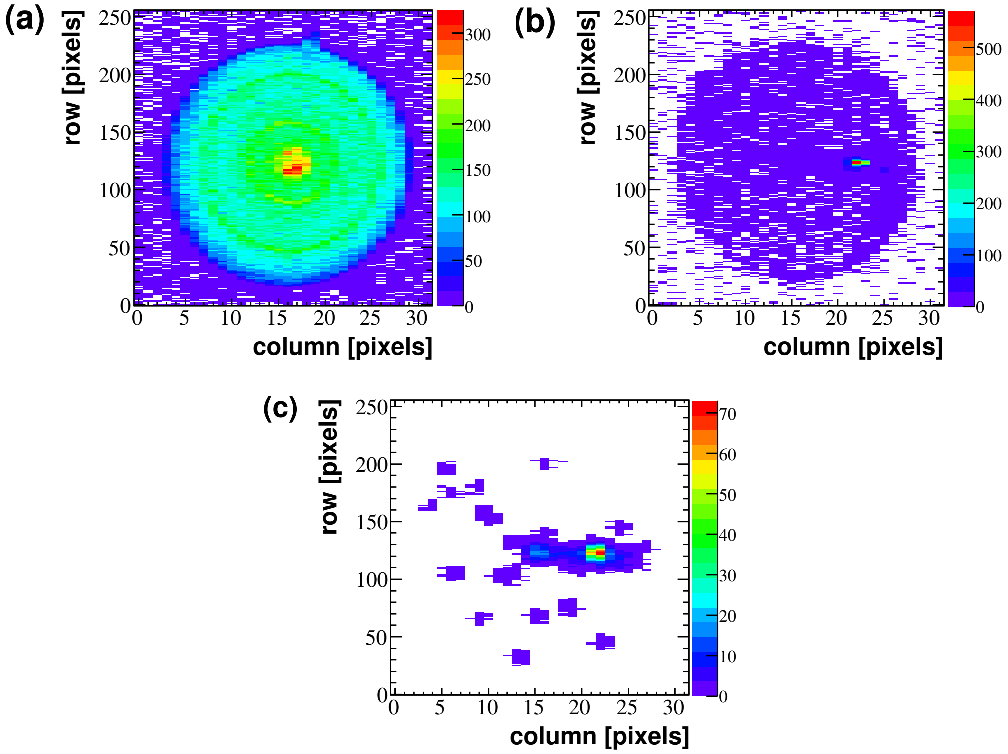

Figure 5.2: *(a)* The image formed on the silicon pixel sensor (in ALICE mode) when illuminating the entire photocathode. *(b)* The image formed when the laser has been focused and offset by 20 mm on the photocathode and *(c)* with the laser spot in the same position, the position of large (> 10 pixel) clusters on pixel sensor.

$$\ddot{r} = \frac{q}{m}E_r + r\dot{\phi}^2$$

$$\ddot{z} = \frac{q}{m}E_z$$

$$\ddot{\phi} = -\frac{2\dot{r}\dot{\phi}}{r}$$

where q is the charge on the photoelectron (or ion) and m is its mass. The field in the HPD is symmetric about the tube's axis, with no E_ϕ component. In the presence of an external magnetic field these equations will each gain an extra term coming from the $q\vec{v} \times \vec{B}$ term of the Lorentz force.

The equations were solved using a second order Runge-Kutta method in which time steps of 1 ps were used. It proceeds by taking a half-step in one of the variables

$$f^{t+\delta t/2}(r, \phi, z) = f^t(r, \phi, z) + \frac{\delta t}{2}\dot{f}^t(r, \phi, z) \quad ,$$

where f denotes either r, ϕ or z and then a step

$$f^{t+\delta t}(r, \phi, z) = f^t(r, \phi, z) + \delta t \dot{f}^{t+\delta t/2}(r, \phi, z) \quad .$$

The initial velocities of the photoelectrons are chosen according to:

- a Maxwellian distribution in energy with a maximum energy $h\nu - E_{thr}$, where $E_{thr} = 1.5\,\mathrm{eV}$.
- a Lambert cosine distribution in emission angle, $\frac{dN}{d\Omega} \propto \cos\theta$.

Further details can be found in reference [66]. The trajectories of particles from eight starting positions on the photocathode are shown in Fig. 5.3. The figure also includes the position of the photocathode and the 19.7 and 16.4 kV electrodes.

5.3 HPD Efficiency

The efficiency of the HPD is a product of three components:

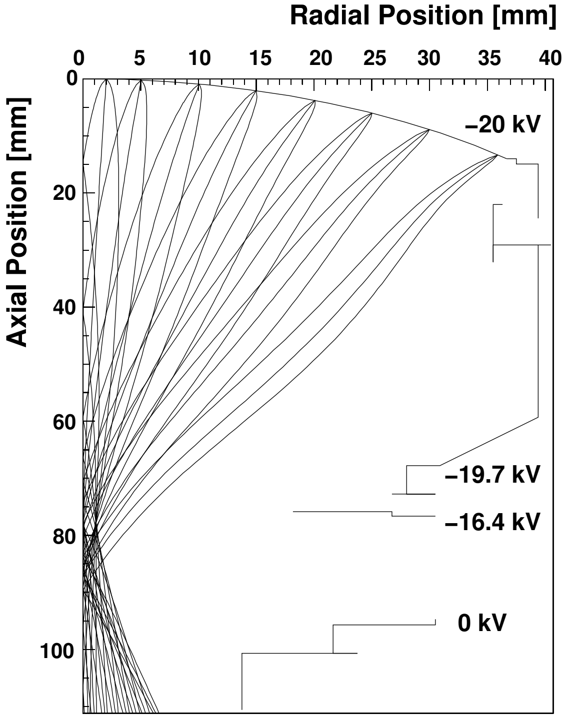

Figure 5.3: The simulated trajectories (in the absence of any external field) followed by photoelectrons emitted from eight different positions on the HPDs photocathode. At each position the spread in trajectories from photoelectrons emitted at +45°, 0° and -45° to the surface normal is illustrated.

- The quantum efficiency of the HPD's photocathode (and its quartz window transmission).
- The charge collection efficiency of the electron optics. This is greater than 98%.
- The efficiency for detecting the photoelectrons at the silicon pixel sensor.

By far the largest of these inefficiencies is product of the HPD's quantum efficiency (QE) and window transmission. It peaks at a wavelength of 270 nm (in the UV) at an average value of 31%, is small in the red (due to the QE of the photocathode) and is cut-off below 180 nm by the quartz transmission. The combination is measured by the manufacturer from the photocathode current using a light source and calibrated photodiode. A typical curve for one of the HPDs is given in Fig. 5.4.

The most significant contributions to the efficiency of the pixel chip are from: two photoelectrons striking the same binary pixel, charge sharing between neighbouring pixels that lead to a pixel being below threshold and photoelectrons that are Rutherford backscattered in the silicon sensor (see illustration in Fig. 5.5). The

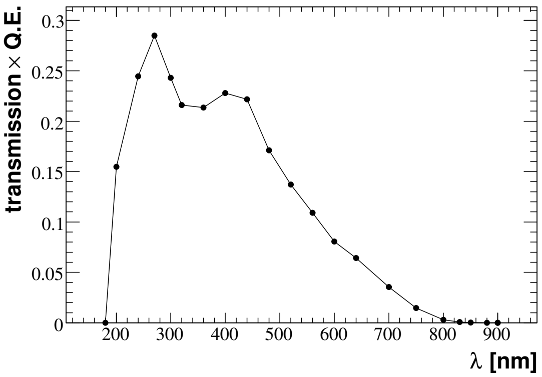

Figure 5.4: The combined quartz window transmission and photocathode quantum efficiency for one of the HPDs used in the testbeam at the CERN SPS (measured by the manufacturer).

typical probability for a 20 keV electron to be backscattered from the silicon sensor is expected to be 18% [67]. In many cases the backscattered photoelectron will still deposit enough charge for the pixel signal to exceed the threshold.

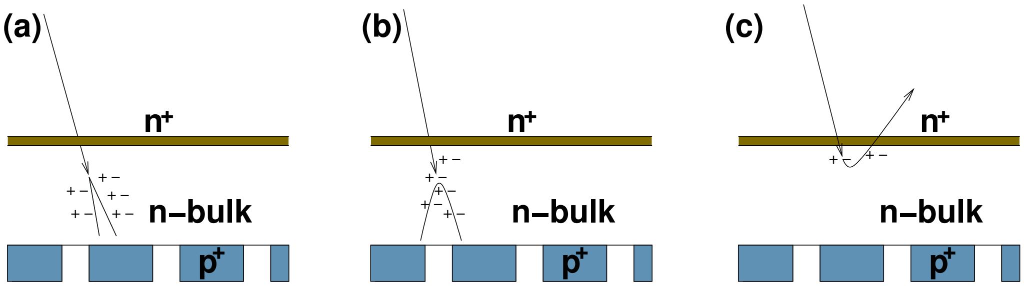

Figure 5.5: The HPD pixel sensor has a n-type bulk, with an n^+ ‘dead’ contact layer and charge is collected at the p^+ pads. A schematic of the pixel sensor is given in (a). The charge deposited in a single pixel can be reduced if there is charge sharing between adjacent pixels (b) or the photoelectron is Rutherford backscattered (c).

In the laboratory setup the readout efficiency has been assessed by comparing the number of pixel hits, in a 50 ns window, to the analogue pulse height spectrum of the full silicon sensor (measured at the n^+ back plane). This is achieved by using a fast amplifier and an ADC[3] in coincidence with a long gate. The gate is provided by the same signal that is used to trigger the fast pulsed laser. An example pulse height spectrum is given in Fig. 5.6. The poor separation between the peaks is due to the large (approximately 60 pF) back-plane capacitance of the pixel chip, resulting in high noise at the amplifier input. This noise is not relevant for the individual pixel readout. The analogue spectrum is fitted with a convolution of a single photoelectron response function and a Poisson distribution for the number of photoelectrons

---

[3] An ORTEC 926 ADC.

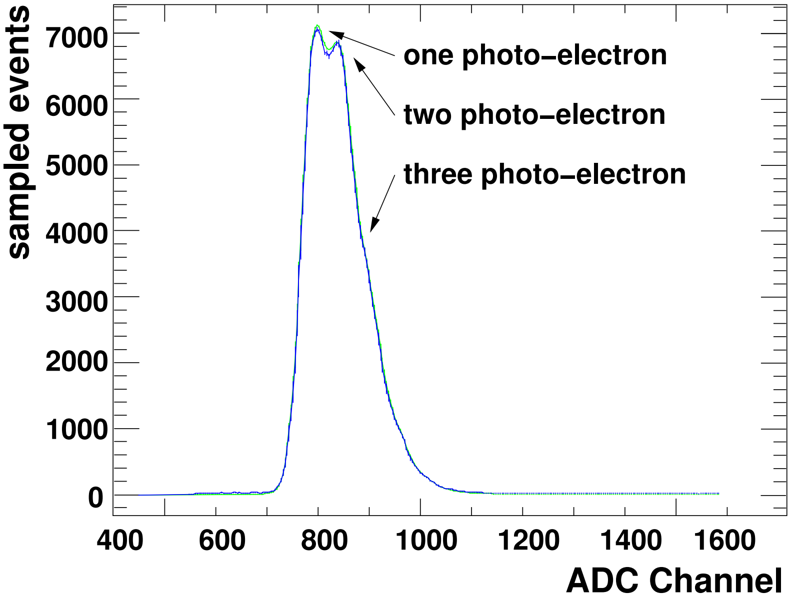

Figure 5.6: The analogue pulse height spectrum from the full silicon pixel sensor, read through an amplifier connected to the n^+ backplane. The photoelectron peaks are not well separated due to the large back-plane capacitance of the pixel sensor, but the one, two and three photoelectron peaks are visible. Overlaid is a fit to the spectrum.

(per trigger). The HPD response is separated into a response for fully absorbed photoelectrons and a separate response function for backscattered photoelectrons. A detailed description of these contributions can be found in reference [68].

The efficiency of the HPD silicon sensor and binary readout, measured in Fig. 5.6 is 86% and is typical of the production HPDs. This efficiency measurement has been carried out on a 10% sub-sample of HPDs at the test centres, with an average of 87±2%. The number is obtained from the ratio of hit pixels registered by the binary readout to the Poisson mean of the fit to the pulse height spectrum from the back surface. The variation between HPDs is correlated to the global threshold of the HPD's pixel chip. In the experimental setup the probability to lose photoelectron hits when two or more photoelectrons strike the same pixel is kept small by keeping the intensity low (on average there are less than two photoelectrons per trigger) and allowing the laser beam to diverge across the entire surface of the photocathode. These lost photoelectron hits are discussed in greater detail in Sec. 6.6.1.

5.3.1 Efficiency with Arrival Time

Owing to the finite rise-time ($\simeq 25\,\mathrm{ns}$) of the signal from the shaping stage of the binary readout chip, the time taken for the signal to exceed threshold depends on

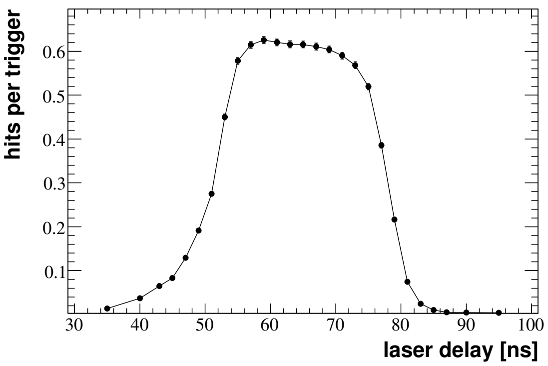

Figure 5.7: The relative efficiency as a function of the signal delay. The 25 ns width corresponds to the length of the strobe.

the size of the deposited signal in that pixel. If the amount of charge deposited in a pixel is reduced, through backscattering or charge sharing, then the pixel will take longer to pass threshold (time-walk). This is demonstrated in Fig. 5.7. The time delay between the laser pulse and the strobe being issued is varied by delaying the trigger to the laser diode. A signal is seen when there is an overlap between the strobe and the pixel passing threshold. This overlap should be 25 ns in length, corresponding to the length of the strobe. If the time taken to pass threshold were independent of the amount of charge deposited in the pixel then Fig. 5.7 would be an ideal top-hat function. The observed shape is a result of the time-walk. The highest efficiency is seen when the signal arrives early, allowing time for smaller signals to pass threshold within the 25 ns window of the strobe. Only prompt signals arriving later in the 25 ns window have time to pass threshold.

5.3.2 Efficiency with the Silicon Bias and HV

The time response of the HPD is strongly dependent on the threshold of the pixel readout. If the discriminator threshold is increased then the signal will take longer to pass threshold. This leads to a variation in the optimal timing between HPDs with different thresholds. This time response also depends on the reverse bias of the silicon sensor and on the HV supplied to the bleeder chain.

Decreasing the silicon bias increases the drift and charge collection time. A simplified estimate for this charge collection time can be made from the drift equation,

$$v(z) = \frac{dz}{dt} = \mu E(z)$$

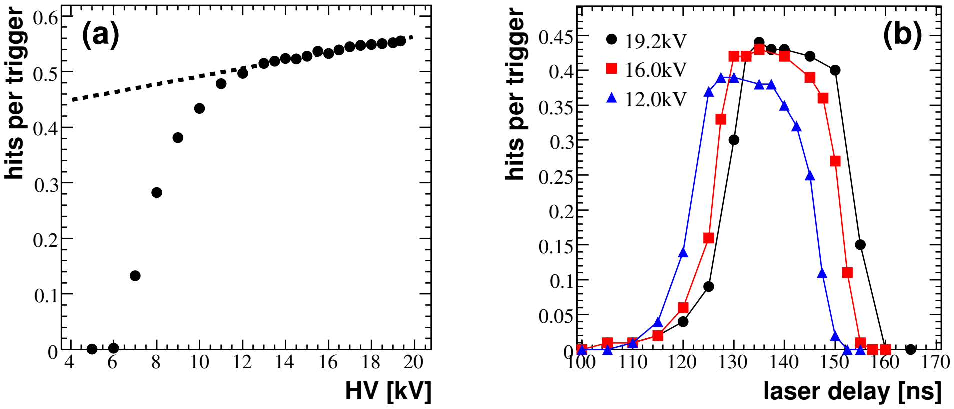

Figure 5.8: The variation in HPD efficiency *(a)* and time response *(b)*, in hit pixels per 25 ns trigger window, for three different supply voltages (12 kV, 16 kV and 19.2 kV).

where z is the depth at which the charge is deposited in the sensor, μ ($= 450\text{cm}^2\text{V}^{-1}\text{s}^{-1}$) is the carrier mobility and $E(z)$ the electric field at the p^+ on n junction. The HPD's silicon sensor is depleted at 12 V and has a thickness d of 300 μm. The charge is typically deposited in the first few microns of the n-type layer. The collection time in the silicon is [69],

$$t = \frac{d^2}{2\mu V_{\text{depletion}}} \ln\left(1 + \frac{2V_{\text{depletion}}}{V_{\text{bias}} - V_{\text{depletion}}}\right)$$

Using the equation above, if the silicon reverse bias is reduced from its nominal value of 80 V to 55 V the drift time will increase by 12 ns. If the bias is reduced further to 35 V then drift time increases by 34 ns, more than one bunch crossing at the LHC. These simple assumptions do not take into account the behaviour of the pixel readout. Fitting the three time response curves for the different voltages indicates the time taken to pass the discriminator threshold actually increases by 14.08 ± 0.03 ns and 56.73 ± 0.05 for 55 V and 35 V respectively.

When the HV supplied to the bleeder chain is reduced below its nominal 20 kV the efficiency of the HPD is also reduced (Fig. 5.8(a)). There is a sudden turn-on around 6 kV when photoelectrons from the photocathode gain enough energy to take the pixel above threshold. This depends on the pixel threshold, with one electron-hole pair being produced per 3.63 eV deposited in the silicon. The efficiency then rapidly increases as the HV is increased (the slope depends on the threshold dispersion between pixels). Above 12 kV the efficiency flattens and enters a "plateau" with a small gradient ($1.3 \pm 0.2\%\text{kV}^{-1}$). This gradient results from a reduction in

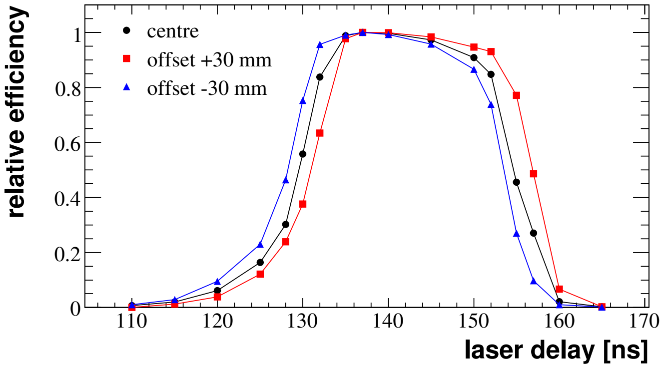

Figure 5.9: The relative efficiency as a function of the laser diode delay when the laser is focused on three different positions on the HPD's photocathode. The offset between the curves results from the time delay of the strobe as it propagates along the columns of the pixel sensor.

the number of backscattered photoelectrons that fail to exceed the threshold as the voltage is increased towards 20 kV. In Fig. 5.8(b) there is also a small change in the time response as the HV is reduced owing to a decrease in the amount of charge deposited by the photoelectrons.

5.3.3 Relative Efficiency Across the Pixel Chip

The readout signal or strobe, sent to the pixel chip propagates along the pixel chip in columns from the bottom of the pixel matrix. This introduces a propagation delay for the readout and clock signal and changes the optimal delay-time for reading out events from the pixel chip. This readout propagation time is non-negligible and was measured, as shown in Fig. 5.9, to be 4-5 ns across the full photocathode image.

5.4 HPD Noise Performance

The pixel HPD is a low-noise device, typically with rates below 10 kHz cm^{-2}. This value is a good guide for the HPD's performance as it equates to a probability of 1% per HPD of seeing a single hit pixel in the 25 ns read-out window. The global reconstruction algorithm will tolerate much higher noise rates than this and is stable up to a rate of 1% per pixel in the 25 ns bunch-crossing window, a factor 1000 above the noise rates discussed here. The noise performance, averaged over all of the production HPDs measured at the Scottish test centres is about 2 kHz cm^{-2}.

The noise rate is measured by taking a long run, over 5 million random triggers with the laser diode turned off. With no external illumination the main contributions to the noise of the HPD come from:

- Thermionic emission of photoelectrons from the photocathode. This is the most significant source of background and is primarily associated with HPDs with high quantum efficiencies in the red-to-near-IR where photoelectrons can be thermally excited with enough energy to overcome the work function of the photocathode.
- Ionisation of residual gas in the vacuum tube. This is discussed in detail in Sec. 5.5.
- Charge settling effects. This source of noise is an unfortunate consequence of having a grounded magnetic shield very close to the photocathode, with a 20 kV potential. This leads to sudden, but infrequent, discharges of charge at the photocathode that leave a large cluster of hits in the HPD. They are associated with clusters of typically 50 or more hit pixels on the silicon pixel sensor. This is a common source of background during the ramp up of the high-voltage supply to the HPD.
- Electronics noise. The rate of noise hits coming from electronics noise is very low and the majority of hits lying outside the photocathode image arise from genuine photoelectrons that are Rutherford back-scattered from the anode and then accelerated back onto it.

With the exception of electronics noise the background tends to come from genuine photoelectrons, that are produced at the photocathode and appear as hits on the pixel sensor that lie under the active photocathode area.

5.5 Vacuum Quality and Ion Feedback

The formation of afterpulses in photomultiplier tubes (PMTs) has been studied since the 1960's and is a well understood source of background in these devices. A detailed discussion of afterpulses in PMTs can be found references [70] and [71]. The same effect can also provide a source of background in the HPD.

Photoelectrons from the photocathode can strike residual gas atoms in the vacuum tube, ionising the gas. The ions will then drift in the opposite direction under the HPD's electrostatic field back towards the photocathode. The photoelectrons released by this ion bombardment will be seen as a large afterpulse that arrives some time after the prompt photoelectron signal.

The size of the afterpulse (in photoelectrons) can be estimated from the analogue back-pulse spectrum. The length and arrival of the gate (and the gain) are adjusted to include signals arriving up to 300 ns after the prompt signal. A Gaussian (with mean μ_{channel} and sigma σ_{channel}) are fitted to the spectrum to describe the afterpulse distribution and an exponential distribution (parametrised by α) to describe the tail of the prompt signal, Fig. 5.10.

$$N_1 \exp\left(\alpha \times \text{channel}\right) + N_2 \exp\left(-\frac{(\text{channel} - \mu_{\text{channel}})^2}{2\sigma_{\text{channel}^2}}\right)$$

A fit was also made to the pedestal and the prompt signal distributions to estimate the normalisation between photoelectrons and ADC channels. The distribution has a mean of 28.1 ± 2.9 and width of 5.87 ± 0.60 photoelectrons.

$$\mu_{\text{p.e.}} = \frac{\mu_{\text{channel}} - \text{pedestal}}{\text{peak separation}}$$

The time delay between the prompt signal and the large afterpulse is shown in Fig. 5.11, which was obtained by varying the time delay between the prompt signal and the readout window for the digital pixel chip. The rate of large clusters, with 5 or more hit pixels, is largest at a time delay of 200 ns after the original prompt signal.

The 200 ns delay in Fig. 5.11 is consistent with the (single) ionisation of Helium gas in the vacuum tube. This identification can be made by comparison of Fig. 5.11 and 5.12. Fig. 5.12 demonstrates the time taken for an ion produced at a particular depth in the HPD to drift back to the photocathode in the HPD simulation. This excludes Hydrogen and He^{2+} that both have faster transit times, arriving much closer to the prompt signal (He^{2+} also has a 200 times smaller ionisation cross-section). Helium can be particularly problematic for HPDs (and for PMTs) as it is known to diffuse through the quartz (fused silica) windows of these devices[4]. For this reason the HPDs are stored in a dry nitrogen atmosphere before being mounted and whilst inside the RICH 1 and 2 detectors.

---

[4] The rate of diffusion of Helium through fused silica (quartz) is $7.2 \times 10^{-14} \text{mol}\,\text{s}^{-1}$ per cm^2 of surface area, per mm of thickness, per mbar pressure difference at 25° C [72].

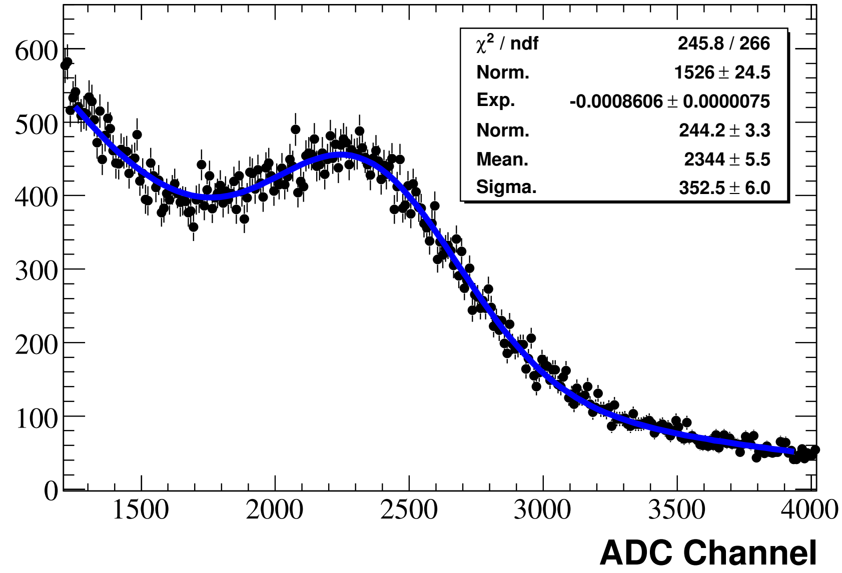

Figure 5.10: The tail of the analogue pulse height spectrum, read from the backplane of the silicon pixel sensor. The increased number of counts at higher ADC channels comes from large afterpulses that result from ion feedback in the vacuum tube. The fit to the data is described in the text.

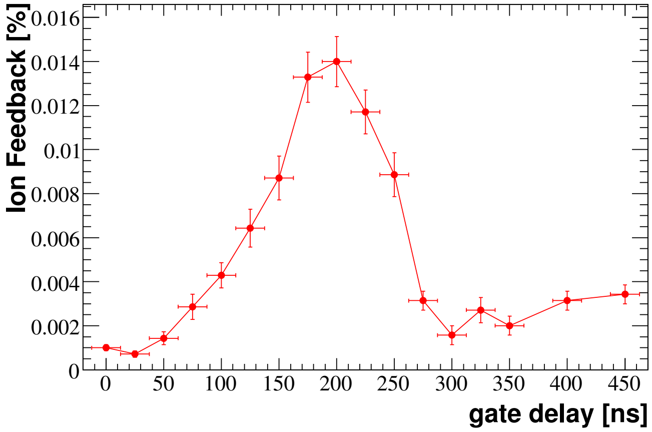

Figure 5.11: The rate (per trigger) of large clusters, expressed as the probability to observe a cluster of 5 or more ALICE pixels in a 50 ns readout window, as a function of the readout delay in ns.

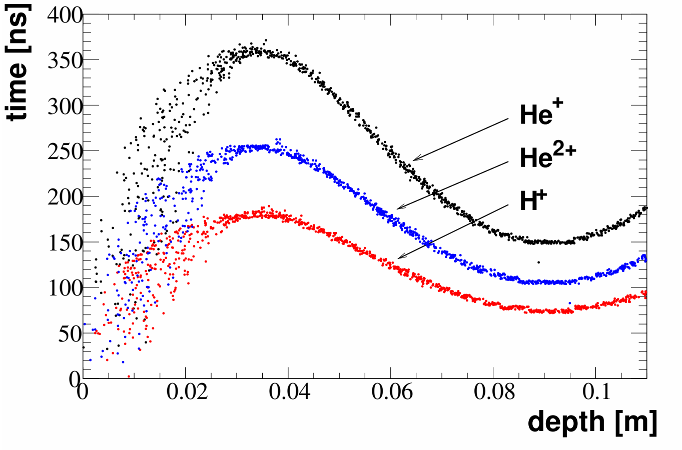

Figure 5.12: The time taken (results from simulation) for ions, produced at a particular depth in the HPD, to drift to the photocathode. Ions produced at a depth of around 3 cm in the tube are created in a region of low-field and take longer to drift to the photocathode. The three curves represent the transit times for Hydrogen and singly and doubly ionised Helium.

At the digital level the ion feedback events are seen as clusters of 5-20 ALICE pixels, whose position tends to follow the position of the original prompt signal. When the HPD is illuminated by a light source with a small spot size the majority of the large clusters lie around the position of the laser spot image on the pixel chip (see Fig. 5.2(c) where the laser diode is offset by 20 mm on the photocathode). A number of large clusters are also seen at the centre of the pixel chip. This is due to the cross-focusing of the HPD and the photoelectron density being largest at the crossing point. Ions produced at this point have a tendency to drift back along the tube axis to the photocathode. If the HPD is uniformly illuminated then the rate of large clusters is the highest at the centre of the tube.

5.6 Electron Optics and Spatial Precision

In Fig. 5.3, the trajectory of particles inside the HPD form an image on the silicon pixel sensor that follows almost linearly the position on the photocathode. The linearity breaks down at larger radii. This image at the anode is also not perfectly focused. The image point spread arises from photoelectrons, that are emitted from the same point on the photocathode, having a different initial energy or emission angle. The photoelectrons then follow different trajectories through the electrostatic field in the vacuum tube to the anode. Fig. 5.3 also demonstrates the image spread in photoelectron trajectories coming from the same position on the photocathode.

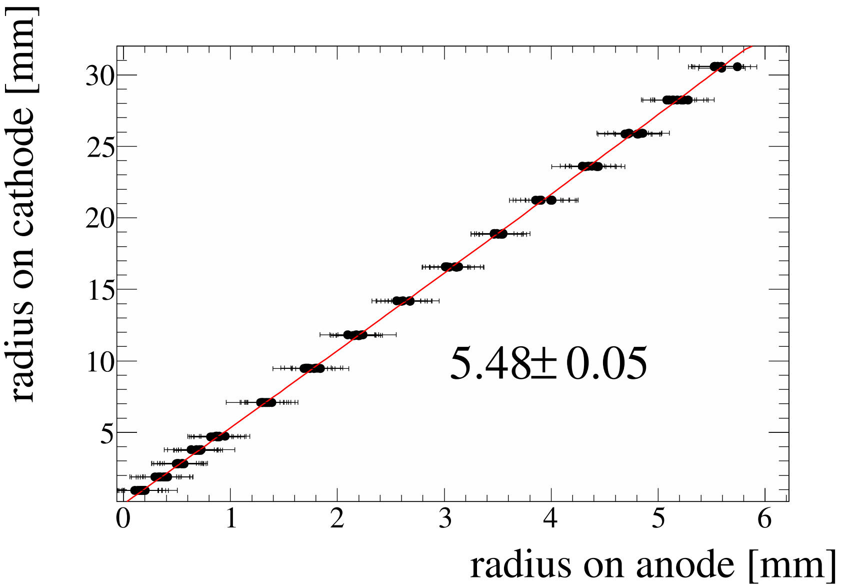

Figure 5.13: The demagnification of the image on the cathode seen at the anode. The image is cross-focused with an apparent linear demagnification by a factor of 5.5. A straight line fit is included.

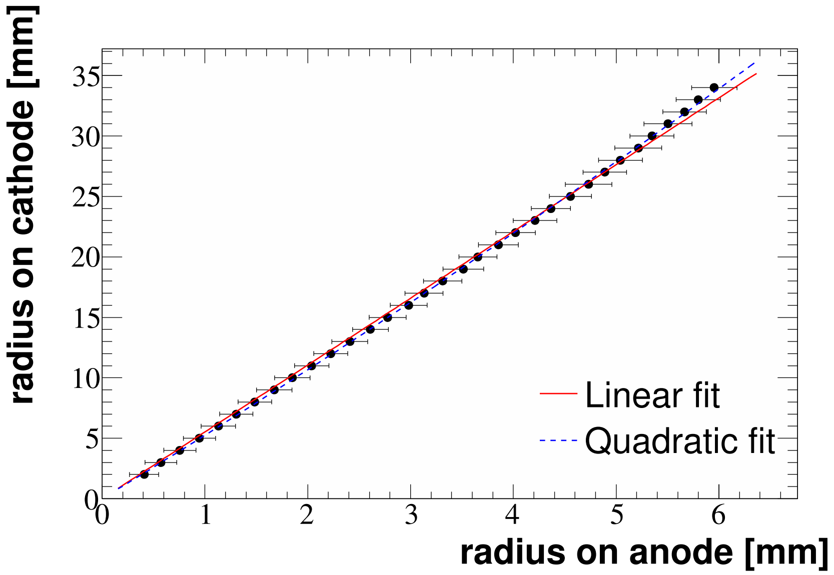

Figure 5.14: The demagnification of the image on the anode as calculated from the simulation of the HPD's electrostatic field. The fits are a linear fit with a demagnification 5.53 ± 0.05 and a quadratic ($r_{cathode} = p_0 + p_1 r_{anode} + p_2 r_{anode}^2$) fit with $p_1 = 5.17 \pm 0.20$ and $p_2 = 0.080 \pm 0.043 \text{mm}^{-1}$.

5.6.1 Demagnification

The demagnification of the image in the cross-focusing optics has also been measured in the laboratory setup. The translation stage is used to scan the optic fibre across the surface of the quartz window, and the impact position on the photocathode calculated by performing a correction for refraction in the quartz. This is then compared to the reconstructed position on the silicon sensor, formed by taking the centre of gravity of the image, over 10,000 triggers. To take into account any misalignment of the pixel sensor a LED is used to illuminate the entire photocathode surface and the boundary of the image fitted to a circle to get the image size and, significantly, the '$x - y$' position of the HPD axis on the silicon pixel sensor.

The result for one of the HPDs is shown in Fig. 5.13. A straight line fit to the data results in an image size that is demagnified by a factor of 5.48 ± 0.05 on the silicon sensor. This is consistent with the value, of 5.53 ± 0.05, that comes from the simulation (Fig. 5.14). The error bars on Fig. 5.13 come from the image point spread of $\sim 160\,\mu$m. Four measurements were taken at each radial position on the photocathode. These correspond to the four x or y positions on the translation stage that have an equivalent offset on the photocathode. These are in good agreement. The demagnification of the HPD was found to be unaffected by the proximity of Mumetal or Supra-36 local magnetic shielding.

5.6.2 Image Point Spread

The image point spread has been estimated from the full simulation of the field in the HPD and is $200\,\mu$m in the near-UV and $80\,\mu$m in the Red. The simulated point spread at a number of different photon energies is plotted in Fig. 5.15(b). For reference the wavelength of the blue DC LED and the red laser diode are indicated. The larger point spread in the blue comes down to the increase in the average emission energy from the photocathode. The point spread is calculated, in the simulation, by finding the centre of gravity of the hit position of 1000 photoelectrons on the anode, emitted with a random energy and angle. The radial density distribution about this point is fitted according to,

$$\rho(r) \propto r \times \exp\left(-\frac{r^2}{2\sigma_{PSF}^2}\right)$$

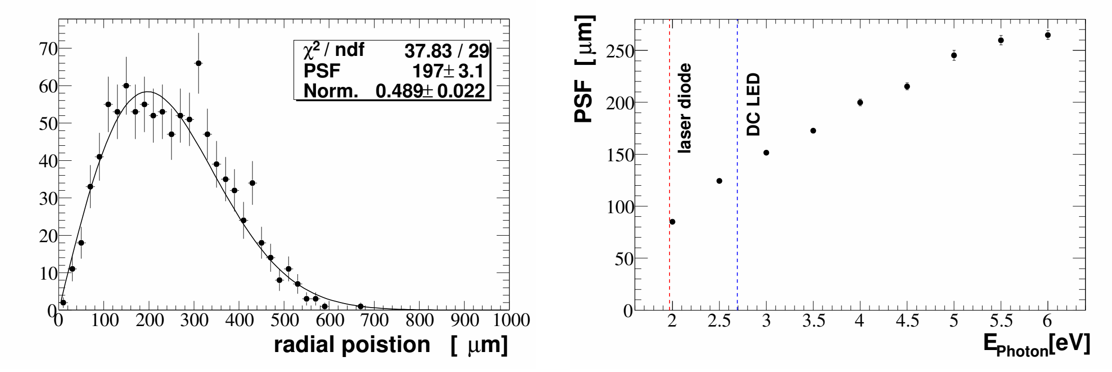

(a) (b)

Figure 5.15: The radial image point spread (PSF) on the pixel sensor in a simulation of 1000 photoelectrons emitted at a radius of 20 mm on the photocathode with an incident photon energy of 4 eV (*a*). The right-hand plot, figure (*b*), demonstrates the dependency of the fitted PSF on the incident photon energy. For reference the wavelength of the blue DC LED and red fast pulsed laser have been indicated.

where σ_{PSF} is the measured point spread. This is equivalent to the Gaussian spread in row and column directions on the pixel sensor. An example fit is provided in Fig. 5.15(a).

Experimentally the image point spread can be calculated in a similar way; by calculating the centre of gravity of hit pixels on the anode. In this case the point spread needs to be deconvolved from the effect of the pixel size and the finite spot size of the laser.

$$\sigma^2_{\mathrm{PSF}} = \sigma^2_{\mathrm{Measured}} - \sigma^2_{\mathrm{Laser}} - \sigma^2_{Pixel}$$

The spot size of the red laser diode was measured using a CCD camera with a 11.6 μm pixel size to be 268 μm on the photocathode. Applying the image demagnification law from Fig. 5.13 the spot size is expected to be 49 μm on the pixel sensor. The large pixel size of the LHC*b* pixels introduces a large smearing effect on the measured resolution. A better estimate of the point spread can be made by looking at the short pixel direction of the ALICE pixels. In ALICE mode the contribution due to the pixelisation of the pixel sensor is $\sigma_{Pixel} \simeq 18\,\mu$m. Fitting a Gaussian to the distribution of hit pixels in the small pixel direction, the HPD point spread at 2 eV (628 nm) is $\sigma \simeq 58\,\mu$m.

The image point spread depends on the position on the photocathode, and at larger radii the point spread increases almost quadratically. The increased point spread is combined with a break down of the linear demagnification law. In Fig. 5.16(b)

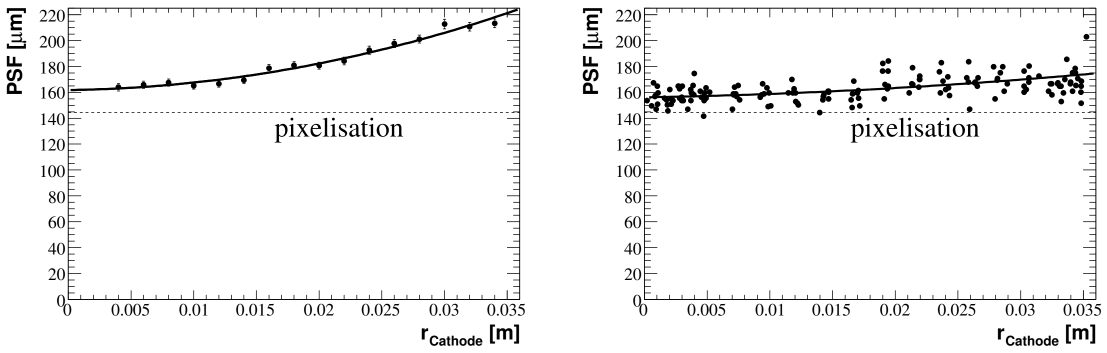

(a) (b)

Figure 5.16: Variation of the image point spread with position on the photocathode (or anode) in the simulation (*a*) and measured (*b*) for the blue LED. At this wavelength the image spread introduces an equivalent error to the pixelisation.

this behaviour is illustrated for laboratory measurements with the blue DC LED (2.7 eV) and in Fig. 5.16(a) in the simulation with $E_{photon} = 4\,\text{eV}$. The measured point spread at 2.7 eV (460 nm) is 140 μm at its smallest value. A quadratic fit yields a value of 156 μm on the tube axis. This point spread is comparable to the size of the error coming from the pixelisation of the LHC*b* pixels ($\simeq 143\,\mu$m).

5.7 Charge Sharing

The majority of the $5000e^-$ of charge is deposited in a thin layer near the surface of the pixel sensor. Diffusion of this charge near the pixel boundary can lead to pixel-to-pixel charge sharing. The charge is shared between two or more neighbouring p^+ pads. The Gaussian spread σ, due to diffusion over the charge collection time t, comes from Einstein's equation.

$$\sigma = (2Dt)^{1/2}$$

$$D = \frac{kT\mu}{e}$$

where k is Boltzmann's constant, T is the temperature and μ the carrier mobility. Using the numbers from Sec. 5.3.2 the typical diffusion scale is $\sigma = 6.8\,\mu$m. In ALICE mode the amount of charge sharing is very different in the row and column directions due to the asymmetric size of the pixels. It is approximately eight times larger along the columns than in the rows. The effect of this charge spread is a 2-3% probability of gaining an extra pixel hit as the charge is shared between neighbouring pixels. This is considered in more detail in Sec. 6.6.1.

5.8 HPD Performance in an External Magnetic Field

The electrostatic cross-focusing of the HPD can be affected by an external magnetic field. Magnetic effects will lead to image distortions, reducing the resolution of the HPD and may result in photoelectrons being deflected away from the anode. These distortions can be significant in the RICH detectors, which sit in the fringe field of the dipole magnet. The maximum field in the region of the HPD plane of RICH 2 is 6 gauss and in RICH 1 25 gauss (2.5 mT compared with a peak field in the dipole magnet of 1.1 T). These values are without the local magnetic shielding of the HPDs. This section reports on measurements made on these image distortions with and without the HPD's local magnetic shielding. The measurements are a continuation of the earlier studies in reference [73].

Photo-electron trajectories within the HPD are governed by the Lorentz force,

$$\vec{F} = -e\left(\vec{E} + \vec{v} \times \vec{B}\right)$$

where $\vec{E}$ is the electric field from the HPD electron-optics, $\vec{B}$ is the external magnetic field and $\vec{v}$ the photoelectron velocity. When the external field is parallel to the tube axis the field exerts a force on the photoelectrons; $-er\dot{\phi}B_{axial}$ in the $\hat{r}$-direction and $e\dot{r}B_{axial}$ in the $\hat{\phi}$-direction. This is illustrated in Fig. 5.17. It leads to an increase in the image size and a rotation of points on the image about the tube axis. The axial rotation of the image will depend only on the photocathode radial coordinate, r, and leads to a new image coordinate r', on the anode that is a deviation from the standard demagnification law,

$$\begin{aligned} \Delta\phi &= a_0\left(B_{axial}\right) + a_1\left(B_{axial}\right) r + a_2\left(B_{axial}\right) r^2 \\ r' &= b_1\left(B_{axial}\right) r + b_2\left(B_{axial}\right) r^2 \quad . \end{aligned}$$

In a transverse field, a magnetic field perpendicular to the axis of the HPD, the image at the anode undergoes a lateral shift. The size of this shift is also a function

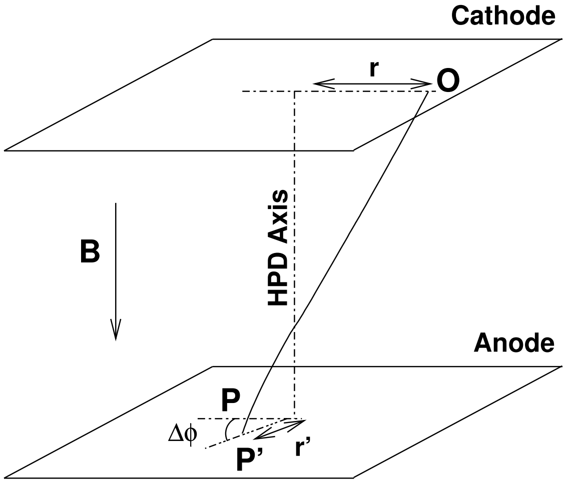

Figure 5.17: A schematic showing the origin of image distortions in the HPD. Photoelectrons emitted from the cathode (point O) are accelerated by the large electric field of the HPD to the anode. In the absence of an external magnetic field these photoelectrons would strike the anode at point P. In the presence of an axial magnetic field, B, the photoelectrons feel a Lorentz force normal to the axis. This leads to a rotation of the image by $\Delta\phi$ to point P' and an expansion of the image on the anode.

of the HPD radial coordinate r, a consequence of the electrostatic field in the HPD. In general the translation of the image is small and transverse fields are unlikely to be problematic in LHCb as they are almost entirely screened by the local magnetic shielding of the HPDs. With the shield in place the transverse field inside the HPD is consistent with zero, within the tolerance of the Hall probe (± 0.5 gauss).

The experimental setup used for these measurements is essentially the same as the setup described in Sec. 5.1. However the red laser diode was replaced by the blue LED and a Helmholtz coil was placed around the HPD. The orientation of the Helmholtz coil was adjusted to provide a field; axial, transverse or at some oblique angle to the axis of the HPD. The '$x - y$' translation stage was used to scan the optical fibre over the surface of the HPD and map the distortions caused by the external field. Practically this was done by projecting a series of 161 points to form an image of an eight-armed cross onto the surface of the quartz window.

5.8.1 Image Distortions in an Unshielded HPD

The field from the Helmholtz coil is relatively uniform over the volume of the HPD, but does fall away slowly from the axis of the HPD (at the centre of the coil). When the field is applied the image on the anode is distorted as described above. For example in an axial field of 15 gauss the image of the eight-armed cross is rotated

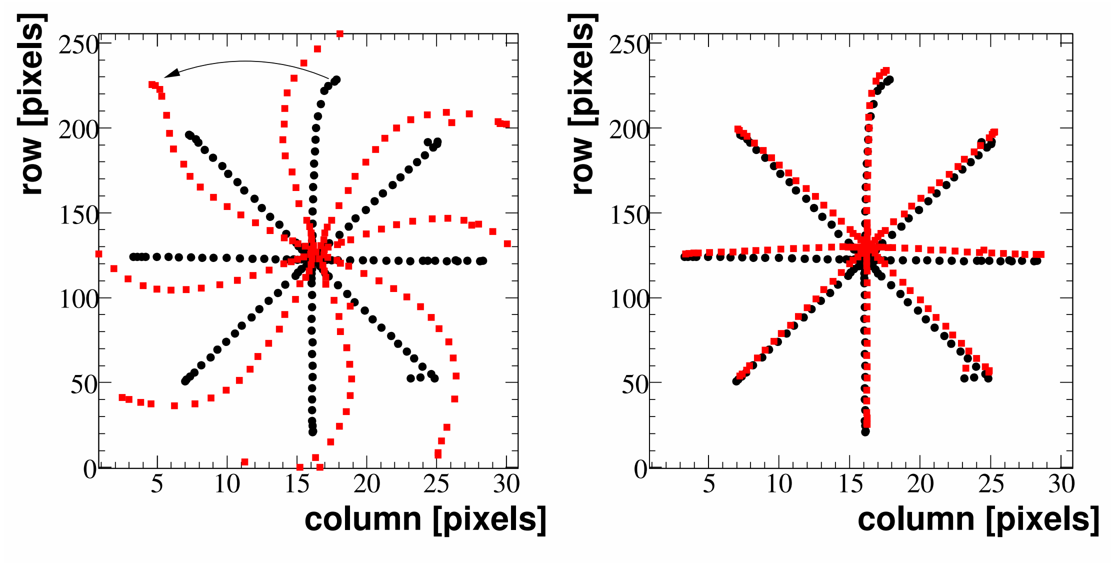

(a) (b)

Figure 5.18: Image distortions in an unshielded HPD under a 15 gauss axial field (*a*) and a 20 gauss transverse field (*b*).

and expanded as in Fig. 5.18(a). If the magnetic field is increased then the image of the eight-armed cross is no longer fully contained on the pixel sensor. The radial expansion and rotation of the image seen by the the pixel sensor for three external field strengths are shown in Fig. 5.19.

In Fig. 5.19(a) a straight line has been fitted to the radial distortion. There is a clear trend showing that the radial position of the hits is increased proportionally to the radius on the photocathode and that this increases with increasing external field. The image undergoes a rotation about the axis that depends on the field

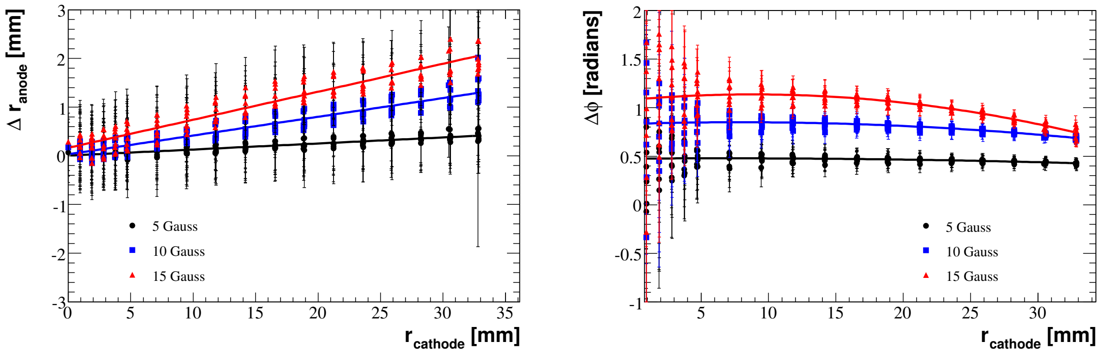

(a) (b)

Figure 5.19: Radial (*a*) and azimuthal (*b*) distortions for an unshielded HPD in 5 gauss, 10 gauss and 15 gauss axial fields.

B_{axial}	a_0	$a_1[\mathrm{mm}^{-1}]$	$a_2[\mathrm{mm}^{-2}]$	b_1
5 G	0.472 ± 0.060	0.001 ± 0.005	$-(8.3 \pm 10.5) \times 10^{-5}$	0.013 ± 0.002
10 G	0.840 ± 0.056	0.003 ± 0.005	$-(24.2 \pm 9.8) \times 10^{-5}$	0.0400.002
15 G	0.112 ± 0.055	0.009 ± 0.005	$-(58.9 \pm 10.4) \times 10^{-5}$	0.063 ± 0.002
20 G shielded	0.469 ± 0.061	-0.006 ± 0.005	$-(4.2 \pm 10.8) \times 10^{-5}$	0.005 ± 0.002
30 G shielded	0.654 ± 0.060	-0.006 ± 0.005	$-(9.5 \pm 10.6) \times 10^{-5}$	0.008 ± 0.002

Table 5.1: The parametrised image distortions, $\Delta\phi = a_0\,(B_{axial}) + a_1\,(B_{axial})\,r + a_2\,(B_{axial})\,r^2$ and $r' = b_1\,(B_{axial})\,r$, for r in mm.

and falls away (due to a small decrease in the field of the Helmholtz coil) at higher radii. The wild variation in the image rotation $\Delta\phi$, close to the HPD axis (see Fig. 5.19(b)) arises from the ambiguity as the radius tends to zero. The image rotation has been fitted with a second order polynomial. The results of the fit are provided for reference in Table. 5.1.

The image distortion caused by a transverse field is shown in Fig. 5.18(b). There is a small shift of the image position perpendicular to the direction of the field.

5.8.2 Image Distortions in a Shielded HPD

The HPDs in RICH 1 and RICH 2 are surrounded by 14 mm long local magnetic shielding. This is Mumetal shielding for RICH 2 and Supra-36[5] for RICH 1. These are Nickel-Iron magnetic alloys, with high permeability and saturation field strength. Supra-36 is chosen for RICH 1 because of its increased saturation field strength over Mumetal ($B_S = 1.3\,\mathrm{T}$ c.f. $B_S = 0.76\,\mathrm{T}$) and the higher permeability to large fields ($H > 1000\mathrm{Am}^{-1}$).

With the magnetic shielding in place an external axial field of 30 gauss is reduced to 3-6 gauss within the HPD. The image distortion seen on the pixel sensor is shown in Fig. 5.20. A transverse field is almost completely screened (it is consistent with zero within the errors on the Hall probe measurement).

The radial and azimuthal distortions in a shielded HPD with an external field of 30 gauss are consistent with the distortions seen in an unshielded HPD at 5 gauss. This can be seen by comparing Fig. 5.21 and Fig. 5.19.

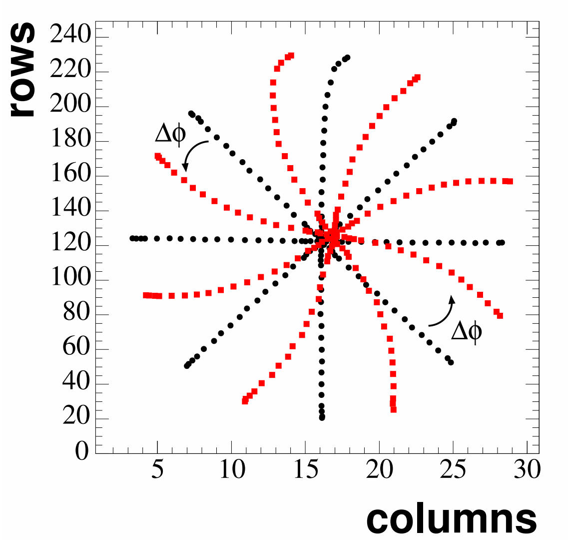

Figure 5.20: Image distortions in a shielded HPD with a 30 gauss axial magnetic field.

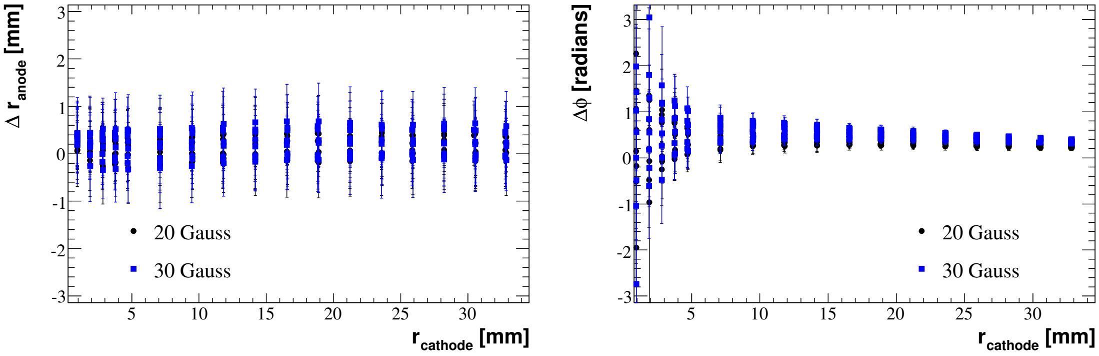

Figure 5.21: Radial and azimuthal distortions for a shielded HPD in a 20 gauss and 30 gauss field.

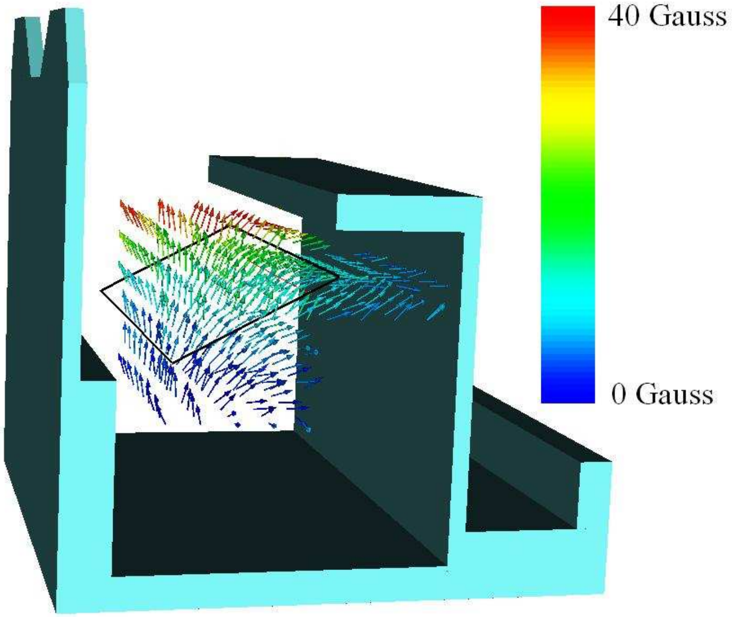

Figure 5.22: The $\vec{B}$ field in the RICH 1 detector. The position of the HPD plane is indicated by the rectangular outline.

5.8.3 Image Distortions in the RICH Detectors

The measured field around the HPD plane in the RICH1 1 detector is at most 30 gauss (Fig. 5.22), but has an axial component that is ∼20 gauss. This is large enough to lead to significant distortions of the HPD image even in a shielded HPD. In the RICH detectors the distortions will be measured in-situ, with and without magnetic field, by mapping points on the HPD photocathode to hit pixels on the HPD anode. This is achieved in RICH 1 using a series of LEDs mounted on a translation stage. In RICH 2 where the distortions are expected to be much lower, a simple projector system will be used. Measurements with the Hall probe, when the HPD plane of RICH 1 is populated with Mumetal shields, confirm the axial field inside the HPD is likely to be 4-6 gauss at the centre of the HPD plane.

5.9 Summary

This chapter gives a flavour of measurements made at CERN on the early production HPDs. Many of these measurements have since been repeated on the production HPDs at the test centres in Scotland. The programme at the test centres includes;

---

[5] Supra-36 is 36% Nickel and Mumetal 80%.

measurements of the HPD noise performance, the pixel chip threshold, leakage current and a measurement of any dead or noisy pixels (that is used to mask the pixels in the final RICH detectors). The test centres have also made measurements of the HPD readout efficiency and the HPD quantum efficiency on a small, 10%, subsample of HPDs. Finally they have, using a projected pattern, looked for rotations or translations in the mounting of the HPD pixel sensors [74].

At the time of data taking, the measurements and simulation of the image point spread in Sec. 5.6.2 were quite surprising. In earlier simulations this point spread was negligible, but the results showed that the contribution to the Cherenkov angle resolution was comparable to the pixelisation on the pixel sensor. This change had been brought about by a modification of the high voltage supply chain. The values of the resistors in the bleeder chain had been changed slightly to reduce the image size from the photo-cathode on the pixel sensor. This decision was made following the early magnetic field measurements that showed the photoelectron could be swept off the pixel sensor by the external field. The revised image point spread has now been added to the detector simulation and has explained a previously unresolved issue with the Cherenkov angle resolution in beam test data taken in 2004. There is now good agreement between the measured and simulated Cherenkov angle [75].

The measurements in Sec. 5.8 have since been used to inform the choice of both the RICH 1 HPD pitch and local magnetic shielding. Supra-36 shields have been used in RICH 1 to avoid saturation of the magnetic field inside the shield and to maintain the same pitch as RICH 2 (89 mm).

Chapter 6 presents an analysis of the performance of 48 HPDs over three beam test with a prototype RICH detector. One of the two stated aims of these beam tests was to measure the efficiency of the HPD and the readout chain in a realistic environment and with the final RICH electronics. The efficiency in the following chapter should be compared with the 87% efficiency described in Sec. 5.3.

Chapter 6

Qualification of the HPDs in a Charged Particle Beam

In 2006 a prototype of the LHC*b* RICH detectors was tested in three beam tests. Two of these were carried out in a 493 MeV/c electron beam at INFN Frascati's beam test facility (BTF) and the third in a 80 GeV/c π^- beam at the CERN SPS. The principal aim of these tests was to measure the detected Cherenkov photon yield and Cherenkov angle precision using a HPD array in a setup that closely resembles the final LHC*b* setup. This chapter describes the analysis of the photon yield from data collected at the BTF and SPS. Although the BTF runs came chronologically earlier than the runs at the SPS the analysis is complicated by an asynchronous beam and data acquisition. For this reason the runs at the SPS, with an LHC-like 25 ns beam structure, are considered first. Data from the BTF are compared for consistency.

6.1 The Prototype RICH Detector

The prototype Cherenkov detector is shown in Fig. 6.1. It is a light-tight gas vessel that contained either N_2 or C_4F_{10} gas radiator. Particles entering the gas volume, through a thin aluminium foil, produce Cherenkov light that is focused into a ring image by a parabolic mirror (focal length 1016 mm) onto the photon detector plane. The length of radiator seen by the charged particles is 1102 mm. The HPDs are contained in a N_2 gas volume that is separated from the radiator gas volume by a 5 mm-thick quartz window. The N_2 volume holds three complete RICH 2 columns of 16 HPDs. The parabolic mirror is mounted on a set of micrometric screws that allow the angle of the mirror to be adjusted and the Cherenkov ring to be directed and focused onto different HPDs.

Nitrogen gas (N_2) is used as a Cherenkov radiator because it has the useful property that Cherenkov rings produced in it can be fully contained within a single HPD in the HPD plane.

For each beam test the production front end electronics and detector control system were used but the trigger and some of the other readout electronics differed. These are described below.

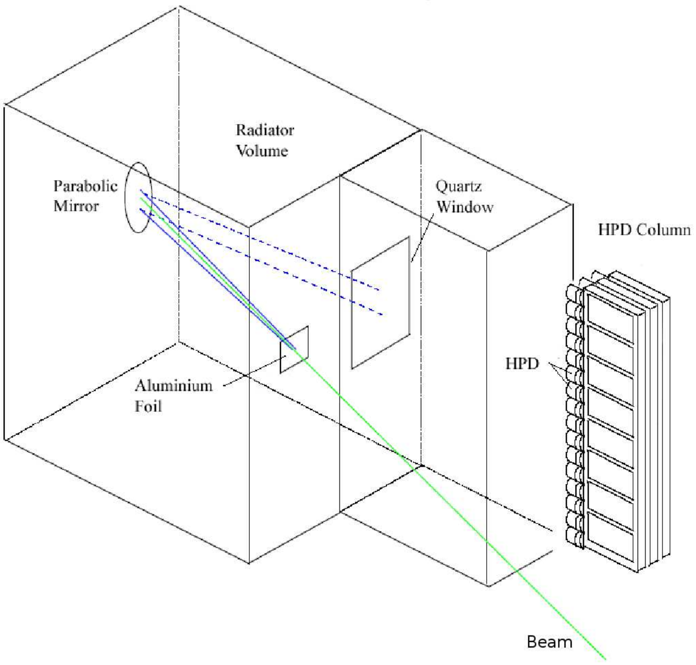

Figure 6.1: The prototype RICH detector used in the beam tests. Particles entering the radiator volume produce Cherenkov light that is focused by a parabolic mirror onto three full columns of HPDs.

6.1.1 CERN SPS Beam

The beam test at the CERN SPS provided the first chance to test the prototype detector with the final readout electronics, including the Level-1 board, ODIN [76], event builder and monitoring farm in a beam with a LHC-like 25 ns time structure (Fig. 6.2). This beam was produced using protons from the CERN SPS incident on a target, producing an 80 GeV/c secondary beam of negatively charged particles.

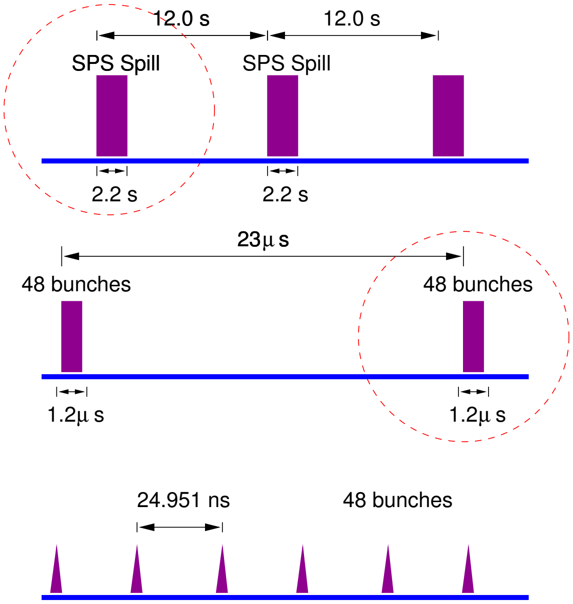

Figure 6.2: The time structure of the SPS beam provided to the North Area. This is LHC-like with a bunch spacing in each bunch train of 25 ns.

These are mainly π^- with an estimated contamination of 10% electrons, 7% kaons and 3% antiprotons [77], all exceeding the Cherenkov threshold in N_2.

An overview of the electronics used in the beam tests is given in Fig. 6.3. The clock was provided by the TTCmi interface to the SPS and is distributed to the electronics through the ODIN [76], an electronics board responsible for supervising the readout in LHC*b*. The clock is then converted from an electrical signal to an optical signal and broadcast to the Level-0 and Level-1 boards. Details of the timing and fast control (TFC) system can be found in references [78] and [57]. The Level-0 board then distributes the clock electrically to the pixel chip.

The trigger is provided by a pair of 2 cm × 2 cm plastic scintillators upstream of the prototype RICH detector. A pair of bare HPD pixel-chip sensors was used as an improvised silicon tracker, mounted on tripods upstream and downstream of the detector. The tracking stations were included to provide tracks for off-line Cherenkov angle resolution studies.

The ODIN forwards the trigger through the TFC system to the Level-1 and the front-end. On receipt of a trigger (the strobe) data is read out from the HPD, formatted by the Level-0 board and transmitted off-detector over 1.6 GHz optical links. The links are bundled into 12-fibre data ribbons. Data is received by the Level-1 board, which performs zero-suppression and multiplexes data from the Level-0 boards out via Gigabit ethernet to an event-builder farm. This computer farm then

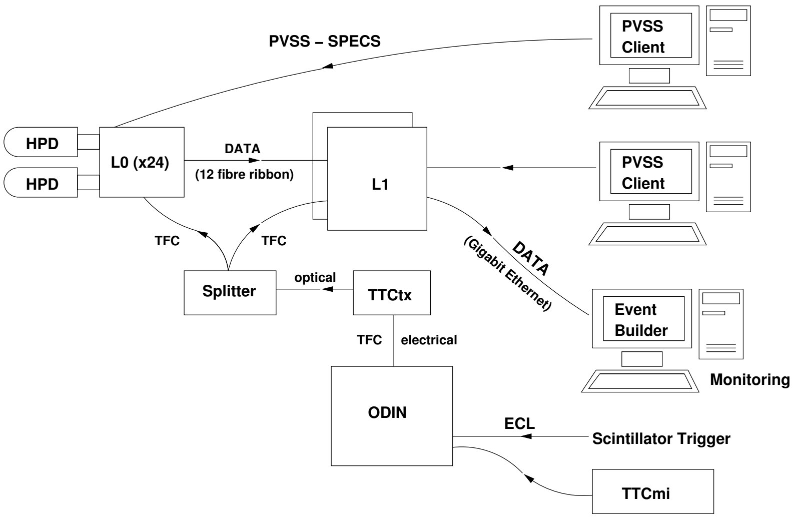

Figure 6.3: An overview of the electronics used in the beam test at the CERN SPS.

combines all the data from a single event (using time stamp information), performs some data quality monitoring and writes the data to disk. The electronics boards (the Level-0 and Level-1) were controlled though a pair of PCs using PVSS[1] [78] via a SPECS [58] interface. The bare anodes that constitute the tracker appear to the rest of the readout system as another pair of HPDs.

6.1.2 Beam Test Facility at INFN Frascati (BTF)

The Frascati beam tests used a 493 MeV/c electron beam that arrived asynchronously with respect to the 40 MHz clock that is applied externally to the front-end electronics. Particles arrive randomly within the HPD readout window. Events are read out if a beam trigger (that identifies when a beam pulse is arriving in the hall) is received along with a signal from a sodium iodide calorimeter placed behind the mirror. The analogue pulse height from the calorimeter is passed through a low and high level threshold discriminator so that only events with a single electron are selected (with a purity $> 99\%$).

For this asynchronous beam test the final UK Level-1 board, ODIN and the event builder were not available and the Level-1 board was replaced by a 12 channel prototype, while the ODIN and event builder were replaced by electronics specially assembled for this test.

---

[1] PVSS is a commercial piece of software produced by ETM professional control, Austria.

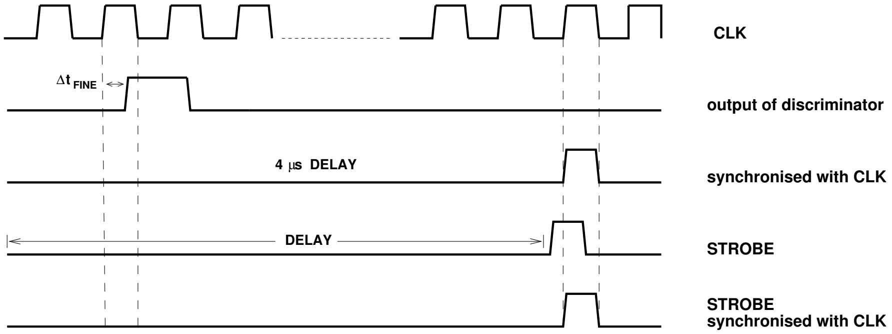

Figure 6.4: Time structure of the HPD pixel readout. The output of the discriminator of the pixel sensor is synchronised to the external clock and enters a delay line ($4\,\mu$s). It is read into the pixel FIFOs on receipt of an external trigger, that is also synchronised with the clock. If the trigger is applied for more than one clock cycle then a hit in either of the two (three or more) clock cycles will be read out as a hit in the pixel FIFOs.

6.2 Timing

6.2.1 Timing in a Synchronous Beam

The time response of a single HPD in the laboratory setup was discussed in Sec. 5.3. In those measurements the arrival time of the laser pulse with respect to the clock window, which arrives synchronously, was adjusted and the highest efficiency observed when the signal passed threshold early with respect to the 25 ns window.

To better understand this behaviour it is useful to describe in more detail the pixel chip readout. This is done with reference to Fig. 6.4. The analogue output from the shaping stages is fed into a discriminator that produces an output if the pixel is above threshold. This output is then synchronised with the clock and enters a delay line that stores the 'hit' for the trigger latency ($4\,\mu$s for the L0 trigger). The trigger, the STROBE, is resynchronised with the clock at the front-end and instructs the data in that clock window to be written to the pixel FIFOs. The data is then shifted out in columns by the shift registers. The time-walk discussed in Sec. 5.3 is due to the discriminator response, with smaller signals taking longer to exceed threshold. Depending on the relative arrival time within the clock window it is possible, due to time-walk, to have the larger prompt signals and the smaller (e.g. through charge sharing or backscattering) signals synchronised with different clock transitions.

At the SPS the beam arrives at fixed 25 ns time intervals with a fixed phase compared with the clock. This relative phase can be adjusted by shifting (delaying by Δt_{FINE} in Fig. 6.4) the clock in time using the timing fine delay features of the Level-0 boards (on TTCrx receiver).

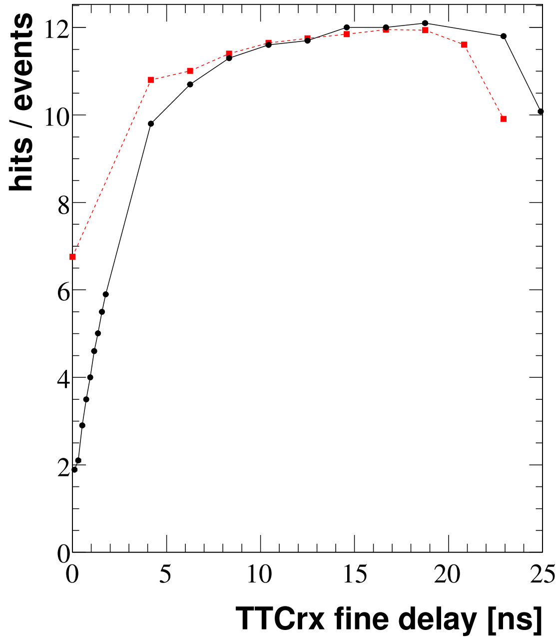

Figure 6.5: Variation of the HPD efficiency with the TTCrx fine delay for two HPDs at the SPS beam test.

An example timing scan, achieved by varying the clock phase, can be seen in Fig. 6.5. There is a relative time shift of 2 ns between the curves for the two HPDs shown in the figure. This is typical of the HPDs in the test beam and results from a difference in the HPD threshold ($921e^-$ c.f. $1253e^-$). The fine delay features enable the timing of each pair of HPDs to be adjusted individually.

6.2.2 Timing in an Asynchronous Beam

At the BTF the e^- beam was asynchronous with respect to the 40 MHz clock of the HPD readout, i.e. each event will arrive with a random phase in the clock window. The readout signal, the strobe, is generated by the combination (logical AND) of: an the calorimeter signal, passed through a discriminator, and a machine trigger with a veto from the DAQ software.

The arrival time of the strobe at the front-end is tied to the arrival time of the signal with an additional delay that is introduced by delaying the machine trigger. This delay is used to delay the readout for the Level-0 trigger latency and

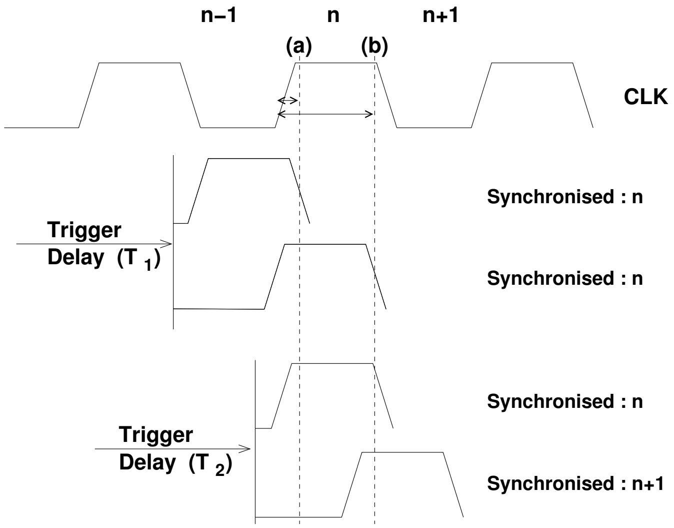

Figure 6.6: Time structure of the pixel readout in an asynchronous beam.

to compensate for any time of flight delays in the cables. In Fig. 6.7 the data points show the HPD efficiency as a function of this trigger delay for one of the HPDs at the BTF. The triangular shape is described below.

If we imagine there are two events; one passing threshold early (a) in a particular clock window and one late (b) and there are also two different delay settings T_1 and T_2. With the first trigger delay the readout signal for event a will arrive at the front end at a time $T_1 + t_a$, where t_a is the arrival time of event. For the remainder of the discussion t_a can be thought of as the relative arrival time within the 25 ns clock window. In Fig. 6.6, with delay setting T_1 the strobe for both a and b is synchronised to the correct clock cycle and the correct event is read out from the delay unit. For T_2, the event arriving later (b) is synchronised to the wrong clock cycle. In this case an empty event is read out from the delay units.

As the trigger delay is increased the fraction of events where the strobe is synchronised with the correct, the previous or the next clock cycle varies, leading to the triangular shape in 6.7. If the HPD response were ideal the efficiency would be a convolution of two 25 ns top hats. In reality the time response is an integral of a 25 ns window of the HPD time response $\varepsilon(t)$. The fitted line in Fig. 6.7 compares the data from the testbeam with this model for the time response, using $\varepsilon(t)$ measured in laboratory tests for this HPD.

For the photon yield studies the timing is adjusted to sit at the point where the photon-yield is greatest.

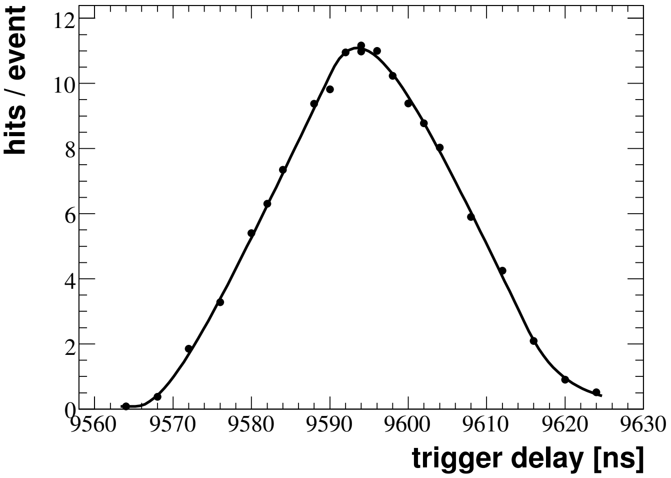

Figure 6.7: An example of the variation of the HPD efficiency (for HPD 8_133) with the trigger and clock delay at the BTF. The fit model is described in the text.

6.3 Performance of the HPDs in the Full System

The noise performance in the beam tests is significantly worse than measured in laboratory tests. There are a number of possible reasons for this: the HPDs at the test centres were not tested with their local magnetic shielding, there is an increase in temperature and stray background light from the readout system with the close packed HPD arrays. All of these will lead to an increase in the dark count rate (DCR), particularly for HPDs with a high red sensitivity

This red sensitivity is shown for all of the HPDs (at the BTF and SPS) in Fig. 6.8. There is some correlation between the two features. The HPD with the highest DCR, HPD 9_106, is associated with a large number of hit pixels in the very centre of the HPD. This could be an indication of poor vacuum quality and consequently a high ion-feedback rate. It should be stressed that even the worst performing HPD is still well below the $10\,\mathrm{MHz\,cm^{-2}}$ level at which the ring reconstruction algorithm in LHCb breaks down. This noise level is insignificant for HPDs used for the photon yield measurements.

6.4 Expected Photon Yield

The number of observed photoelectrons for a real RICH detector; with a mirror of finite reflectivity, $R(E)$, quartz with transmission, $T(E)$, and a photon detector with a quantum efficiency, $Q(E)$ where E is the photon energy is given by

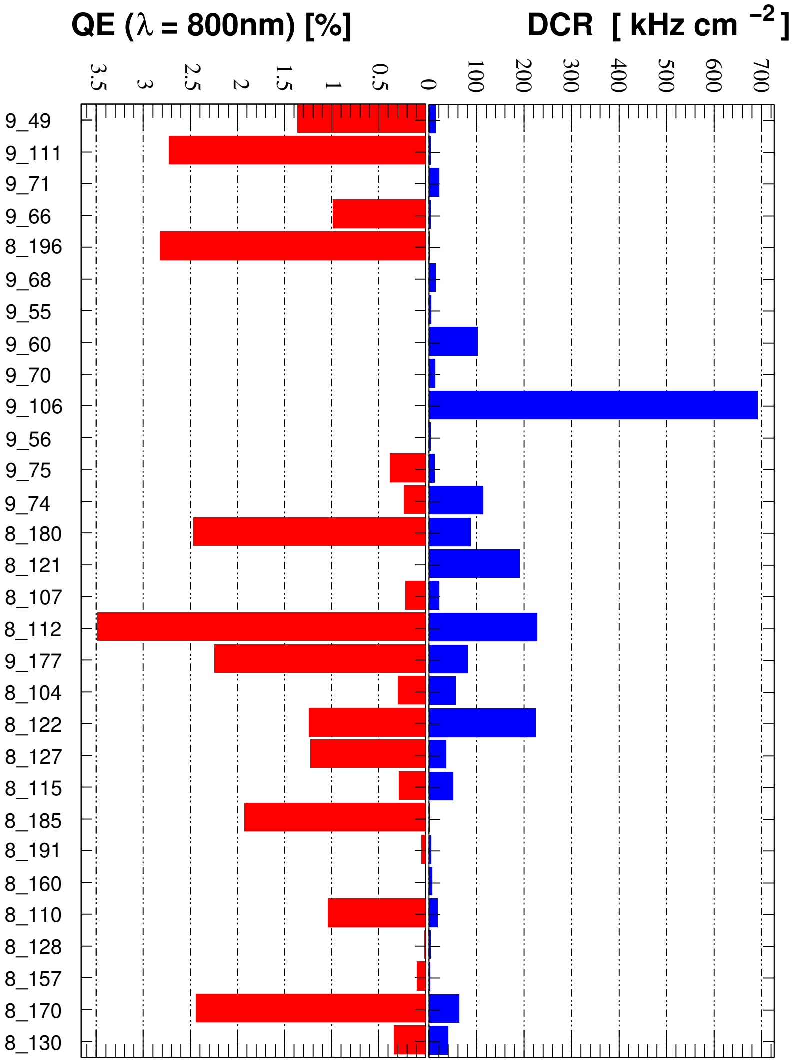

Figure 6.8: The noise performance (DCR) of 30 HPDs used in the testbeam at the CERN SPS. For comparison the HPD quantum efficiency in the red (at 800 nm) is also displayed. (DCR).

	N_2	C_4F_{10}	CF_4
S_0	$5.32 \times 10^{-8}\,\mathrm{nm}^{-2}$	$2.53 \times 10^{-7}\,\mathrm{nm}^{-2}$	$1.25 \times 10^{-7}\,\mathrm{nm}^{-2}$
λ_0	$74.36\,\mathrm{nm}$	$73.6\,\mathrm{nm}$	$61.8\,\mathrm{nm}$

Table 6.1: Sellmeier parametrisation for the refractive index of nitrogen gas, C_4F_{10} and CF_4 for λ in nm.

$$N = 370\mathrm{eV}^{-1}\mathrm{cm}^{-1} \times L \int QRT \left(1 - \frac{1}{n(E)^2\beta^2}\right) dE \quad .$$

This equation is a modification of the Frank-Tamm relation from Sec. 4.1, where L is the length of the radiator. Furthermore, in the case of the HPDs we need to introduce an efficiency ε to detect the photoelectrons from the photocathode and if the Cherenkov ring covers more than one HPD an efficiency coming from the HPD's geometrical acceptance η. N_2 events have been used in the subsequent analysis to remove the contribution from this geometrical acceptance.

The refractive index of the gas radiator n varies with photon energy and is described by the Lorentz-Lorenz equation. Using the one pole Sellmeier parametrisation,

$$n - 1 = \frac{S_0}{\lambda_0^{-2} - \lambda^{-2}}$$

The parametrisation of the two gas radiators used in LHC*b* (C_4F_{10} andCF_4) and for nitrogen gas, a radiator used in the beam test are given in Table 6.1. For an ideal gas variations in temperature T and pressure P lead to a change in density,

$$\rho = \rho_{STP} \times \frac{P}{P_{STP}} \frac{T_{STP}}{T}$$

and

$$(n-1) = (n-1)_{STP} \times \frac{P}{P_{STP}} \frac{T_{STP}}{T}$$

Temperature and pressure changes, relative to STP, lead to a change in photon yield of -0.06 ± 0.01 per Kelvin and 0.018 ± 0.04 per mbar in a typical HPD.

As discussed in Sec. 5.3 the most significant contribution to the HPD's efficiency comes from the HPD's quantum efficiency (QE), see Fig. 5.4. The QE is maximum

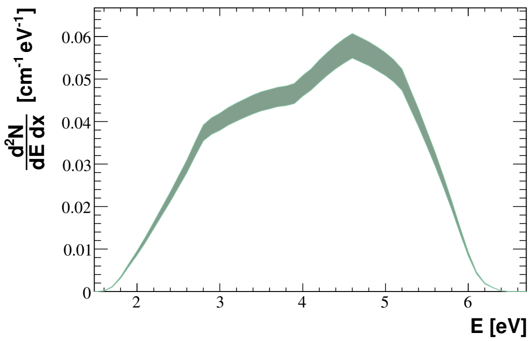

Figure 6.9: The predicted photon yield (per centimetre) as a function of photon energy at T = 296 K and P = 960 mbar for one of the HPDs used in the test beam. The filled area represents the expected 5% uncertainty on the yield in the beam test.

HPD Anode Identifier	N_2	C_4F_{10}
8_133	15.26 ± 0.76	71.27 ± 3.56
9_121	17.55 ± 0.88	81.98 ± 4.01
9_177	16.01 ± 0.80	74.75 ± 3.74

Table 6.2: The expected photoelectron yield for three of the HPDs used in the beam test at the CERN SPS in an 80 GeV/c π^- beam at T = 296 K and P = 960 mbar.

at 270 nm. There is a cut-off at high photon energies (180 nm) coming from UV transmission in quartz. The quantum efficiency is also low in the red, primarily due to the sensitivity of the photocathode which has a photoemission threshold of 1.5 eV. Figure 6.9 demonstrates the typical, differential, photon-yield for one of the HPDs in the beam test.

The expected photoelectron yields for three of the HPDs used in the CERN SPS beam test are provided in Table 6.2. The errors assume a 5% uncertainty of any measurement of the combination of the mirror reflectivity, the quartz transmission and the quantum efficiency measurement at DEP. This 5% represents not only the error on the individual measurements but also a systematic error introduced by interpolating between the measured data points. The dominant source of error is the uncertainty on the QE measurement. This has been estimated at 3-5% by comparing measurements of the QE at DEP with a measurement on a small sub-sample at the test centres.

6.5 Event Selection

For the SPS data, where tracking information was available, events for the photon yield study are selected only if there is a single cluster of hits in each tracking station.

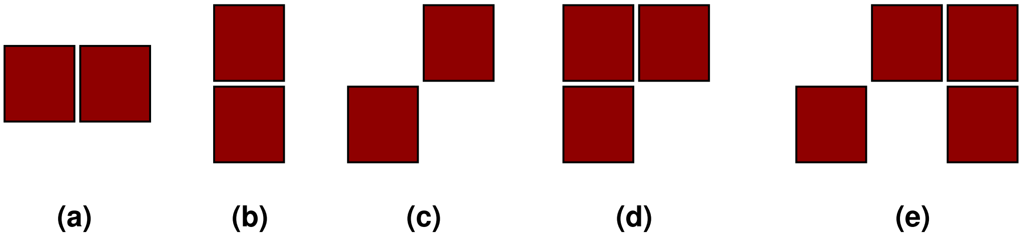

Figure 6.10: From left to right, an example of a horizontal cluster (a), vertical cluster (b), diagonal cluster (c) and three and four pixel clusters (d and e).

For reference a definition of the different types of cluster is provided in Fig. 6.10. The tracker cut is used to ensure that the same sample of events can also be used for angular resolution studies. It has an added benefit that the number of events with two or more particles is also reduced. Due to inefficiencies in the tracking the tracker cuts select approximately 40% of events but no bias is introduced.

Rings are then fitted to the N_2 events on an event-by-event basis (Fig. 6.11) and the average ring centre and radius used to define an annulus, ±3 pixels about this average ring position. Events are selected if:

- There are ≥ 4 hits within the annulus, the minimum number required to fit a circle through the pixel hits on the silicon sensor.
- There are < 3 hits outside the annulus.

These cuts remove empty events and events with large backgrounds and retain 87% of the events passing the tracker cuts.

6.6 Measurements of the Photoelectron Yield

The photoelectron yield is extracted by performing a least-χ^2 fit to the distribution $N(n)$ of the number of hit pixels per event in the selected events.

$$\chi^2 = \sum_{i=4}^{25} \left(\frac{\left(N^{expected}(i) - N^{observed}(i)\right)^2}{N^{observed}(i)} \right)$$

The χ^2 is defined in terms of the expected number of events with i hits $N^{expected}(i)$ and the corresponding observed number $N^{observed}(i)$. The maximum size of the

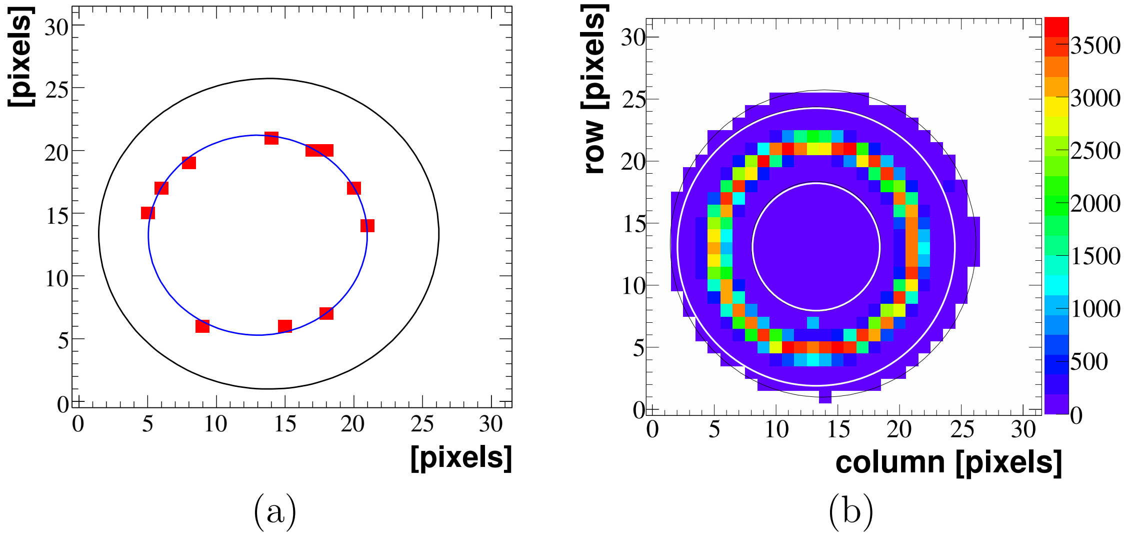

(a) (b)

Figure 6.11: The hit pixels in a typical single event in N_2 gas (a) and events accumulated over an entire run in the same radiator (b). Marked on the single event is the 'best' fit ring position and on the right-hand figure the position of the annulus used for the event selection and the position of the active photocathode area (estimated from LED runs where the entire photocathode surface is illuminated).

event is limited to 25 hit pixels to limit the pull on the fit from a small number of events with very large cluster sizes that sit in the tail. These events have all the characteristics of coming from a charge settling effect but make it through the selection. This fit must take into account:

- Pixel to pixel charge sharing, s, where one photoelectron strikes the pixel sensor near the pixel boundary and produces a hit in a neighbouring pixel.
- Double hits, d, where hits are lost due to two photoelectrons striking a single silicon pixel and only one hit being read out due to the binary readout of the pixel chip.
- The trigger. In the CERN SPS beam test this was a pair of coincidence scintillators which provides no veto of events with more than one beam particle. In practice the rate of events containing more than one particle is small owing to the tracker cut. At the BTF the contribution from events with two or more particles is expected to be negligible owing to the calorimeter cut.
- The beam. At the SPS this contained a mixture of particles, with approximately 80% π^-, 10% electrons, 7% kaons and 3% antiprotons, all above the Cherenkov threshold. At the BTF the beam was a 100% pure beam of electrons. There is however a background from x-rays caused by bremsstrahlung or

more appropriately synchrotron radiation of the electrons in the final magnets before the experimental hall.

If the beam just contains a single particle and detector and timing effects are ignored we expect to see a Poisson distribution $P\left(n|\mu\right)$ of hit pixels, where $\mu = \langle n \rangle$. Taking into account these effects the distribution of hit pixels per event, $N\left(n\right)$ is then given by,

$$\begin{aligned} N(n) \;&=\; N_1 \sum_{i=\pi,K\bar{p}} f_i P(n|\mu_i, s, d) + \\ &\;\; N_2 \sum_{i=\pi,K,\bar{p}} \sum_{j=\pi,K,\bar{p}} f_i f_j P(n|\mu_i + \mu_j, s, d) \end{aligned} \tag{6.1}$$

where f_i is the relative fraction of particles of type i $(= \pi, K\bar{p})$ in the beam,

$$P\left(n|\mu, s, d\right) = \sum_{i=0}^{n} \sum_{j=0}^{\infty} P(n-i+j|\mu)\, \underbrace{P(i|\left(n-i\right)s)}_{charge\ sharing}\, \underbrace{P(j|\left(n-i+j\right)(n-i+j-1)\,d)}_{double\ hits} \tag{6.2}$$

and $P\left(a|b\right)$ is the Poisson probability of getting a given a mean value, b. The three or more particle contribution is assumed to be negligible as is the contribution from events containing two particles where one or more of the particles is not a π^-.

Eq. 6.1 is a sum over the possible particle types and the two particle contribution. The $P\left(n|\mu_i, s, d\right)$ (Eq. 6.2) are Poisson-like probabilities that are the underlying Poisson distribution for the number of hits on a ring, corrected for combinations where hits are gained due to charge sharing or lost due to the binary readout.

In the BTF data sample the beam was not synchronous and particles could arrive at any point within the 25 ns readout window. There is an additional complication of having an efficiency that depends on arrival time $\varepsilon(t)$. $P\left(n|\mu_i, s, d\right)$ becomes

$$\int_{offset}^{25+offset} P\left(n|\mu\varepsilon(t), s, d\right) dt\ . \tag{6.3}$$

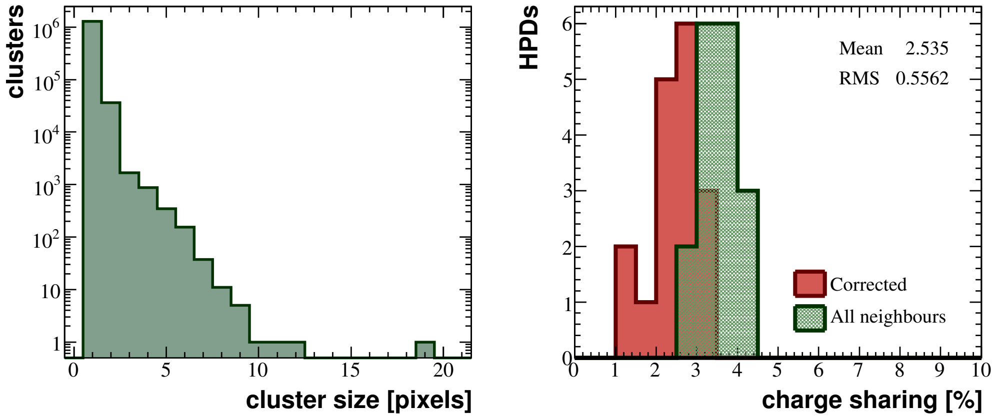

(a) (b)

Figure 6.12: The cluster size distribution measured in a long LED run with 0.82 hits per event on HPD 9_55 (*a*). The probability to observe a two pixel cluster and the probability for charge sharing for a number of HPDs used in beam tests (*b*).

6.6.1 Estimating the Charge Sharing, "s"

The probability per photoelectron for charge sharing was estimated from low intensity LED runs, where the LED is used to illuminate the entire photocathode surface. In this case the probability to get hits in two neighbouring pixels is small and most neighbouring hit pixels arise from charge sharing. The remaining contribution from genuine two pixel clusters was assessed in the data from the number of diagonal clusters. The probability to get such a diagonal cluster from charge sharing is negligible due to the tiny area of the pixel that any photoelectron would have to strike for this to become possible. This assumption has been verified in a toy study (with a mean estimated from, $\mu_{p.e.} = -\ln P(0)$).

The probability per photoelectron for charge sharing is then estimated from the number of two pixel clusters as,

$$s = \frac{N_{clusters} - 2N_{diagonal}}{N_{hits}} \quad .$$

Fig. 6.12(a) illustrates the typical cluster size distribution seen in an LED run (with a mean number of hits per event of 0.82). It is dominated by single isolated hit pixels. The hits in the tail of the distribution have a number of sources: genuine photoelectrons which happen to form a large group (although the probability for this is small), from ion feedback or from micro discharges caused by charge settling effects. Fig. 6.12(b) shows the measured probability to observe a two pixel cluster and the probability, after subtracting the diagonal clusters, for charge sharing. This is 2.56±0.56% averaged over the HPDs and on a HPD-by-HPD basis is correlated to the HPD's threshold. The HPD with the smallest probability has a pixel threshold $> 1500e^-$. This is much larger than the typical threshold from measurements at the test centres.

There are a number of second order, systematic, effects that are not accounted for here: firstly a contribution from ion feedback that leads to an excess of two-pixel clusters and secondly the random arrival time of the photoelectrons within the readout window. If the photoelectron arrives late then one of the two hit pixels may not pass the discriminator threshold until the next clock window.

6.6.2 Estimating the Probability for Double Hits, "d"

The probability to lose a hit as a double can not be measured directly from data. There are two possible methods for estimating this number. The first is to extract it from a Monte Carlo (MC) toy simulation and the second to measure it indirectly in the data by combining different events. In the second approach the idea is to take a single hit at random from a number of different events and combine them to create a new event. The probability to get a double hit can then be estimated from the number of hits in the new events that fall on the same pixel. Both of the approaches have been tried and are consistent. In the second approach it is important to take hits from inside the road to avoid underestimating the double hit probability.

The probability for a double hit is estimated in the MC model by generating a large number of events with the correct ring radius, centre and dispersion as measured in the real data. These are extracted from the event-by-event fitting that performs a least-squares minimisation of the distance of points to a circle,

$$\frac{1}{\sigma^2_{pixel}}\left(\left((x-x_0)^2+(y-y_0)^2\right)^{1/2}-R\right)^2 \quad .$$

The least-squares fit assumes that the points on the ring sit on a circle on the detector plane and is an assumption that holds reasonably well for yield studies but is less suitable for resolution studies. In reality there is some deviation away from this ideal behaviour as the beam strikes the mirror off axis in the horizontal plane (it is on axis in the vertical plane only when the ring image in at the centre of the HPD

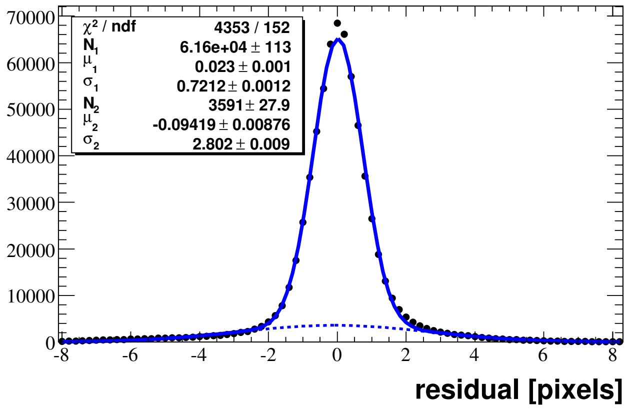

Figure 6.13: The residual difference between points on the ring and the best fit ring through the remainder of the points.

enclosure). This effect, known as the *emission point* effect leads to a broadening of the ring image in the horizontal direction.

Fig. 6.13 shows the hit residual, the distance between a hit pixel and the best fit ring position through the remaining pixels, in events passing the event selection for HPD 9_177. A double Gaussian has been fitted to include the tails of the distribution. These tails result from events with either two or more overlapping Cherenkov rings, noise sitting outside the ring or, in the case of the testbeam at the CERN SPS, from Kaons or from Protons (that have a smaller Cherenkov angle). The central contribution has a width of 360 μm (the image point spread contributes 200 μm and pixelisation 144 μm leaving 260 μm that is associated with the emission point effects and chromatic dispersion).

Fig. 6.14 displays the number of lost hits in events of size n. The number of lost hits is distributed as a Poisson with a mean given by

$$\mu = d \times n$$

where d is the probability per hit of seeing a double hit. It depends linearly (see Fig. 6.15) on the event size and is zero when $n = 1$, i.e.

$$d = 0.0035 \times (n - 1)$$

The same number estimated by combining genuine hits from different events to make new events is 0.0045, with a variation of 3×10^{-4} between HPDs. The difference in values between the two methods can be attributed to charge sharing, which broadens the residual distribution, and the emission point effect.

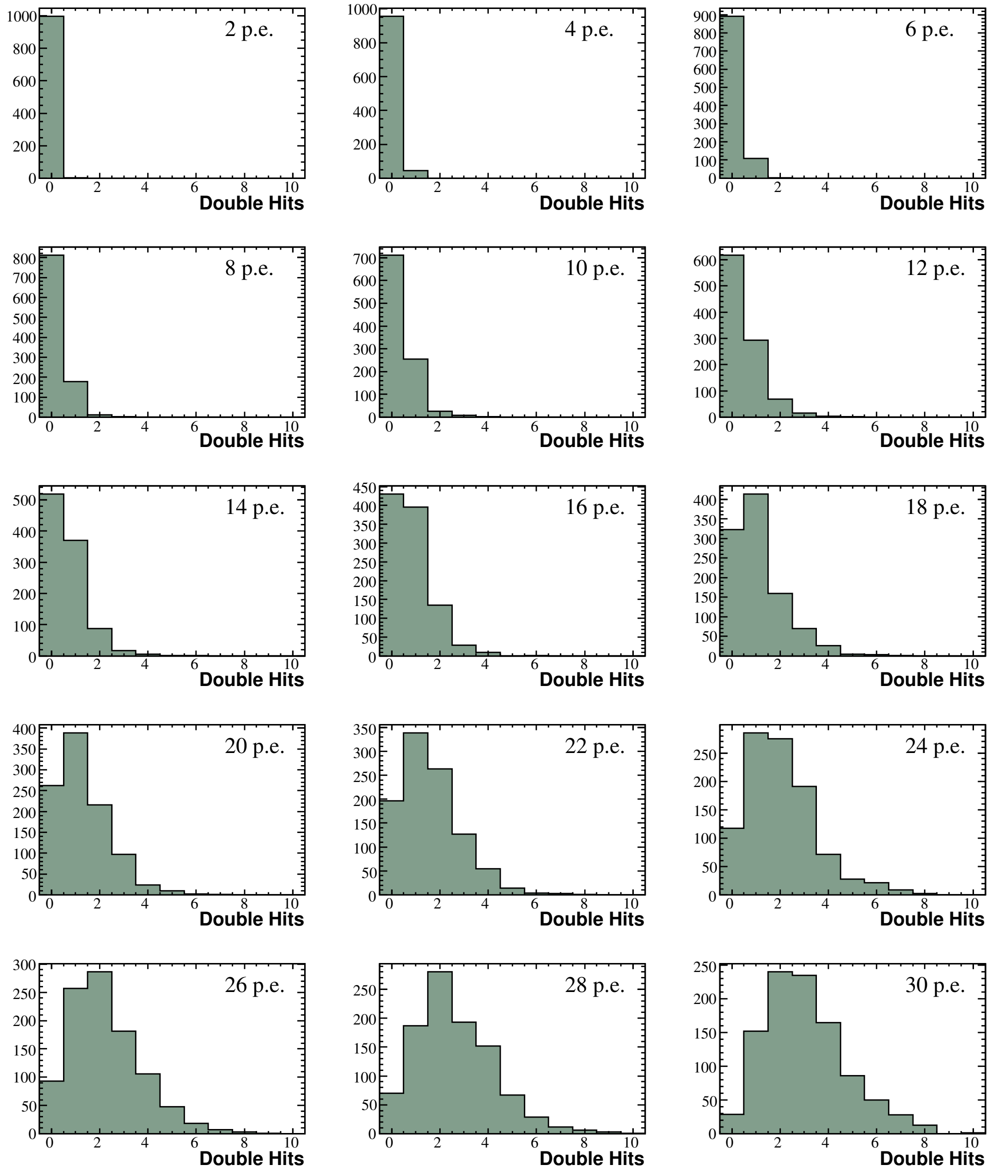

Figure 6.14: The number of lost photoelectrons in an event coming from two or more photoelectrons striking the same binary pixel for various event sizes between 2 and 30 photoelectrons.

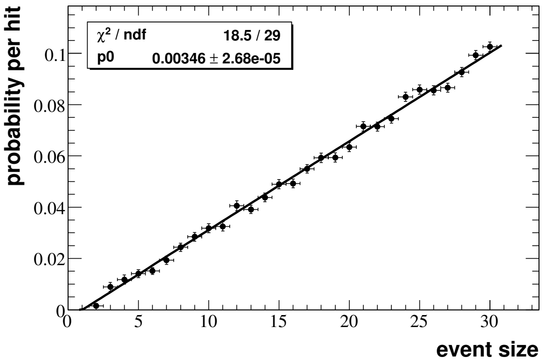

Figure 6.15: Probability per photoelectron of getting a double hit.

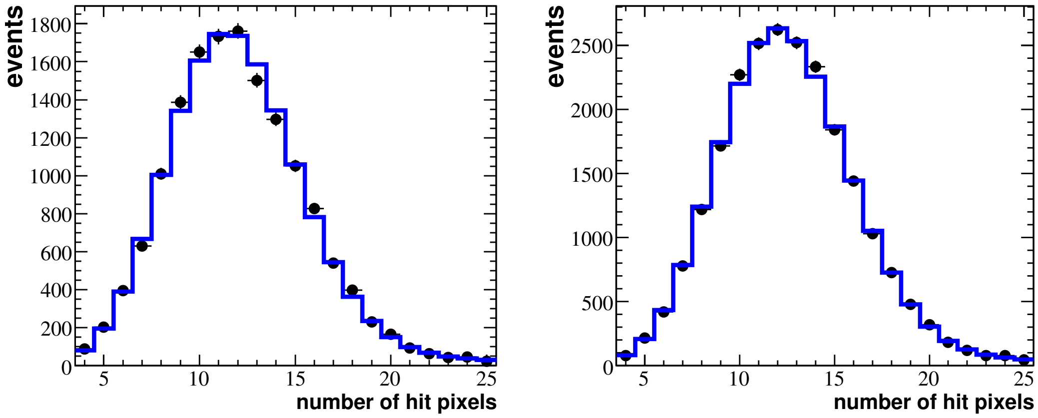

(a) (b)

Figure 6.16: The number of hit pixels per event in a run with the Cherenkov ring centred on HPD 8_133 (a) and HPD 9_121 (b).

6.6.3 Photoelectron Yield in a Synchronous Beam at the SPS

In Fig. 6.16, the distribution of hit pixels per event is compared with the fitted model for two runs on different HPDs. The model (the line) satisfactorily reproduces the data (the points) with $\chi^2/NDF \sim 1$. The best fit model parameters are given in Table. 6.3. The values of s, d and the fraction of kaons and antiprotons are fixed in this fit, leaving three free parameters: the mean number of photoelectrons, the number of one beam particle and the number of two beam particle events. The effect of varying the fixed parameters is discussed below. In each case the expected number of photons in events containing either a kaon or an antiproton is fixed relative to the number of photons produced in a pion event.

HPD	χ^2/NDF	μ_{fit}	N	$N_{2\ \mathrm{particle}}$
8_133	22.72/17	$12.41 \pm 0.04_{\mathrm{fit.}}$	14876 ± 125	356 ± 43
9_121	12.47/17	$13.08 \pm 0.02_{\mathrm{fit.}}$	22756 ± 155	459 ± 60
9_177	15.59/17	$12.60 \pm 0.03_{\mathrm{fit.}}$	19593 ± 143	436 ± 50

Table 6.3: The best fit parameters for the photon yield studies for three HPDs at the CERN SPS.

Estimating Systematic Effects on the Measured Yield

There are additional sources of error on both the measured and the expected yield. For the measured yield there is some uncertainty on the measured value of s and d and on the fraction of pions and kaons in the event. The uncertainties on these are included in the fit using penalty terms added to the χ^2.

$$\chi^2 = \sum_{i=0}^{25} \left(\frac{\left(N_i^{expected} - N_i^{observed}\right)^2}{N_i^{observed}} \right) + \left(\frac{s - \langle s \rangle}{\sigma_s} \right)^2 + \left(\frac{d - \langle d \rangle}{\sigma_d} \right)^2 + \sum_{j=K,p} \left(\frac{N_j - \langle N_j \rangle}{\sigma_{N_j}} \right)^2$$

where $\langle s \rangle \pm \sigma_s$ is the estimate for the charge sharing ($\sigma_s = \pm 0.5$), $\langle d \rangle \pm \sigma_d$ the estimate for the probability for a double hit ($\sigma_d = \pm 0.0004$) and $\langle N_j \rangle$ the estimate for the fraction of a particular particle type (±2%).

The final fit results are provided in Table 6.4 along with the expected number of photoelectrons calculated earlier. The ratio corresponds to the efficiency of the HPD anode and the charge collection efficiency (estimated from the field simulation at 98.5%).

HPD	μ_{fit}	$\mu_{expected}$	*Ratio*
8_133	12.32 ± 0.11	15.23 ± 0.76	0.81 ± 0.04
9_121	13.14 ± 0.12	17.57 ± 0.88	0.75 ± 0.05
9_177	12.56 ± 0.12	15.89 ± 0.80	0.79 ± 0.04

Table 6.4: The fitted photoelectron yield taking systematic effects into account with penalty terms in the fit.

Estimating Systematic Effects on the Expected Yield

The systematic error on the estimated yield includes the uncertainty on QRT and temperature and pressure variations. The temperature and pressure were monitored at the test beam, with temperature varying by 0.5 K and the pressure 1 mbar over the course of typical run. A correction has also been applied for dead pixels (noisy

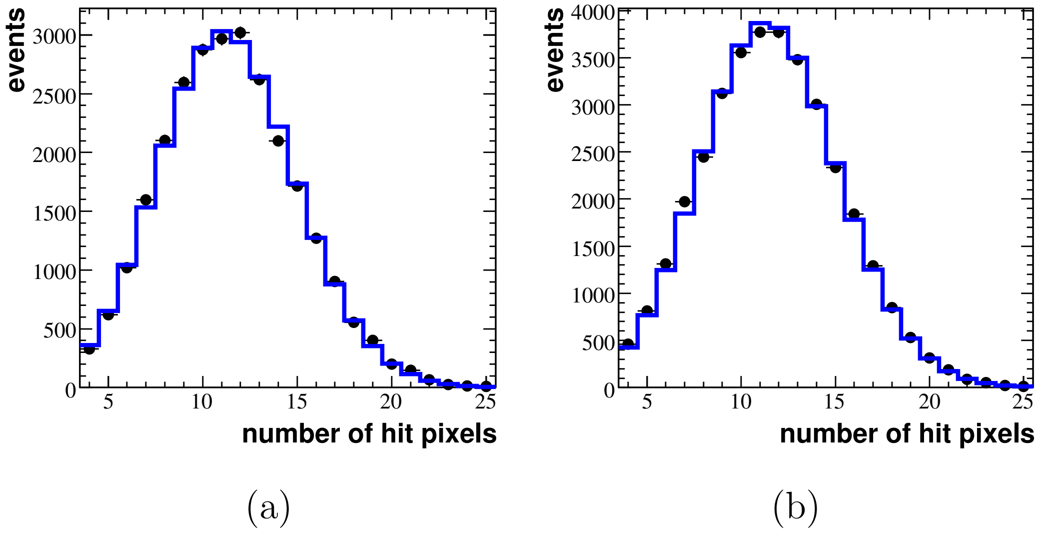

Figure 6.17: The number of hit pixels per event in two runs on different HPDs in the Frascati beam tests, HPD 8_133 (*a*) and 8_130 (*b*).

pixels were also masked and counted as dead for the purpose of this analysis) on the pixel sensor. The HPD with the largest contribution required a correction of 1.8% but this value is typically 0.2%.

6.6.4 Photoelectron Yield in an Asynchronous Beam at the BTF

The distribution in the number of hit pixels in an asynchronous beam is somewhat different. It is an accumulation of a number of different hit distributions with different arrival times and therefore different numbers of photoelectrons per event, sampling a 25 ns window of $\varepsilon(t)$. This has two consequences; the distribution of hit pixels per event is wider and the naïve mean of the distributions is lower than the true mean. Two sample HPDs yielded the distributions shown in Fig. 6.17.

The fitted distribution has a fixed contribution from charge sharing and double hits. The efficiency versus arrival time within the clock has been measured for the HPDs using the fast pulsed laser diode. The time offset of the 25 ns window is measured by fitting the triangular response function achieved by delaying the beam trigger. A summary of the fit results is provided in Table 6.5.

HPD	χ^2/NDF	μ_{fit}	$\mu_{expected}$	*Ratio*
4_11	50.34/17	$13.57 \pm 0.04_{\text{fit.}}$	16.32 ± 0.82	0.83 ± 0.04
8_158	32.97/17	$13.41 \pm 0.04_{\text{fit.}}$	16.55 ± 0.83	0.81 ± 0.04
8_150	45.31/17	$14.08 \pm 0.02_{\text{fit.}}$	17.46 ± 0.87	0.81 ± 0.04
8_104	41.07/17	$14.35 \pm 0.01_{\text{fit.}}$	16.81 ± 0.85	0.85 ± 0.04
8_133	36.28/17	$12.91 \pm 0.03_{\text{fit.}}$	15.47 ± 0.77	0.83 ± 0.04
8_130	28.63/17	$13.15 \pm 0.03_{\text{fit.}}$	15.60 ± 0.78	0.84 ± 0.04
8_128	24.60/17	$13.23 \pm 0.03_{\text{fit.}}$	15.40 ± 0.77	0.86 ± 0.04

Table 6.5: The measured and predicted photoelectron yields at the BTF. The ratio between the two is a measure of the efficiency of the HPD.

Estimating Systematic Effects in an Asynchronous Beam

These are similar to the systematic effects described above for the SPS beam. However there is no contribution from either multiple particles in the beam or contamination from different particles. There is however a new systematic error introduced by the uncertainty on the optimal timing and the 25 ns window of the efficiency curve that contributes in the fit. These have been evaluated explicitly. A breakdown of the systematic error contributions to the photoelectron yield μ_{fit}, is provided for three example HPDs in Table 6.6.

HPD	μ_{fit}	fit.	Δt	s	d
8_158	13.41	0.04	0.08	0.09	0.11
8_150	14.08	0.02	0.07	0.09	0.13
8_104	14.35	0.01	0.06	0.09	0.13

Table 6.6: Contributions to the error on the measured photoelectron yield μ_{fit} at the BTF.

6.7 Summary

The results from the synchronous and asynchronous beam tests at the CERN SPS and the BTF at INFN Frascati are compatible. Fig. 6.18 plots the efficiency of ten HPDs that took part in the SPS or BTF beam tests against the threshold of the pixel chip readout in electrons. There should be some correlation between the HPD threshold and the measured efficiency, with HPDs with the lowest thresholds having the highest efficiencies. The average efficiency across the ten HPDs is,

$$\varepsilon_{\text{collection}} \times \varepsilon_{\text{readout}} = 82 \pm 3\% \quad .$$

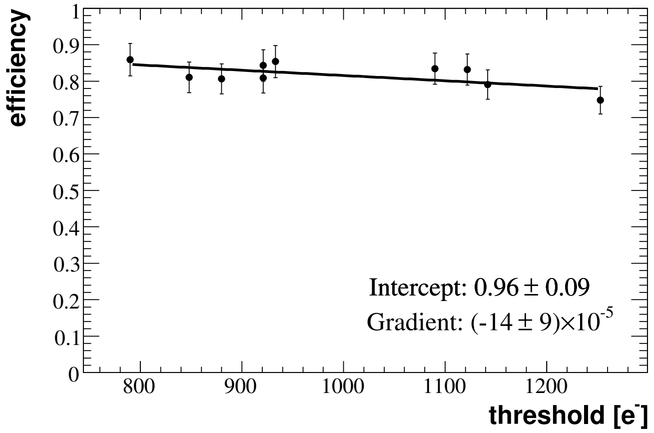

Figure 6.18: The efficiency of 10 HPDs tested in the SPS and BTF beam test plotted against the HPD threshold.

On a HPD-by-HPD basis the efficiency estimate is systematics limited and is dominated by the uncertainty in the HPD QE.

This can be compared with the readout efficiency measured in laboratory tests at 87±2%. A direct comparison need also factor in the charge collection efficiency of the HPDs electron optics, which from the HPD simulation is $\varepsilon_{\mathrm{collection}} \sim 98\%$. The measured efficiencies are then in reasonable agreement, although there is a tendency for the efficiency measured in the beam tests to be lower than that of the laboratory measurements. This discrepancy is predicted by:

- A general increase in the HPD thresholds to cope with the noisier environment.
- The physical size of the ring, which due to the finite propagation time of the strobe across the pixel chip can result in photoelectrons at different positions around the ring seeing different efficiencies.

Chapter 7

$B_d \to K^{*0}\mu^+\mu^-$ at LHC*b*

In Chapter 2 the motivation for studying rare $b \to s\ell^+\ell^-$ decays at LHCb was introduced. There are a number of different observables that are sensitive to a wide variety of new physics models. The properties of inclusive $b \to s\ell^+\ell^-$ decays are difficult to study in the hadronic environment as it will be challenging to make precise measurements of a number of the contributing decays. One of the reasons for this is the difficulty in cleanly reconstructing π^0, K^0_S and K^0_L. At LHCb the main focus is likely to be the exclusive decay modes $B \to (K, K^{*0})\mu^+\mu^-$, where the $K^{*0} \to K^+\pi^-$. In particular, attention has focused on a measurement of the forward-backward asymmetry A_{FB} of the decay. This is the asymmetry between the number of forward and backward going μ^+ (μ^-) with respect to the direction of the B_d ($\overline{B}_d$) in the rest frame of the dimuon pair,

$$A_{FB}(q^2) = \frac{\int_0^1 d\cos\theta_L \frac{d^2\Gamma}{dq^2\ d\cos\theta_L} - \int_{-1}^0 d\cos\theta_L \frac{d^2\Gamma}{dq^2\ d\cos\theta_L}}{\int_{-1}^1 d\cos\theta_L \frac{d^2\Gamma}{dq^2\ d\cos\theta_L}} \quad .$$

The angle θ_L is the angle between the μ^+ (or μ^-) and the B_d ($\overline{B}_d$) and q^2 the invariant mass of the dimuon pair. A full list of the angles used in the analysis is provided in Sec. 7.1.2 below.

The practicalities of this measurement are discussed in this and the following chapter in the context of a Monte Carlo (MC) study. In this chapter the selection and reconstruction of $B_d \to K^{*0}\mu^+\mu^-$ candidates at LHCb and the different sources of background are discussed. The selection highlights a number of different acceptance effects that can complicate a measurement of the A_{FB}. Finally a number of control channels are mentioned along with their strengths and weaknesses.

7.1 Standard Model Predictions for the $b \to s\ell^+\ell^-$ Decays

7.1.1 Predictions for the Decay $B_d \to K^{*0}\mu^+\mu^-$

There are large, $\mathcal{O}(30\%)$, theoretical errors on the SM prediction for the branching fraction and the kinematic distribution of the daughter particles in the exclusive $B_d \to K^{*0}\mu^+\mu^-$ decays. These come predominantly from uncertainties on the form factors describing the $B \to F$ transition, where F is the vector or pseudo-scalar meson in the final state. Good observables (relatively free from theoretical uncertainty) can be found by forming appropriate ratios, where the major uncertainties in the form factors cancel.

The forward backward asymmetry (A_{FB}) described earlier is one such observable. It has a q^2 dependence and flips sign in the Standard Model, with a zero-crossing point q_0^2 related to the Wilson coefficients $\mathcal{C}_7$ and $\mathcal{C}_9$ [79].

$$\mathcal{C}_9 + \Re\left(Y(q_0^2)\right) = -\frac{2M_B m_b}{q_0^2}\mathcal{C}_7^{eff} \quad .$$

$Y(q^2)$ contains contributions from the Wilson coefficients $\mathcal{C}_1$ to $\mathcal{C}_6$ and $\mathcal{C}_7^{eff}$ is $\mathcal{C}_7$ plus contributions from $\mathcal{C}_3$ to $\mathcal{C}_6$. The Wilson coefficients $\mathcal{C}_1$ through $\mathcal{C}_6$ are small compared to $\mathcal{C}_7$, $\mathcal{C}_9$ and $\mathcal{C}_{10}$. $\mathcal{C}_7$ is related to the Standard Model Feynman diagram in Fig. 7.1 containing the photon. The latest prediction for the zero point in the Standard Model is $q_0^2 = 4.39^{+0.38}_{-0.35}\,\text{GeV}^2$ [79]. $q_0^2 = 4\,\text{GeV}^2$ is used throughout the LHCb MC simulation studies.

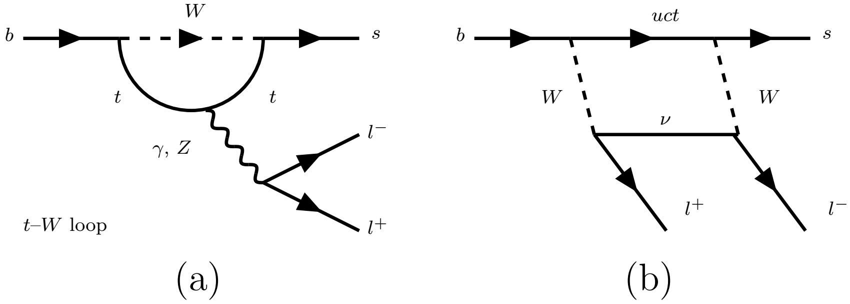

Figure 7.1: Flavour changing neutral current transition $b \to sl^+l^-$ in the Standard Model, mediated by electroweak penguin (a) and box diagrams (b).

Measurements of A_{FB} are limited by theoretical uncertainties to a q^2 range $1 < q^2 < 6\,\text{GeV}^2$. At low-$q^2$ where $\mathcal{C}_7$ dominates, the limit comes from the photon pole as $q^2 \to 0$ and the photon becomes real. The upper limit is set by theoretical uncertainties as we approach the $c\bar{c}$ resonances. Above $1\,\mathrm{GeV}^2$ the number of form factors is also reduced from seven to just two universal form factors. There are experimental challenges as q^2 approaches its lower limit of $q^2 = 4m_\mu^2$. The angular distribution becomes more complex with $L \leftrightarrow R$ cross terms that makes extracting information about the decay more difficult. These left-right cross terms are suppressed by a factor m_μ^2/q^2 and vanish as q^2 increases.

7.1.2 Angular Distribution in $B_d \to K^{*0}\mu^+\mu^-$

The kinematic distribution of particles from the decay can be completely described by three angles and one invariant mass [1], defined as (Fig. 7.2):

- θ_L: The lepton angle is the angle between the μ^+ and the direction of the B_d in the dimuon rest frame. For the decaying $\overline{B}_d$ the μ^- is used to define the lepton angle.
- θ_K: The kaon angle is defined as the angle between the kaon and a vector in the opposite direction to the direction of the B_d or $\overline{B}_d$ in the $K\pi$ rest frame.
- ϕ: This is the angle between the two planes defined by the $\mu^+\mu^-$ pair and the $K\pi$ pair in the rest frame of the B_d or $\overline{B}_d$.

The invariant mass squared of the dimuon pair is the fourth variable. It is defined in the range $4m_\mu^2 < q^2 < (m_B - m_{K\pi})^2$.

The differential decay rate can then be written as [32],

$$\begin{aligned}\frac{d^4\Gamma}{dq^2\ d\cos\theta_l\ d\cos\theta_K\ d\phi} = \frac{9}{32\pi} \Big(& I_1 + I_2\cos 2\theta_L + I_3\sin^2\theta_L\cos 2\phi + I_4\sin 2\theta_L\cos\phi + \\ & I_5\sin\theta_L\cos\phi + I_6\cos\theta_L + I_7\sin\theta_L\sin\phi + \\ & I_8\sin 2\theta_L\sin\phi + I_9\sin^2\theta_L\sin 2\phi \Big)\end{aligned}$$

The $I_{1\ldots9}$ are functions of θ_K and are usually expressed in terms of K^{*0} spin amplitudes, transversity amplitudes A_0, $A_\parallel$ and $A_\perp$. Under the assumption that $q^2 \gg 4m_\mu^2$ the angular expression becomes [32]:

---

[1] If the decay does not go to a $K\pi$ resonance but instead goes to some non-resonant $K\pi$ (s-Wave) final state it is then parametrised by five variables.

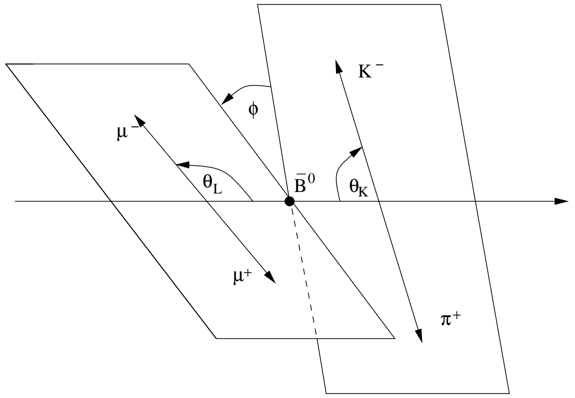

Figure 7.2: Definition of the angular basis used for the decay $B_d \to K^{*0}\mu^+\mu^-$.

$$I_1 = \tfrac{3}{4}\left(|A_{\perp L}|^2 + |A_{\parallel L}|^2 + |A_{\perp R}|^2 + |A_{\parallel R}|^2\right)\sin^2\theta_K + \left(|A_{0L}|^2 + |A_{0R}|^2\right)\cos^2\theta_K$$

$$I_2 = \tfrac{1}{4}\left(|A_{\perp L}|^2 + |A_{\parallel L}|^2 + |A_{\perp R}|^2 + |A_{\parallel R}|^2\right)\sin^2\theta_K - \left(|A_{0L}|^2 + |A_{0R}|^2\right)\cos^2\theta_K$$

$$I_3 = \tfrac{1}{2}\left(|A_{\perp L}|^2 + |A_{\perp R}|^2 - |A_{\parallel L}|^2 - |A_{\parallel R}|^2\right)\sin^2\theta_K$$

$$I_4 = \tfrac{1}{\sqrt{2}}\left(\Re(A_{0L}A^*_{\parallel L}) + \Re(A_{0R}A^*_{\parallel R})\right)\sin 2\theta_K$$

$$I_5 = \sqrt{2}\,(\Re(A_{0L}A^*_{\perp L}) - \Re(A_{0R}A_{\perp R})\sin 2\theta_K$$

$$I_6 = 2\left(\Re(A_{\parallel L}A^*_{\perp L}) - \Re(A_{\parallel R}A^*_{\perp R})\right)\sin^2\theta_K$$

$$I_7 = \sqrt{2}\left(\Im(A_{0L}A^*_{\parallel L}) - \Im(A_{0R}A^*_{\parallel R})\right)\sin 2\theta_K$$

$$I_8 = \tfrac{1}{\sqrt{2}}\left(\Im(A_{0L}A^*_{\perp L}) + \Im(A_{0R}A_{\perp R})\right)\sin 2\theta_K$$

$$I_9 = \left(\Im(A_{\parallel L}A^*_{\perp L}) + \Im(A_{\parallel R}A^*_{\perp R})\right)\sin^2\theta_K$$

The transversity amplitudes contain the Wilson coefficients and the form factors and are dominated by coefficients $\mathcal{C}_7$, $\mathcal{C}_9$ and $\mathcal{C}_{10}$. Integrating out all but one of the angles from the full angular distribution leaves the following angular projections,

$$\frac{d^2\Gamma}{d\theta_L dq^2} = \left[\frac{3}{4}F_L\sin^2\theta_L + \frac{3}{8}\left(1 - F_L\right)\left(1 - \cos^2\theta_L\right) + A_{FB}\cos\theta_L\right]\sin\theta_L$$

$$\frac{d^2\Gamma}{d\theta_K dq^2} = \frac{3}{4}\left[2F_L\cos^2\theta_K + \left(1 - F_L\right)\sin^2\theta_K\right]\sin\theta_K$$

with,

$$F_L(q^2) = \frac{|A_0|^2}{|A_\perp|^2 + |A_\parallel|^2 + |A_0|^2} \quad \text{and} \quad A_{FB}(q^2) = \frac{2\left(\Re(A_{\parallel L}A^*_{\perp L}) - \Re(A_{\parallel R}A^*_{\perp R})\right)}{\left(|A_\perp|^2 + |A_\parallel|^2 + |A_0|^2\right)}$$

F_L is the fraction of longitudinally polarised K^{*0}. Information on A_{FB} can be readily extracted from the angular projections. $A_T^{(2)}$ appears in the ϕ projection only but is suppressed by a factor $(1 - F_L)$ in the SM. This makes it difficult to determine accurately without resorting to a full angular fit. This is technically challenging as the fit has to cope with background distributions and signal efficiencies that are not flat over the four kinematic variables. This is discussed further in Sec. 8.5.

7.1.3 Predictions for $B^+ \to K^+\mu^+\mu^-$

The angular distribution for the decay $B^+ \to K^+\mu^+\mu^-$ is defined by only two variables, q^2 and the lepton angle, θ_L. As such the angular distribution is much simpler [80]. The Hamiltonian includes the usual operators from the $b \to s$ Hamiltonian plus scalar ($\mathcal{O}_S^{(\prime)} \propto (\bar{s}\frac{1}{2}(1 \pm \gamma^5)b)(\bar{l}l)$) and pseudo-scalar operators ($\mathcal{O}_P^{(\prime)} \propto (\bar{s}(1 \pm \gamma^5)b)(\bar{l}\gamma_5 l)$). These are highly suppressed in the Standard Model by the electron or muon mass (over m_W) and vanish under the assumption that $m_l \to 0$. One consequence is a vanishing forward-backward asymmetry in the Standard Model.

The distribution can be written in terms of θ_L as,

$$\frac{d^2\Gamma}{d\theta_L dq^2} = \left[\frac{3}{4}\left(1 - \cos^2\theta_L\right)(1 - F_S) + \frac{1}{2}F_S + A_{FB}\cos\theta_L\right]\sin\theta_L \quad . \tag{7.1}$$

Here F_S is the contribution from Scalar and Pseudo-Scalar processes and is ~ 0 in the SM. F_S and the A_{FB} are expected to remain small in this decay even in the presence of new physics. The existing limits on $B_s \to \mu^+\mu^-$ and branching fraction for $B_d \to K^{*0}\gamma$ limit the A_{FB} to $\pm 2\%$ in most new physics models [81].

7.2 Status of Measurements at the B Factories

The current state of the art measurements of $b \to s\ell^+\ell^-$ decays come from the B-Factories; *BABAR* at the PEP-II e^+ e^- storage ring and Belle at the KEKB e^+ e^-

collider. Both experiments operate predominantly at the $\Upsilon(4S)$ resonance. *BABAR* have observed $57.1^{+13.7}_{-12.5}$ $B_d \to K^{*0}\ell^+\ell^-$ decays in a sample of 229×10^6 $\Upsilon(4S)$ to $B\overline{B}$ decays [82], enabling a measurement of A_{FB} in two bins of q^2. Below the $c\bar{c}$ resonances ($0.1 < q^2 < 8.41\,\mathrm{GeV}^2$) *BABAR* set a lower limit on A_{FB} that is > 0.19 at 95% confidence level and above the resonances provide a measurement of A_{FB}, $A_{FB} = 0.72^{+0.28}_{-0.26} \pm 0.08$. Belle have a larger data sample of 386×10^6 $B\overline{B}$ pairs from the $\Upsilon(4S)$, observing 113.6 ± 13 $B_d \to K^{*0}\ell^+\ell^-$ decays [83]. *BABAR* and Belle use an opposite sign convention for the A_{FB}. The status of measurements at Belle can be seen in Fig. 7.3. *BABAR* and Belle see no forward backward asymmetry in the decay $B^+ \to K\ell^+\ell^-$. These limits still offer a large phase space for new physics models.

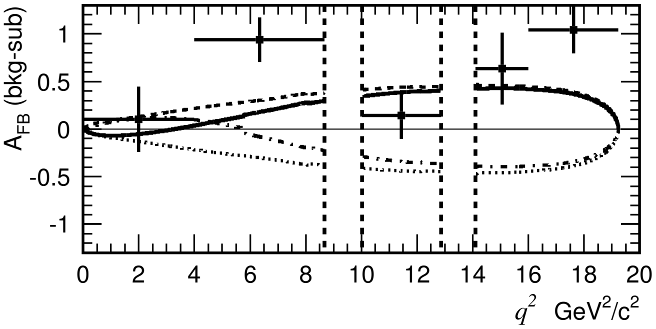

Figure 7.3: Forward-backward asymmetry in $B_d \to K^{*0}\mu^+\mu^-$ versus q^2 as measured by the Belle collaboration. The solid line is the Standard Model prediction and the dashed lines represent several plausible new physics scenarios. The missing regions are the $c\bar{c}$ resonances. From [83].

7.3 Signal and Background Event Simulation

The most recent simulation studies at LHCb, including the one described here, are carried out using data sets produced in the 2006 data challenge (DC06). The signal and background MC samples are produced in the LHCb framework [84]. This is a three step process:

- GAUSS generates events and simulates the behaviour of the detector. The generator process proceeds by simulating the proton-proton collision and hadronizing the quarks and gluons produced in PYTHIA [85]. b hadrons are then decayed by the EvtGen [86] package. EvtGen parametrises the different decay modes of the b-hadron and provides a standard model description of the decay of the signal channel. The second stage of the event generation involves propagating the long-lived particles through the detector and simulation of the energy deposits in detector elements, provided by GEANT 4 [87]. The generation phase also handles any running conditions, e.g. the smearing of the beam due to the size of the proton bunches and any multiple collisions.

- BOOLE then digitises any hits in the detector elements and provides a simulation of the detector front-end electronics. The output of BOOLE is a series of data banks that replicate the data structure seen by the DAQ system in the experiment.
- BRUNEL is the LHC*b* reconstruction package and takes the raw buffers and reconstructs hits in the detector to form 'proto-particle' objects that represent particles in the detector.

The signal sample is a sample of $\sim 420\,\mathrm{k}$ $B_d \rightarrow K^{*0}\mu^+\mu^-$ events that use recent next to leading order calculations for the Wilson coefficients, coming from reference [88]. A cut is applied to the decay products, the $K^{\pm}$, $\pi^{\pm}$, μ^- and μ^+ to ensure that they are inside the detector's geometrical acceptance. The background sample used for these studies is a high statistic inclusive $bb \rightarrow \mu\mu$ sample which requires events to contain at least one b quark and a pair of muons with opposite sign within a 10 mrad-400 mrad acceptance about the beam pipe. This sample is described in more detail below. Earlier studies using simulated data samples from 2004 (DC04) had indicated that the major source of background is from events that contain both real muons and b-quark decays. The rate from non-b inelastic collisions ('minimum bias') is small.

The background coming from inclusive $bb \rightarrow \mu\mu$ events can be classified according to the origin of the pair of muons. These can be,

- $b \rightarrow \mu\mu X$, signal like decays that include $B_d \rightarrow K^{*0}\mu^+\mu^-$ and $B^+ \rightarrow K^+\mu^+\mu^-$.
- $b \rightarrow \mu X(\rightarrow \mu)$, cascade decays such as $B \rightarrow D^-(\rightarrow K^{*0}\mu^-\overline{\nu}_\mu)\mu^+\nu_\mu$.
- $b \rightarrow X(\rightarrow \mu\mu)$, decays like $B \rightarrow K^{*0}J/\psi$ or $B \rightarrow \psi(2S)K^{*0}$.
- $b \rightarrow X(\rightarrow \mu)Y(\rightarrow \mu)$, such as $B \rightarrow D^-D^+$, where the $D^{\pm}$ decays semi-leptonically.

or decays where one of the muons comes from the opposite side b.

Decay mode	
$b \to \mu X(\to \mu)$	37%
$b \to X(\to \mu\mu)$	4%
$b \to X(\to \mu)Y(\to \mu)$	10%
$b \to \mu$, $b \to \mu$	14%
$b \to X\mu$, $b \to X(\to \mu)$	14%
$b \to X(\to \mu)$, $b \to X(\to \mu)$	12%
One or more not from b	9%

Table 7.1: The generator level origin of the muon pairs that make up the $bb \to \mu\mu$ background sample.

- $b \to \mu$, $b \to \mu$
- $b \to X\mu$, $b \to X(\to \mu)$
- $b \to X(\to \mu)$, $b \to X(\to \mu)$

There are also a number of events where the reconstructed muon does not come from a B or can not be associated to a MC particle in the event. A breakdown of the source of the muons at the Generator level is given in Table. 7.1.

7.3.1 Dimuon Event Production

The dimuon background sample is generated with a special fast generation scheme. Inclusive b events are generated using PYTHIA until there is at least one b-quark within a ±400 mrad acceptance about the beam pipe. The hard interaction and fragmentation is then stored in memory and the event repeatedly decayed ten times. A cut is then applied on the particles in the decay and any event passing the dimuon cut is accepted. After ten repeated decays a new inclusive b event is generated. This fast generation scheme avoids the overhead of generating a new b event in PYTHIA but unfortunately can result in multiple selected events coming from the same b quark. These will have different final state particles but the same momentum distribution for the underlying b quark. If the event were to be discarded as soon as it passed the dimuon cut then this would have introduced an altogether different bias. In this case the fraction of selected events from each type of underlying event would be biased. It was felt that this would be a far more problematic bias.

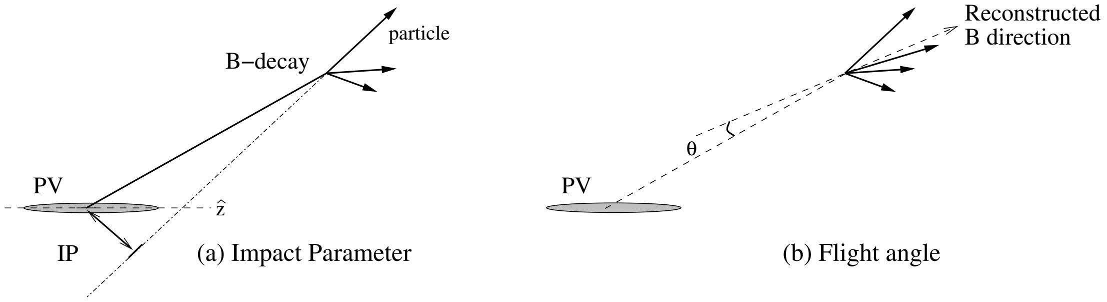

(a) Impact Parameter

(b) Flight angle

Figure 7.4: The impact parameter (a), defined as the distance between the PV and the extrapolated position of a particle at the z-position of the PV. The flight angle (b). The angle between the flight direction of the reconstructed B and the vector between the PV and the reconstructed B vertex.

7.4 Selection of Signal Candidates

Signal candidates are reconstructed and selected by combining a pair of opposite sign tracks that are identified as muons by the muon system and tracks from a kaon and pion, identified using the RICH, and applying a set of selection cuts. The tracks are combined to make the K^{*0} and B_d.

A detailed description of the selection cuts used to identify the $B_d \to K^{*0}\mu^+\mu^-$ candidates can be found in reference [89]. The selection is designed to optimise, on the DC04 data, the signal significance ($S/\sqrt{S+B}$ where S is the number of candidates in the signal sample and B the number in the background sample) whilst minimising the distortion of the dimuon invariant mass spectrum of genuine signal decays. Like the HLT the selection focuses on kinematic cuts, such as cuts on the p_T and Impact Parameter (IP) of the daughter particles, to reduce the background coming from the primary vertex. The impact parameter is defined with respect to the reconstructed position of the primary vertex (PV), or the most significant PV if there is more than one reconstructible primary vertex in the event, by extrapolating the trajectory of the particle. In the LHC*b* framework the impact parameter is signed and the sign represents whether the extrapolated track crosses the axis upstream or downstream of the the position of the PV. In addition, for the K^{*0} and the B_d, a cut is applied to the quality of the reconstructed vertex and the flight distance (or significance from the PV). This cut is motivated by the finite lifetime of the B_d. The lifetime bias that this introduces is not a problem for this analysis. A list of the full selection cuts is given in Table 7.2. A set of pre-selection cuts is also provided. These can be viewed as a minimal set of selection cuts that is required to reconstruct the candidates.

Cut description	Pre-selection value	Selection value
B_d p_T	–	$p_T > 250\,\mathrm{MeV}/c$
B_d Vertex χ^2	< 30	< 20
B_d Flight Angle	$\cos\theta > 0.995$	$\cos\theta > 0.99975$
B_d Flight Distance	–	$> 6\,\mathrm{mm}$
B_d Impact Parameter Significance	–	< 5
K^* p_T	–	$> 300\,\mathrm{MeV}/c$
K^* Vertex χ^2	< 25	< 25
K^* Flight Significance	–	> 1
K^* Impact Parameter Significance	–	1.5
$K^{\pm}$ momentum	–	$> 2000\,\mathrm{MeV}/c$
$K^{\pm}$ p_T	–	$> 400\,\mathrm{MeV}/c$
$K^{\pm}$ Impact Parameter Significance	> 1.5	> 3
$\pi^{\pm}$ momentum	–	$> 200\,\mathrm{MeV}/c$
$\pi^{\pm}$ p_T	–	$> 250\,\mathrm{MeV}/c$
$\pi^{\pm}$ Impact Parameter Significance	> 1.5	> 3
Dimuon Vertex χ^2	–	< 15
Dimuon Flight Distance	–	$> 1\,\mathrm{mm}$
$\mu^{\pm}$ momentum	–	$> 4000\,\mathrm{MeV}/c$
$\mu^{\pm}$ p_T	–	$> 500\,\mathrm{MeV}/c$
$\mu^{\pm}$ Impact Parameter Significance	–	> 2

Table 7.2: The selection and pre-selection cuts used to signal, $B_d \rightarrow K^{*0}\mu^+\mu^-$, candidates. A number of these cut on the significance of the measurement, the measured value divided by the error on this measured value, rather than the absolute value.

The flight-angle cut in Table 7.2 is a cut on the angle between the reconstructed direction of the B_d ($\vec{v_B}$) and the vector $\vec{v_{PV}}$ from the PV to the reconstructed position of the decaying B_d (Fig. 7.4)

$$\vec{v}_B.\vec{v_{PV}} = v_B v_{PV} \cos\theta \quad .$$

The $b\bar{b}$ pairs come from the PV so for real decaying B_d's this angle peaks close to zero.

For the subsequent discussion a tight (5279±50 MeV) and loose (5279±500 MeV) mass window have been defined. Where signal-to-background ratios are discussed, these refer to the ratio in the tight mass window. The selection masks out the q^2 region occupied by the J/ψ and $\psi(2S)$ mass peaks. These will be used separately as a control channel.

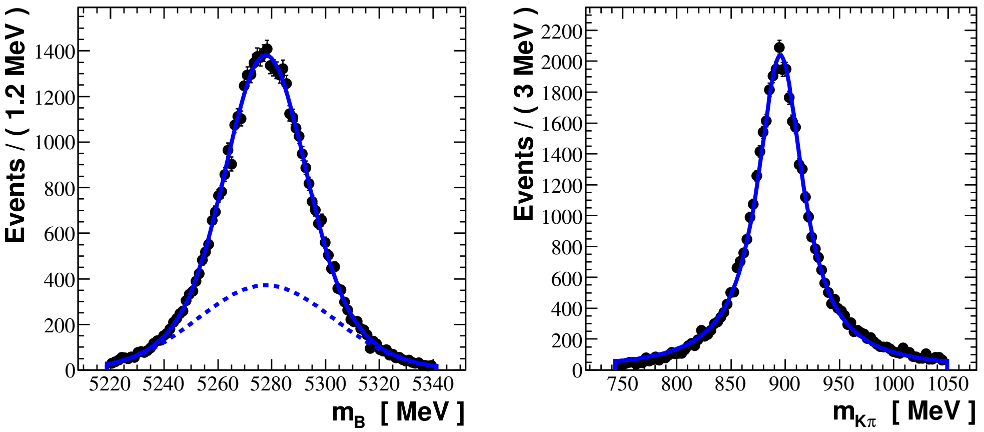

Figure 7.5: The B and K^{*0} mass distributions for reconstructed $B_d \to K^{*0}\mu^+\mu^-$ decays.

7.5 Signal Distribution after Selection Cuts

The distributions of the B mass (m_B) and the $K\pi$ mass ($m_{K\pi}$) after the selection cuts for signal $B_d \to K^{*0}\mu^+\mu^-$ events are shown in Fig. 7.5. The angular distributions are not shown here but are discussed in detail in the next chapter.

The reconstructed B mass is fitted with a double Gaussian, with $\sigma_1 = 13.9 \pm 0.3\,\text{MeV}$ and $\sigma_2 = 25.3 \pm 0.8\,\text{MeV}$. A single Gaussian fit has a width of 18 MeV. There is no bias in the reconstructed B mass. The K^{*0} mass distribution is fitted with a Breit Wigner distribution with a width of $51.3 \pm 0.4\,\text{MeV}$. The dimuon mass distribution is demonstrated in Fig. 7.6. In total 96% of the selected signal events are within the tight $\pm 50\,\text{MeV}$ mass window.

7.6 Background Distribution after Selection Cuts

The background sample is a sample of 9 million events containing b-quarks decaying to a pair of muons in the detectors' geometrical acceptance. This sample will naturally contain a large number of $B \to K^{*0}J/\psi$ ($J/\psi \to \mu^+\mu^-$) events that pass the selection cuts with a reasonable efficiency. These can clearly be seen in Fig. 7.7. Figure 7.7(a) plots the B mass distribution of the selected events and Fig. 7.7(b) the dimuon invariant mass distribution after the full selection cuts have been applied. The dimuon invariant mass peaks at $m_{J/\psi} = 3096\,\text{MeV}$ and $m_{\psi(2S)} = 3686$ with the B mass inside the tight mass window. The branching fraction of $B \to K^{*0}J/\psi$ is $1.33 \pm 0.06 \times 10^{-6}$ and $J/\psi \to \mu^+\mu^-$, $5.93 \pm 0.06\%$. The combined ratio is orders of

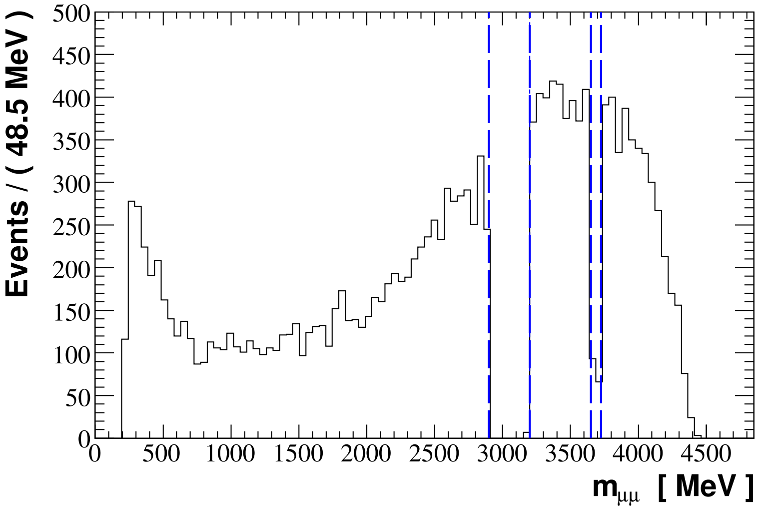

Figure 7.6: Dimuon mass spectrum for muons from the decay $B_d \to K^{*0}\mu^+\mu^-$. The dashed lines are an exclusion region around the position of the J/ψ and the $\psi(2S)$ resonances.

magnitude higher than the signal channel and these events will have a high selection and trigger efficiency. It is likely that these events will need to be pre-scaled in the high-level-trigger.

If the events in the dimuon mass windows $2900-3200$ MeV and $3650-3725$ MeV are ignored the background, in the wide B mass window, is mainly combinatorial events (54%). These are events where the daughters of more than one of the decaying b-hadrons, or particles coming from the PV, are combined to fake a $B_d \to K^{*0}\mu^+\mu^-$ candidate. There is also a non-negligible contribution (16%) of events containing one or more *ghost* tracks. These are reconstructed particles that have no associated Monte Carlo particle and where a reconstructed track could come from; the combination of two or more genuine tracks or from random hits in the detector that are combined to form a track. A large proportion of the remaining background comes from low mass backgrounds where a particle decays to the same final state with some additional particles. Examples of this could be cascade $b \to c(\to \mu)\mu$ decays or even $B \to K^{*0}J/\psi$ decay, where $J/\psi \to \mu^+\mu^-\gamma$ and the γ is not reconstructed and the J/ψ sits outside the masked mass window. In each of the low mass backgrounds the B mass should sit below its true value. If the B mass window is tightened to $\pm 50\,\mathrm{GeV}/c$ the fraction of ghosts falls to 7% and combinatorial background to 33%. Generally the ghost rate can be reduced by tightening the p_T or IP cuts or by cutting on the track quality (track χ^2). The B mass distribution of the signal candidates from the background distribution, in the wide mass window, is plotted in Fig. 7.8(a). The line is the distribution of the preselected candidates and the

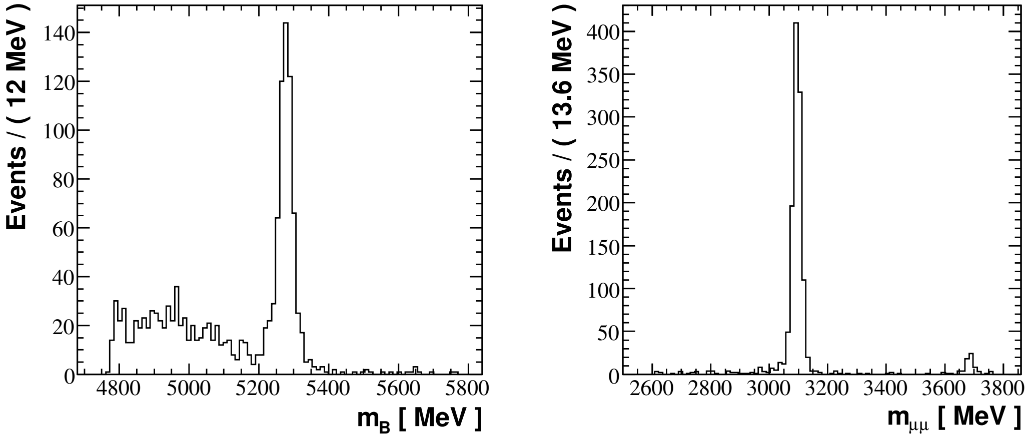

(a) (b)

Figure 7.7: The B (a) and dimuon (b) mass of candidates from the background sample after the selection cuts have been applied if the J/ψ and $\psi(2S)$ mass peaks are not masked.

points the candidates after the full selection cuts. Less than two candidates are selected for every million dimuon events. The B mass distribution of the selected candidates is plotted again in Fig. 7.8(b). These candidates have a small peaking component within the tight mass window coming from wrongly reconstructed B decays. Examples of these are:

- $B_s \to \phi\,(\to K^+K^-)\,\mu^+\mu^-$ where either the K^+ (K^-) is identified as a π^+ (π^-).
- $B_d \to K^{*0}\,(\to K^+\pi^-)\,J/\psi\,(\to \mu^+\mu^-)$ where the π^- is reconstructed as a μ^- and the μ^- a π^-. This event would clearly sit outside the J/ψ mass window.

Fortunately these peaking backgrounds can be removed by simply applying vetoes on mass combinations. For example in the first case by labelling the $\pi^\pm$ as a $K^\pm$ and by applying a cut on the ϕ mass (for more details see referenence [90]). A similar method can be applied to the second case by trying $\pi^\pm$ $\mu^\mp$ (or $K^\pm$ $\mu^\mp$) combinations and rejecting any events where the combination sits inside the J/ψ or $\psi(2S)$ window.

7.6.1 Cascade, $b \to c(\to \mu)\mu$ decays

A particularly dangerous class of backgrounds arises from events where there is some correlation between the momentum of the daughter particles. This can lead to a

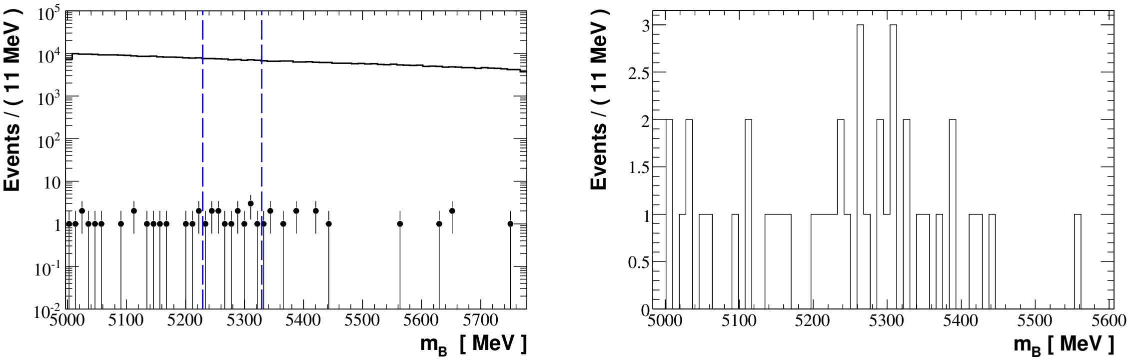

(a) (b)

Figure 7.8: The distribution of background events after the pre-selection cuts (a) and the remaining events after the selection (points in (a) and (b)). The dashed lines highlight the signal B mass window.

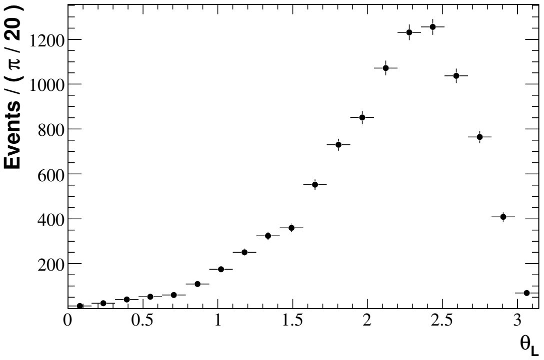

Figure 7.9: The lepton angle distribution in cascade, $b \to c(\to \mu)\mu$ decays.

background distribution in θ_L or θ_K that has a large forward backward bias and will bias any measurement of the A_{FB}. One example of this class of backgrounds is cascade $b \to c(\to \mu)\mu$ decays. These cascade $b \to c(\to \mu)\mu$ decays are a particularly problematic source of background as the μ^+ and μ^- have a different momentum spectrum. For example in the rest frame of the B in the decays $B \to D^-\mu^+\nu_\mu$ and $D^- \to K^{*0}\mu^-\overline{\nu}_\mu$ the μ^+ will have a larger energy than the μ^-. This in turn will bias the angular distribution of the muons in the dimuon rest frame and leads to a peaking distribution that favours backward over forward events. The θ_L distribution of these events in the dimuon background sample, before selection cuts are applied, can be seen in Fig. 7.9.

7.6.2 Loose Selection of Background Candidates

It is difficult to draw any strong conclusions on the background mass and angular distributions with this handful of events. To enable a sensitivity study with a somewhat realistic background distribution the selection cuts have been loosened to provide the set of loose cuts in Table 7.3. Each of the selection cuts has been loosened to accept a greater number of candidates in the $bb \to \mu\mu$ events.

The background mass distribution in three of the interesting observables; m_B, θ_L and θ_K for $1 < q^2 < 6\,\mathrm{GeV}^2$ with the loose cuts applied is shown in Fig. 7.10. The mass distribution is well approximated by an exponential distribution, with a coefficient $-(1.32 \pm 0.07) \times 10^{-3}\,\mathrm{MeV}^{-1}$. A fourth order (Chebychev) polynomial is fitted to both the θ_L and θ_K distributions. The shape of the θ_L distribution strongly depends on the value of q^2. At high q^2 the peaks in Fig. 7.10(b) disappear. These peaks come predominantly from ghost particles, which are much more prevalent in reconstructed candidates with low q^2.

Cut description	Selection value	Loose Selection
B_d p_T	$p_T > 250\,\mathrm{MeV}/c$	$100\,\mathrm{MeV}/c$
B_d Vertex χ^2	< 20	< 30
B_d Flight Angle	$\cos(\theta) > 0.99975$	$\cos(\theta) > 0.995$
B_d Flight Distance	$> 6\,\mathrm{mm}$	$> 2\,\mathrm{mm}$
B_d Impact Parameter Significance	< 5	< 10
K^* p_T	$> 300\,\mathrm{MeV}/c$	$100\,\mathrm{MeV}/c$
K^* Vertex χ^2	< 25	< 25
K^* Flight Significance	> 1	–
K^* Impact Parameter Significance	1.5	–
$K^\pm$ momentum	$> 2000\,\mathrm{MeV}/c$	$> 1000\,\mathrm{MeV}/c$
$K^\pm$ p_T	$> 400\,\mathrm{MeV}/c$	$> 200\,\mathrm{MeV}/c$
$K^\pm$ Impact Parameter Significance	> 3	> 1.5
$\pi^\pm$ momentum	$> 2000\,\mathrm{MeV}/c$	$> 1000\,\mathrm{MeV}/c$
$\pi^\pm$ p_T	$> 250\,\mathrm{MeV}/c$	$> 100\,\mathrm{MeV}/c$
$\pi^\pm$ Impact Parameter Significance	> 3	> 1.5
Dimuon Vertex χ^2	< 15	< 100
Dimuon Flight Distance	$> 1\,\mathrm{mm}$	–
$\mu^\pm$ momentum	$> 4000\,\mathrm{MeV}/c$	$2000\,\mathrm{MeV}/c$
$\mu^\pm$ p_T	$> 500\,\mathrm{MeV}/c$	$250\,\mathrm{MeV}/c$
$\mu^\pm$ Impact Parameter Significance	> 2	> 1

Table 7.3: Loose selection cuts used in the sensitivity study with the final selection cuts for comparison.

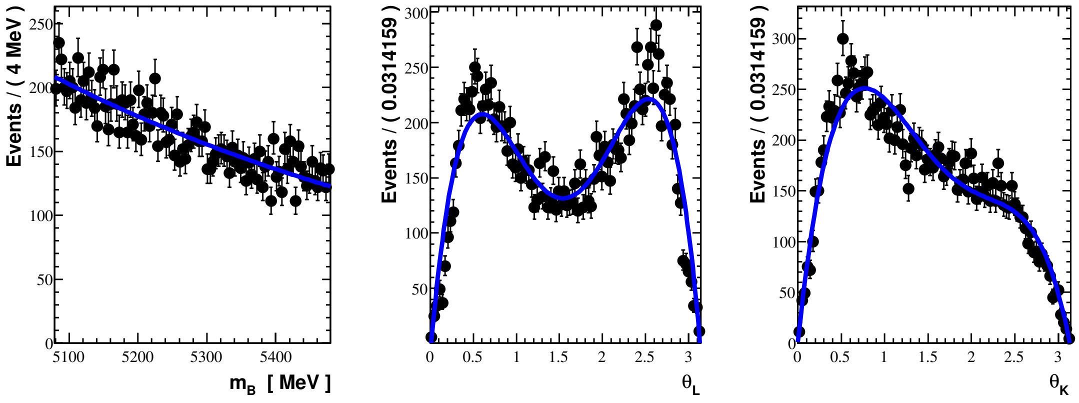

(a) (b) (c)

Figure 7.10: Background distribution in m_B, θ_L and θ_K for dimuon events passing the loose cuts $(1 < q^2 < 6\,\mathrm{GeV}^2)$.

7.7 Expected Signal and Background Yields

The expected number of signal candidates from genuine $B_d \to K^{*0}\mu^+\mu^-$ decays in a nominal year of data taking is given by

$$N_{signal} = N_{b\bar{b}} \times \frac{2}{3} \times 1.22 \times 10^{-6} \times 0.349 \times 0.405 \times \underbrace{\varepsilon_{reco.} \times \varepsilon_{sel.} \times \varepsilon_{trigger}}_{0.042}$$

where the factor of $\frac{2}{3}$ accounts for the branching fraction of the K^{*0} to a charged kaon and pion. The factor 0.405 is the fraction of events where b quarks that are hadronised to form B_d mesons and the 0.349 the fraction of $B_d \to K^{*0}\mu^+\mu^-$ decays with the muons, pion and kaon produced within the 400 mrad geometrical acceptance. For reference the PYTHIA tune used by LHCb produces B_d s 40.5%, B^+ s 40.5%, B_s s 9.9% and Λ_b s 9.1% of the time a b-quark is hadronised. The L0 trigger efficiency ε_{L0} is 93% for reconstructible, selected events. The 4.2% product of efficiencies does not include the HLT efficiency, which is expected to be greater than 90%.

The total signal yield is slightly lower than seen in the DC04 data, $\sim$ 4600 in DC06 compared to $\sim$ 7000 in DC04. It should be compared to the expected number of candidates that will be selected from the background,

$$N_{bkg.} = N_{b\bar{b}} \times 0.438 \times 0.022 \times \varepsilon_{reco.} \times \varepsilon_{sel.} \times \varepsilon_{L0}$$

where 0.438 is the probability to get the *b*-quark in the detectors geometrical acceptance and 0.022 is the probability for an event containing a $b\bar{b}$ pair to decay to a final state with a pair of opposite sign muons. These muons are also required to be inside the acceptance. The selection efficiency for events in this background sample is 1.7×10^{-6}. This implies that on average $14,500 \pm 3,700$ candidates will be wrongly selected in the same nominal year. The error is purely statistical.

Unfortunately the background levels are also higher in the DC06 simulation than in DC04. This is expected as the DC06 data represents a big leap forward in the realism of the detector simulation. For example this includes the revised image point spread and HPD efficiency discussed in Chapters 5 and 6 that impact the PID performance of the RICH. More crucially it contains a much more complete description of the material in the detector that leads to large numbers of secondary particles. In the DC06 data samples the signal-to-background ratio $S/B = N_{signal}/N_{bkg.} \sim 0.28$ (with a signal significance of $S/\sqrt{S+B} \simeq 33$). This is a factor of seven less than the $S/B \sim 2$ seen in the DC04 data. It should be stressed that the selection cuts have not been re-optimised for DC06 and it is likely that by tuning the cuts the S/B ratio will approach its DC04 value. Work on this is ongoing and colleagues have been able to achieve S/B ratios close to those achieved on the DC04 data albeit at a slightly reduced signal yield of $\sim$ 5700 events per nominal year [91]. In the subsequent analysis in Chapter 8 the DC04 numbers and ratios will be used, i.e. $N_{signal.} = 7000$ and $S/B = 2$.

7.8 Biases Introduced by Acceptance Effects

The forward backward asymmetry is measured from the kinematic distribution of the daughter particles, the two muons in the decay. Unfortunately the p_T and IP of the daughters is correlated with the angular variables (θ_L and θ_K) that are being measured. The p_T and IP cuts, presented in Table 7.2, are generally very good at reducing the background but as a consequence of the correlation between the daughter p_T and IP and θ_L (or θ_K) they can introduce a bias in the angular distribution. The term acceptance is used to refer to an efficiency to reconstruct candidates that is a function of one of the angles in the decay. These acceptance

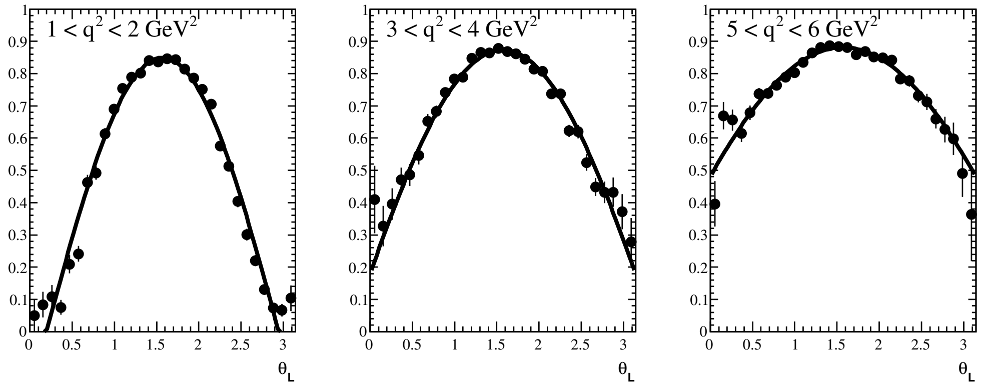

Figure 7.11: p_T cut induced acceptance effect in 3 bins of q^2 below the $c\overline{c}$ resonances. The lines are a fit, $a_0\left(1 - a_1(\theta_L - \frac{\pi}{2})^2\right)$.

effects should not be confused with the detector's geometrical acceptance mentioned earlier.

An example of such an acceptance effect on θ_L is shown in Fig. 7.11. This has been achieved by introducing a 300 MeV/c p_T cut in a large sample of $B_d \rightarrow K^{*0}\mu^+\mu^-$ generator level MC decays (using the MC truth information for θ_L and the muon p_T) and comparing the angular distribution before and after the cut. The figure separates the acceptance effect out into three different dimuon invariant mass bins, each of which has been fitted with a parabola,

$$a_0\left(1 - a_1(\theta_L - \frac{\pi}{2})^2\right)$$

a_1 characterises an efficiency that is not flat across the angle and varies with q^2. In the case of this simple p_T cut a_1 varies linearly with q^2 below 6 GeV^2 (with a gradient $-0.13\,\text{GeV}^{-2}$). If the A_{FB} is constant in the bin in q^2 then the θ_L acceptance will be symmetric about $\frac{\pi}{2}$. This symmetry is guaranteed by the definition of θ_L because, apart from their charge, the two particles (muons) defining θ_L are identical. For every forward μ^+ there is a backward μ^- and vice versa. If the same kinematic cuts are applied to the muons then the acceptance will be symmetrical about $\frac{\pi}{2}$. Furthermore, because B_d decays are defined with respect to the μ^+ and $\overline{B}_d$ to the μ^- any asymmetry will be lost in the combined distribution.

The acceptance effect in Fig. 7.11 comes from a correlation between the momentum of the muons and the angle θ_L (likewise the angle θ_K is correlated to the kaon momentum). This is demonstrated in Fig. 7.12. At small or large angles one of the

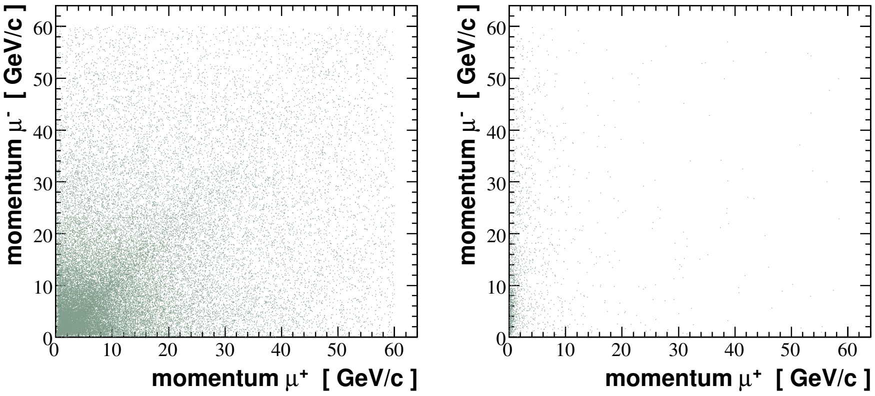

(a) (b)

Figure 7.12: Correlation between the momentum of the μ^+ and μ^- in decays where the lepton angle is close to $\frac{\pi}{2}$ (a) and close to 0 or to π (b).

muons tends to carry away more momentum than the other (Fig. 7.12(b)), however around $\frac{\pi}{2}$ the muons have a similar distribution of momentum (Fig. 7.12(a)). Conversely cutting on the momentum or p_T of just a single muon in the decay introduces an acceptance effect that preferentially favours forward or backward going events.

Similar effects are introduced by cutting on the IP or the IP significance of the muons with respect to the PV. The angle of the muons in the dimuon rest frame clearly has some correlation with the impact parameter and we would expect the IP to be smaller when θ_L is around zero or π and, in the dimuon rest frame, the muons point along the direction of the B_d. The B_d itself will come from the PV.

Any cuts that are applied to the composite particles, the K^* or the B_d, do not introduce an acceptance effect. These include cuts on the B_d flight distance, the vertex χ^2 of the B_d or K^{*0} vertex or the B_d, K^{*0} or dimuon momentum and p_T. The angular acceptances will bias any measurement of the θ_L and θ_K distributions and it might be seen as a good idea to try and reduce these by loosening the kinematic cuts on the daughters and tightening the cuts on the B_d, dimuon or K^* instead. Unfortunately this exercise is academic, as will be shown in Sec. 7.9 and 7.10 because the trigger and the particle reconstruction both introduce their own acceptances that will need to be accounted for.

	L0 Accepted	L0 Muon	L0 Dimuon
$B_d \to K^{*0}\mu^+\mu^-$ events	81.2 %	52.6 %	42.3 %
Pre-selected signal events	92 %	61.8 %	61.7 %

Table 7.4: L0 Trigger efficiency.

7.9 The Trigger

7.9.1 The Level-0 Trigger

The Level-0 (L0) trigger strategy has already been discussed in some detail in Sec. 3.7. The most significant aspects for $B_d \to K^{*0}\mu^+\mu^-$ are the muon and dimuon trigger, through which most of the candidates come. The L0 single muon trigger requires a single muon candidate with $p_T > 1.3\,\mathrm{GeV}/c$ and the dimuon trigger a pair of muons with ${p_T}^{muon\,1} + {p_T}^{muon\,2} > 1.5\,\mathrm{GeV}/c$. There is also a requirement that the lowest momentum muon in the pair has a $p_T > 200\,\mathrm{MeV}/c$. The L0 trigger calculates the p_T of the muons assuming that the tracks emerge from the PV, the tracks are straight in the $y - z$ plane and that the particle receives a kick in the $x - z$ plane at the centre of the magnet.

For a particle of momentum p with charge q, moving in a magnetic field $\vec{B}$ the p_T kick will be,

$$ {p_T}^{kick} = \frac{q}{p} \int B_y dz \quad . $$

The p_T is estimated using hits in stations M1-M4 (and can use M5), this p_T kick and the PV as a constraint. The L0 efficiency and the efficiency of the single muon and dimuon channels are provided in Table 7.4 for both raw $B_d \to K^{*0}\mu^+\mu^-$ events and for events that can be reconstructed with a loose pre-selection. The trigger efficiency is 81.2% on raw $B_d \to K^{*0}\mu^+\mu^-$ events and 92 % on events that have been reconstructed and pre-selected offline.

Fig. 7.13 demonstrates the efficiency versus q^2 and θ_L for the L0, L0 muon and L0 dimuon triggers. The trigger has introduced a series of p_T cuts and these introduce an angular acceptance. This acceptance is a particular issue for the L0 dimuon trigger but overall the L0 efficiency is relatively flat in θ_L.

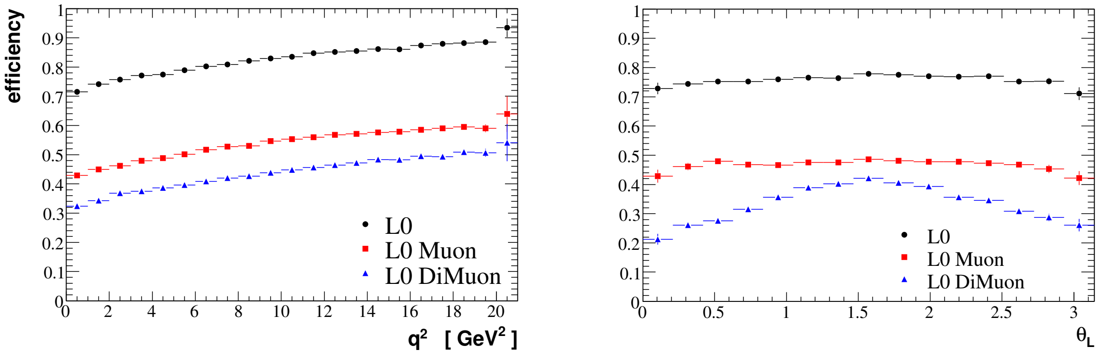

(a) (b)

Figure 7.13: The L0 trigger efficiency versus q^2 (a) and θ_L (b) for events with $1 < q^2 < 6\,\mathrm{GeV}^2$.

7.9.2 High-Level-Trigger

The impact of the High-Level-Trigger (HLT) is not mentioned here. At the time of writing the HLT development is still on going but it is likely that the final stages of the HLT will apply a set of cuts very similar to those described in Sec. 7.4 albeit without particle ID information from the RICH detectors which is not available in the HLT.

7.10 The Reconstruction

The reconstruction of the candidate B_d's takes four charged tracks; two identified as muons in the detector, one identified as a pion and one as a kaon. In reconstructing these daughter particles there is an extra set of cuts that are applied. For example kaons are identified as particles with long tracks, tracks that pass through all of the tracking stations, and a cut on the $DLL(K-\pi)$. The $DLL(K-\pi)$ is the difference in log-likelihoods between the kaon and pion hypothesis from the RICH detectors.

The muon reconstruction applies a much stronger cut, this time on the muon momentum. For a track in the detector to be identified as a muon it must pass through the tracking stations and leave hits in the muon stations. There is a large amount of material between the calorimeters and only muons above a certain threshold momentum should be able to reach later stations. These criteria are given in Table 7.5. For example for a muon to leave hits in stations M2, M3 and either M4 or M5 but not M4 and M5 it must have a momentum p in the range $6 < p < 10\,\mathrm{GeV}/c$. These are already applied at the pre-selection stage and are independent of the selection.

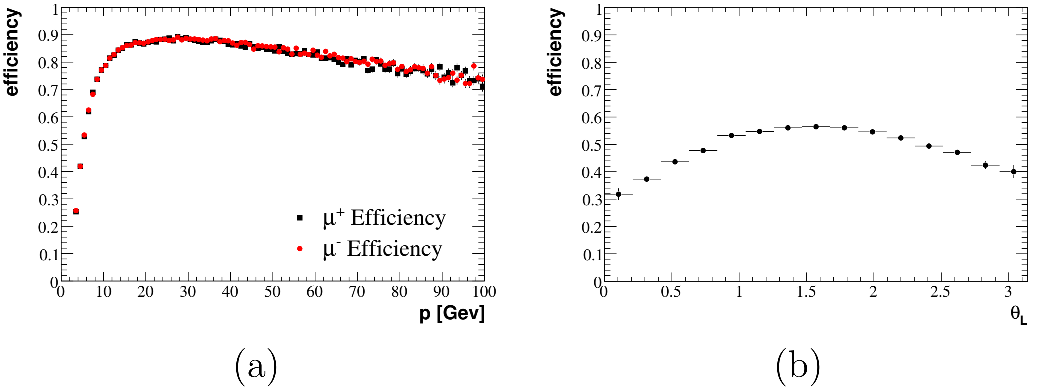

(a) (b)

Figure 7.14: Muon reconstruction efficiency (a) and the acceptance effect introduced on the lepton angle (b).

This momentum cut on each of the muons introduces a further acceptance effect on θ_L that is demonstrated in Fig. 7.14(b).

Muon Station	Momentum
Hits in M2 and M3	$3 < p < 6\,\mathrm{GeV}/c$
Hits in M2, M3 and M4 or M5	$6 < p < 10\,\mathrm{GeV}/c$
Hits in M2, M3, M4 and M5	$p > 10\,\mathrm{GeV}/c$

Table 7.5: The hard momentum cuts that are applied when reconstructing tracks as muon candidates.

Fig. 7.14(a) shows the reconstruction efficiency versus momentum for the muon reconstruction. This efficiency is greater than 70% for muons from $B_d \rightarrow K^{*0}\mu^+\mu^-$ decays with $p > 10\,\mathrm{GeV}/c$. The overall pre-selection efficiency, including the reconstruction of all four charged particles, is 12.4%. There is a small reduction in efficiency for muons pairs with low q^2 as the muons become closer together and are harder to separate. The efficiency does not fall as rapidly as $q^2 \rightarrow 0$ as it does at *BABAR* and Belle due to the large boost at the LHC.

7.10.1 Angular Resolution

The angular resolution of the reconstruction is good enough that it can be totally ignored when extracting the A_{FB}. The resolution on the three angles is given in Fig. 7.15. It is typically $< 10\,\mathrm{mrad}$ and there is no significant bias on the reconstructed angle. The resolution on θ_L is best owing to the long tracks used in the muon reconstruction.

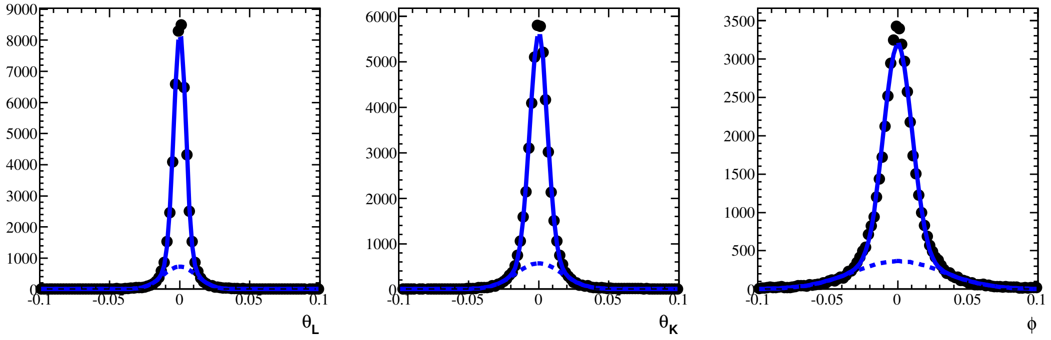

Figure 7.15: Angular resolution on the reconstruction of the three decay angles. The resolution on $\theta_L = 4.31\,\mathrm{mrad}$, $\theta_K = 6.26\,\mathrm{mrad}$ and $\phi = 10.2\,\mathrm{mrad}$. A double Gaussian has been fitted to each dataset (line). The contribution from the broader of the two Gaussians is indicated by the dashed line.

7.11 Using $B \to K^{*0}J/\psi$ as a Control Channel

Much of the previous discussion has focused on how selection cuts, the trigger and the reconstruction of particles in LHC*b* influences the measured θ_L distribution. Ideally these reconstruction efficiencies and angular acceptances would be measured in a known control channel and this data used to correct the signal distributions. For the rare decays $B_d \to K^{*0}\mu^+\mu^-$ and $B^+ \to K^+\mu^+\mu^-$ the ideal control channels would be $B \to K^{*0}J/\psi$ and $B^+ \to K^+J/\psi$. These have the same final state particles and the decays have been measured to good precision by the B Factories. They can also be reconstructed with the same selection cuts as the signal $B_d \to K^{*0}\mu^+\mu^-$ and $B^+ \to K^+\mu^+\mu^-$ decays.

The decay $B \to K^{*0}J/\psi$ goes to a vector-vector final state and is usually described in the Transversity basis [92] with three angles (θ_{tr}, ϕ_{tr} and θ_K),

$$\begin{aligned}
\frac{1}{\Gamma}\frac{d^3\Gamma}{d\cos\theta_{tr}\;d\cos\theta_K\;d\phi_{tr}} \quad = \quad & 2|A_0|^2\left(1-\sin^2\theta_{tr}\cos^2\phi_{tr}\right)\cos^2\theta_K \\
& +|A_\parallel|^2\left(1-\sin^2\theta_{tr}\sin^2\phi_{tr}\right)\sin^2\theta_K \\
& +|A_\perp|^2\sin^2\theta_K\sin^2\theta_{tr} \\
& +\Im\left(A_\parallel^* A_\perp\right)\sin^2\theta_K\sin 2\theta_{tr}\sin\phi_{tr} \\
& -\tfrac{1}{\sqrt{2}}\Re\left(A_\parallel A_0^*\right)\sin 2\theta_K\sin^2\theta_{tr}\sin\phi_{tr} \\
& -\tfrac{1}{\sqrt{2}}\Im\left(A_\perp A_0^*\right)\sin 2\theta_K\sin 2\theta_{tr}\cos\phi_{tr}
\end{aligned}$$

which differ slightly from the angles used in the $B_d \to K^{*0}\mu^+\mu^-$ angular analysis.

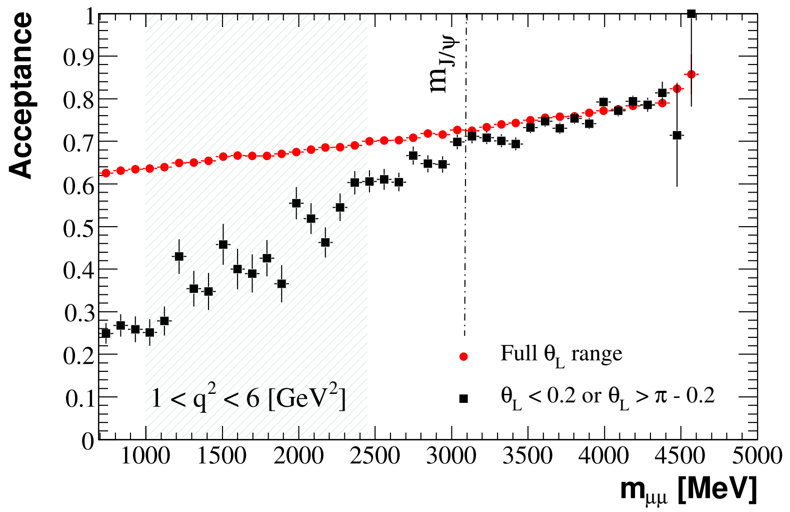

Figure 7.16: The efficiency for events to pass a $p_T > 300\,\mathrm{MeV}/c$ cut on the muons versus the dimuon invariant mass for two different angular ranges.

The two distributions do share a single, common, angle θ_K. It also uses the same K^{*0} spin amplitudes discussed above. Measurements from *BABAR* [93] are $|A_0|^2 = 0.556 \pm 0.009 \pm 0.010$, $|A_\parallel|^2 = 0.211 \pm 0.010 \pm 0.006$ and $|A_\perp|^2 = 0.233 \pm 0.010 \pm 0.005$.

Unfortunately Fig. 7.16 illustrates a major limitation in using these decays to correct the angular distribution of $B_d \to K^{*0}\mu^+\mu^-$ decays. As the invariant mass of the dimuon pair is increased the acceptance effect on θ_L is reduced and the efficiency becomes flat as a function of the angle. In Fig. 7.16 the two sets of points represent the efficiency versus the dimuon mass introduced by a p_T cut in two different bins of θ_L. One around $\frac{\pi}{2}$ and the other around 0 or π. The slope demonstrates that the cut preferentially selects high or low invariant mass muon pairs and the separation between the two sets of points results from the acceptance effect. At high masses, around the J/ψ, the two sets of points are close together and any acceptance effect negligible. In the $1 < q^2 < 6\,\mathrm{GeV}^2$ region the acceptance effect is far larger and any measurement of the angular acceptance in the control channel has little bearing.

A cleanly selected sample of $B \to K^{*0}J/\psi$ decays is still useful for determining the acceptance effects on the kaon angle. An example, in the $1 < q^2 < 6\,\mathrm{GeV}^2$ dimuon mass range, is given in Fig. 7.17. This plots the efficiency to select $B_d \to K^{*0}\mu^+\mu^-$ and $B \to K^{*0}J/\psi$ events using the full selection cuts as a function of the angle θ_K. Figure 7.17(b) shows the double ratio, of the efficiency to select $B_d \to K^{*0}\mu^+\mu^-$ events divided by the efficiency for events in the control channel. The ratio of the efficiencies is flat with θ_K.

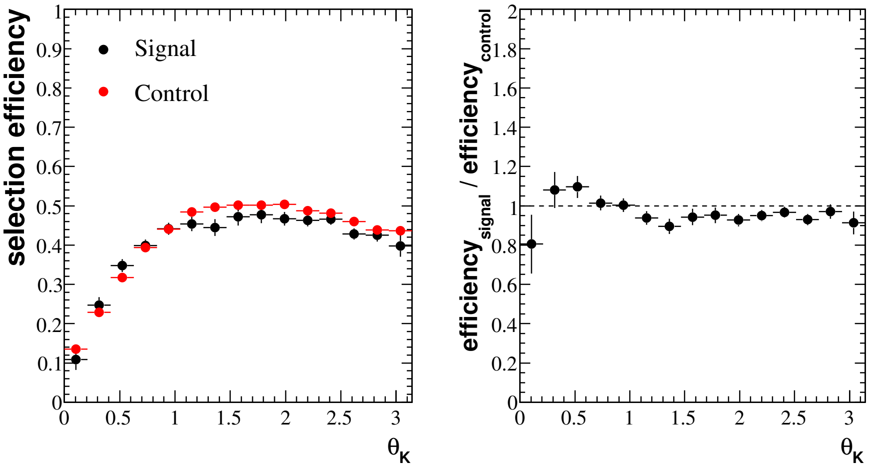

(a) (b)

Figure 7.17: The angular acceptance as a function of θ_K for $B_d \rightarrow K^{*0}\mu^+\mu^-$ signal events and for $B \rightarrow K^{*0}J/\psi$ events selected with the same selection cuts.

In Sec. 7.8 the lepton angular acceptance was symmetric about $\frac{\pi}{2}$. This is not true for the θ_K acceptance in Fig. 7.17(a). In this case the reconstructed particles are a pion and kaon and the angle θ_K is always defined with respect to the kaon. The asymmetry results from the $K^{\pm}$ and $\pi^{\pm}$ having a different momentum and p_T spectrum. Due to the difference in mass they do not take equal amounts of momentum away from the K^{*0}. In Fig. 7.18 there is a different efficiency with p or p_T to pass the selection cuts depending on the particle type. The net result is that if the kaon is in the same direction as the B, forward, with θ_K close to π the efficiency to reconstruct the $B_d \rightarrow K^{*0}\mu^+\mu^-$ events is larger.

In Fig. 7.18 the p_T spectrum is fitted with a power law, with fit parameters a_0 and a_1 ,

$$\varepsilon(p_T) = a_0 \times \left(p_T - {p_T}^{Cut}\right)^{a_1} \quad .$$

This situation is further complicated by reconstruction effects, where the efficiency to identify heavy (kaon) and light (pion) particles is different and depends on the particle's momentum. In the final experiment we may also have to take care when combining B_d and $\overline{B}_d$ events as the K^+ and K^- have different interactions with matter[2] and hence different reconstruction efficiencies.

---

[2] The K^- can produce a Λ whilst the K^+ can not.

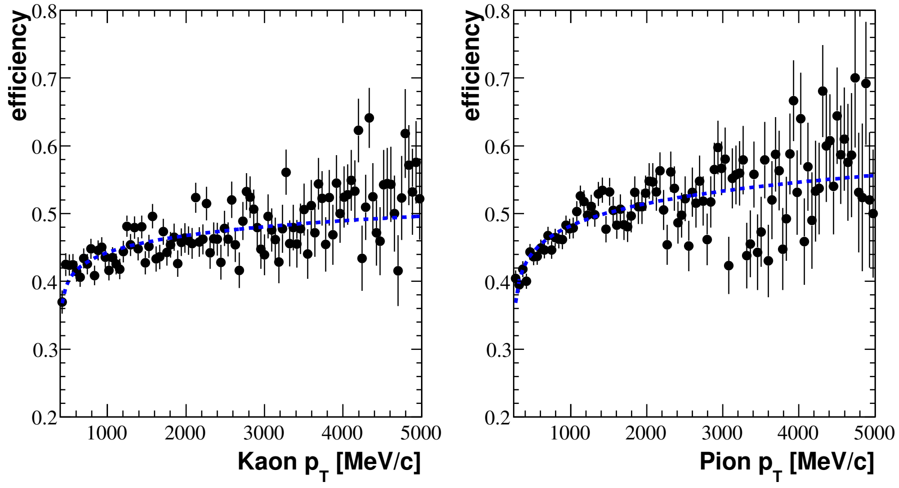

(a) (b)

Figure 7.18: The efficiency to select events based on the kaon p_T (a) and pion p_T (b).

7.12 Forward Backward Asymmetry in $B^+ \to K^+\mu^+\mu^-$ as an Observable

The A_{FB} in $B^+ \to K^+\mu^+\mu^-$ as a stand-alone observable does not look promising for new physics searches. At most the A_{FB} is expected to vary from zero by 2%. Likewise the new physics contributions to F_S are likely to remain small. This raises the prospect of using this decay not for new physics searches but rather as a handle on any systematic or acceptance effects (as the distribution should be known within the 2% uncertainty). In particular it has the useful property that the dimuon invariant mass spectrum is flat across most of the allowed range, with the exception of the $q^2 \simeq (m_B - m_K)^2$ region. It can also be selected with a very similar set of selection cuts. The selection and reconstruction of the muons leads to the same acceptance effects on θ_L. A simple example of this is provided in Fig. 7.19 using the same generator level 300 MeV/c p_T cut. Figure 7.19(a) once again shows the angular efficiency as a function of θ_L for $B_d \to K^{*0}\mu^+\mu^-$ decays. Figure 7.19(b) is the corresponding efficiency in $B^+ \to K^+\mu^+\mu^-$ and (c) is the double ratio of the efficiencies.

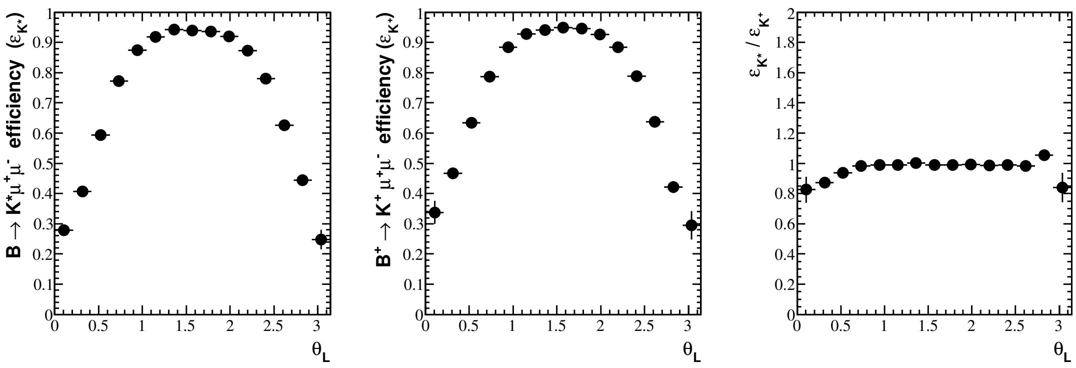

(a) (b) (c)

Figure 7.19: The acceptance effect on θ_L introduced by a 300 MeV/c p_T cut on the muons in the decays $B_d \to K^{*0}\mu^+\mu^-$ (a) and $B^+ \to K^+\mu^+\mu^-$ (b) and the double ratio (c).

7.13 Momentum Dependent Effects on the Forward Backward Asymmetry

The $B_d \to K^{*0}\mu^+\mu^-$ decays are self-tagging and the flavour of the b is identified by the charge of the kaon from the K^*. There are few miss-tagged B_d or $\overline{B}_d$ candidates because the probability to miss-identify both the pion and kaon is small due to the performance of the RICH detectors. The number of events where either a combinatorial kaon is picked up and combined with the genuine pion or the pion from the K^* is miss-identified as a kaon and a combinatorial pion picked up is also small. In the angular analysis lepton and kaon angles for the B_d and $\overline{B}_d$ decays are combined by defining θ_L with respect to μ^+ for the B_d and the μ^- for the $\overline{B}_d$. This naturally follows from the description of the decay. Any effect that creates a difference between the μ^+ and μ^- and biases the individual distribution is cancelled. If the lepton angle distribution is treated separately for B_d or $\overline{B}_d$ events, then it is possible to introduce large changes to the A_{FB} distribution. These large shifts will be equal and opposite for the B_d and $\overline{B}_d$ distributions. A symmetrical acceptance effect will reduce the size of the forward backward asymmetry but not increase it.

An example effect that could lead to large shifts in the measured A_{FB} is a momentum and charge dependent efficiency, treating the μ^+ and μ^- differently. In the following example the μ^+ has an exponential momentum dependent efficiency, see Fig. 7.20. This results in an A_{FB} that is systematically shifted across all values of q^2. This shift for the B_d decay is to a more backward distribution, as depicted in Fig. 7.21(b). For the $\overline{B}_d$ the shift is to a more forward distribution. The shift in the A_{FB} can be explained with reference to Fig. 7.22. The momentum of the backward

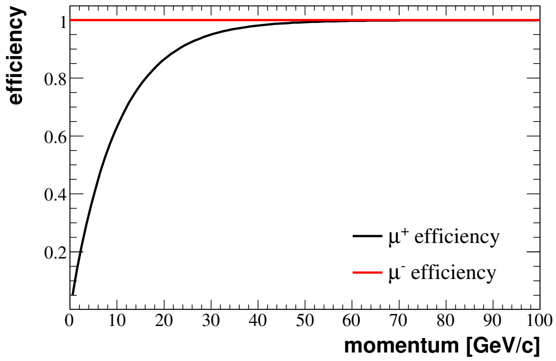

Figure 7.20: An artificial momentum and charge dependent efficiency that has been introduced at generator level.

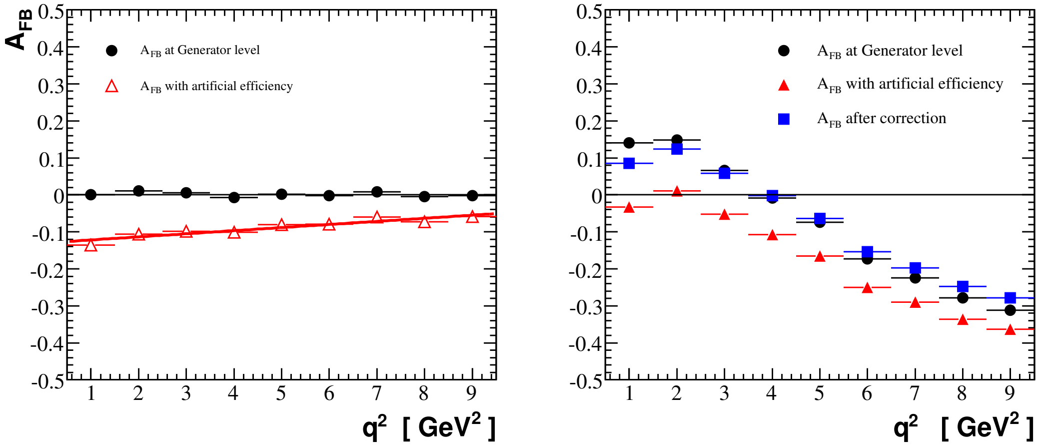

Figure 7.21: The A_{FB} in B^+ and B_d decays at generator level before and after an artificial charge and momentum dependent efficiency is applied. A straight line fit to the A_{FB} in $B^+ \to K^+\mu^+\mu^-$ has been used to correct the right-hand plot showing the A_{FB} in $B_d \to K\mu^+\mu^-$.

going μ^+ in $B_d \to K^{*0}\mu^+\mu^-$ decays tends to be higher than that of the forward μ^+ and so more forward than backward events are lost. This effect is particularly related to the momentum component along the axis of the detector.

A similar shift in the A_{FB}, away from $A_{FB} = 0$, is seen when applying the artificial efficiency to $B^+ \to K^+\mu^+\mu^-$ decays. In this case the shift is to an unphysical value. The $B^+ \to K^+\mu^+\mu^-$ decay is also self-tagging through the $K^\pm$. In Fig. 7.21 a linear fit to the A_{FB} in $B^+ \to K^+\mu^+\mu^-$ has been used to correct the A_{FB} in $B_d \to K^{*0}\mu^+\mu^-$ back towards the true value.

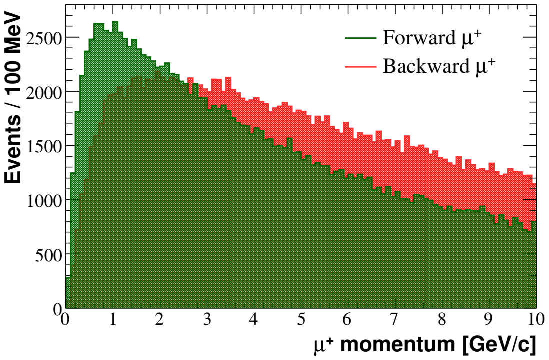

Figure 7.22: The momentum distribution of forward and backward going μ^+ in $B_d \rightarrow K^{*0}\mu^+\mu^-$ decays (not including $\overline{B}_d$ decays).

7.14 Summary

This chapter illustrates LHC*b*'s performance in reconstructing, selecting and triggering on $B_d \rightarrow K^{*0}\mu^+\mu^-$ candidates in the LHC*b* MC. The MC simulation provides a description of the material in the detector and simulation of the front-end electronics necessary to carry out a somewhat realistic study of LHC*b*'s capability to make measurements of this rare FCNC decay. The study indicates that LHC*b* will expect to select 4,600 genuine and 14,500 fake candidates in a single year of data taking. It should be stressed that these numbers are achieved by applying a set of cuts optimised on an earlier simulation. The performance is expected to return to a figure closer to the 7,000 genuine signal candidates and 3,500 background candidates when the selection cuts are re-optimised (for DC06).

MC studies on a sample of $B_d \rightarrow K^{*0}\mu^+\mu^-$ decays highlight several potential difficulties in making a precision measurement of the forward-backward asymmetry. In particular there are angular acceptances in θ_L and θ_K. These are reconstruction or selection efficiencies that bias the measured angular distributions. The acceptance in θ_L is symmetric about $\theta_L = \frac{\pi}{2}$. This is far from true for θ_K owing to the different treatment of pions and kaons in the reconstruction and selection.

The numbers presented in this chapter are used throughout Chapter 8 in a toy MC study to investigate the precision LHC*b* can achieve on the zero crossing point of the A_{FB} with a nominal year of data taking.

Chapter 8

Sensitivity to the Forward-Backward Asymmetry in $B_d \to K^{*0}\mu^+\mu^-$

In Chapter 7 the elements needed to study LHCb's sensitivity to the forward-backward asymmetry A_{FB} and its zero-crossing point in the decay $B_d \to K^{*0}\mu^+\mu^-$ were brought together. The sensitivity analysis will be discussed in this chapter, focusing on measurements with the first nominal year of data ($2\,\mathrm{fb}^{-1}$ at $L = 2 \times 10^{32}\,\mathrm{cm}^{-2}\mathrm{s}^{-1}$) at LHC$b$. The important ingredients are:

- an estimate for the number of signal and background events. This is approximately 7000 $B_d \to K^{*0}\mu^+\mu^-$ events with a signal-to-background ratio, in a tight $\pm 50\,\mathrm{MeV}$ mass window, of two-to-one.
- the signal and background B mass, θ_L and θ_K distributions.
- the signal acceptance.

The signal acceptance was discussed in some detail in the previous chapter. It refers to an angular efficiency that is introduced by the reconstruction, the trigger or the "selection" (any bias introduced by applying the event selection) that is not flat in either θ_L or θ_K. The geometrical acceptance of the detector is not a problem. This is demonstrated in Fig. 8.1. In the sensitivity study only the effect introduced by a non-uniform acceptance on θ_L are considered. It is assumed that the acceptance on θ_K can be measured independently in the high-statistic $B \to K^{*0}J/\psi$ control

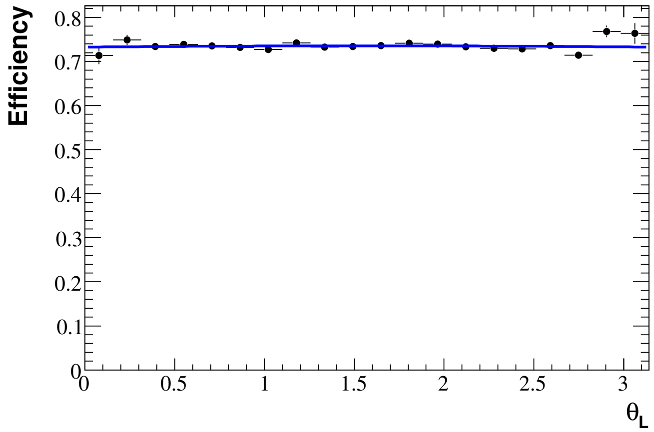

Figure 8.1: The relative efficiency, as a function of θ_L, introduced when requiring the daughter particles from the $B_d \to K^{*0}\mu^+\mu^-$ decay to fall within the 400 mrad geometrical acceptance of the LHCb detector.

channel. No mention was made in the previous chapter of angular acceptances on ϕ. There is no acceptance effect seen in this angle and the efficiency remains flat independent of the cuts.

8.1 Angular Distributions and Forward-Backward Asymmetry

There are a number of different ways to measure the forward-backward asymmetry in the $B_d \to K^{*0}\mu^+\mu^-$ angular distribution. The simplest is to perform a counting experiment, counting the number of forward going μ^+ (or μ^-) compared to the number of backward going μ^+ (μ^-). Where,

$$A_{FB} = \frac{N_F - N_B}{N_F + N_B}$$

and the number of forward N_F and backward N_B going μ^+ or μ^- can be written in terms of θ_L as

$$N_F\left(q^2\right) = \int_0^1 \frac{d^2\Gamma}{dq^2\ d\cos\theta_L} d\cos\theta_L \quad , \quad N_B\left(q^2\right) = \int_{-1}^0 \frac{d^2\Gamma}{dq^2\ d\cos\theta_L} d\cos\theta_L$$

If the tight mass window contains a sizeable background contribution it will need to be subtracted. This can either be done by performing a sideband subtraction before carrying out the counting experiment or directly from the measured A_{FB} by,

$$A_{FB}^{signal} = \frac{N_F^{sig.+bkg.} - N_B^{sig.+bkg.} - A_{FB}^{sidebands} \times \widetilde{n}_B}{N_F^{sig.+bkg.} + N_B^{sig.+bkg.} - \widetilde{n}_B}$$

where $\widetilde{n}_B$ is the estimate for the number of background events in the tight mass window, achieved by fitting the mass distributions. If the background is symmetric about $\theta_L = \frac{\pi}{2}$ and it is not subtracted as described above it will dilute the measured A_{FB} in each bin of q^2. If it is asymmetrical, which may be expected if there is a significant number of cascade $b \to c(\to \mu)\mu$ decays, then it will bias the measured A_{FB}.

The second approach is to measure the A_{FB} in a fit to the projection of the lepton angle, achieved by integrating out the angles θ_K and ϕ in the full distribution. This projection contains information on both the fraction of longitudinally polarised K^*'s (F_L) and A_{FB}. This technique has a number of benefits over the simple counting experiment. In particular the shape of the distribution holds information on A_{FB}, which can be used to improve the measurement. This approach is the focus of much of this chapter.

The final approach is to perform a full angular fit, fitting for the transversity amplitudes rather than the observables of F_L and A_{FB}. This approach will be very challenging with early data. It is discussed in more detail in Sec. 8.5 and will be more useful for larger data sets as it provides the greatest sensitivity to A_{FB} through correlations in the angular distribution. The full fit also allows access to a number of theoretically clean observables that are lost when making the projections.

8.1.1 Acceptance Effects

Figure 8.2 plots the relative significance, in the context of a measurement of A_{FB}, of seeing an excess or deficit of 'N' events at an angle θ_L (for $A_{FB} = \pm 0.1$). This neatly describes why the acceptance effects introduced in the previous chapter can bias a measurement of the A_{FB}. Around $\theta_L = \frac{\pi}{2}$ there is little-to-no sensitivity to the A_{FB} as the increase or decrease in events is small compared to the total number of events. As θ_L gets close to zero or π the sensitivity is small due to the small number of events. The sensitivity is greatest around $\theta_L = 0.2$ or $\theta_L = \pi - 0.2$. Unfortunately these events sit in a region where the effect of the acceptance is large and the efficiency to reconstruct and select these events is low. The number of both

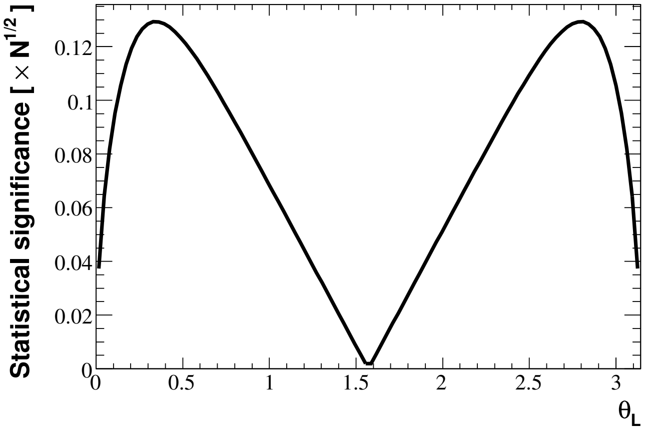

Figure 8.2: The statistical significance of a bin in θ_L for measuring a forward backward asymmetry with $A_{FB} = \pm 0.1$. Defined as the significance $(\Delta N_{AFB}/\sqrt{N})$ of an increase (or decrease) of ΔN_{AFB} events in a bin containing N events centred on θ_L due to the forward-backward asymmetry.

forward and backward events is reduced and so is the size of the A_{FB}. This has the largest impact on the measured A_{FB} if the A_{FB} is estimated by simply counting forward and backward events but will also bias the lepton angle distribution. The distorted shape of the distribution can bias both the estimates of A_{FB} and F_L achieved by fitting the angular distributions.

The reconstruction and selection efficiencies that bias the measured θ_L angle are combined in Fig. 8.3 to provide an estimate for the total acceptance on θ_L in a q^2 bin $1 < q^2 < 3\,\mathrm{GeV}^2$. The line represents a parabolic fit to the distribution,

$$A(q^2, \theta_L) = a_0 \left[1 - a_1 \left(\theta_L - \frac{\pi}{2} \right)^2 \right] \quad .$$

The fitted parameters are $a_0 = 0.063 \pm 0.002$ and $a_1 = 0.48 \pm 0.02\,\mathrm{radians}^{-2}$. Parameter a_0 determines the overall efficiency for reconstructing and selecting the $B_d \rightarrow K^{*0}\mu^+\mu^-$ events as described in Chapter 7. This normalisation is irrelevant for the sensitivity study. It can be neglected because the purpose of the study is not to make a measurement of the branching fraction or a measurement of the dimuon invariant mass distribution in the decay. These measurements have little sensitivity to new physics and it is unlikely that a measurement at LHC*b* will be competitive with the existing measurements from *BABAR* and Belle.

Traditionally angular analyses take the parametrised acceptance directly from their MC simulations. For the first year of data taking it is unlikely that the LHC*b*

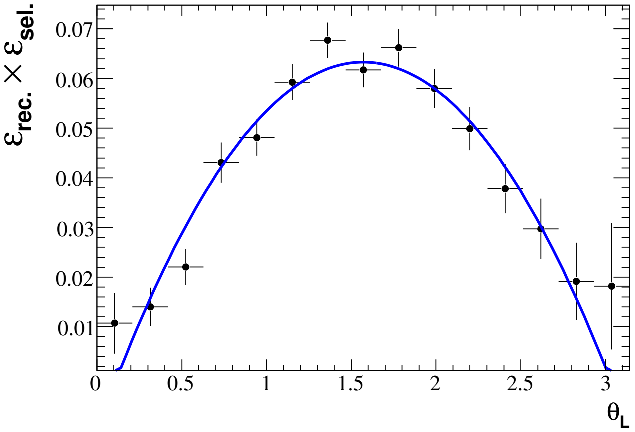

Figure 8.3: The combined acceptance effect resulting from the reconstruction and the selection in a bin $1 < q^2 < 3\,\mathrm{GeV}^2$.

q^2 [GeV^2]	a_1 [radians^{-2}]
$1 < q^2 < 2$	0.5
$2 < q^2 < 3$	0.4
$3 < q^2 < 4$	0.3
$4 < q^2 < 5$	0.2
$5 < q^2 < 6$	0.1

Table 8.1: The parametrised acceptance $A\left(\theta_L, q^2\right) = 1 - a_1\left(\theta_L - \frac{\pi}{2}\right)^2$, used in each q^2 bin of the sensitivity study.

MC simulation will be sufficiently verified to use with confidence for this measurement and the acceptance on θ_L will instead have to be estimated from the data. These numbers may eventually be taken from the MC if it can be shown that the MC description of the B_d's, for example their η and momentum distribution, agree with the data. This approach is valid only because the acceptance is dominated by kinematic cuts in the selection and reconstruction.

The θ_L acceptance has a strong dependence on the dimuon invariant mass, becoming flatter at increasing q^2. The values in Table 8.1 are the acceptance values used in each of the q^2 bins of this study. These are similar in size and shape to the acceptances in the full LHCb simulation but have been chosen somewhat arbitrarily to demonstrate the feasibility of the measurement and highlight the potential bias to the zero crossing point.

8.2 Simulating Events for the Sensitivity Study

The sensitivity study is carried out in a combination of RooFit [94] and stand-alone code, generating 1000 toy Monte Carlo experiments. The study uses five equal-size bins in q^2 in the range $1 < q^2 < 6\,\mathrm{GeV}^2$ with a nominal year of data in each q^2 bin. The number of expected events is calculated from the average annual yield and distributed in q^2 according to Fig. 7.6. The binning is discussed in more detail in Sec. 8.2.1. In each bin of q^2 the average values for A_{FB} and F_L in the Standard Model are used to generate the θ_L and θ_K projections and the θ_L distribution is folded with the acceptance effect parametrised in Table 8.1. The signal mass distribution is Gaussian with a width of 18 MeV (fixed according to the expected precision from the full simulation).

Background events are generated over the wide mass window with an exponential mass dependence, as specified in Sec. 7.6.2. The angular distribution of the background is parametrised, again from Sec. 7.6.2, in terms of a polynomial for both θ_L and θ_K. The coefficients for this parametrisation take different values above, inside and below the tight mass window. There is no q^2 dependence to the simulated background and the correct parametrisation is chosen depending solely on the mass. The signal-to-background ratio has been normalised so that it is two-to-one in the tight mass window.

8.2.1 Binning the Data

In the Standard Model the q^2 distribution peaks as $q^2 \to 0$ around the photon pole and at the $c\bar{c}$ resonances. Many of the new physics models have similar q^2 distributions. Care needs to be taken to keep the analysis model independent and to avoid picking a set of bin sizes that optimises the sensitivity to one model but is less suitable for the others. The choice of binning also relies on the background distribution in q^2 which is difficult to estimate due to the small number of events that remain after the full selection cuts are applied. This will introduce a source of systematic error that will need to be studied in data. Eventually the goal will be to perform an unbinned fit in all variables.

The choice of equal bin sizes in this study leads to a similar number of events remaining in each of the bins after selection cuts (assuming a SM q^2 distribution). This ranges from 4.7 to 5.5% with an 0.2% statistical error. The choice of five bins of q^2 is a trade-off between increasing the statistics in each bin whilst minimising the size of the bins. Ideally the bin size would be kept small so that the variations in the observables and transversity amplitudes are negligible over the bin width.

8.3 Estimating the A_{FB} in the Sensitivity Study

The strategy to measure the A_{FB} in the sensitivity study is to:

- estimate the signal and background contributions in the tight mass window by fitting the signal and background mass distributions over the wide mass window.
- perform a background subtraction to estimate the angular distribution of the signal.
- fit the angular projections to estimate A_{FB} and F_L.

The angular acceptance $A\left(q^2, \theta_L\right)$ on θ_L is included in the fit, by fitting to

$$A\left(q^2, \theta_L\right) \times \frac{1}{\Gamma}\frac{d^2\Gamma}{d\theta_L\ dq^2} \quad \text{and} \quad \frac{1}{\Gamma}\frac{d^2\Gamma}{d\theta_K\ dq^2}$$

where,

$$\frac{1}{\Gamma}\frac{d^2\Gamma}{dq^2\ dx_L} = \frac{3}{8}\left(1+F_L\right)\left(1-x_L^2\right) + A_{FB}x_L$$

$$\frac{1}{\Gamma}\frac{d^2\Gamma}{dq^2\ dx_K} = \frac{3}{4}\left(1-F_L\right) + \left(3F_L-1\right)x_K^2$$

and the parameters $x_L = \cos\theta_L$ and $x_K = \cos\theta_K$. Were it not for the acceptance effects it would be suitable to fit in terms of x_L and x_K rather then the angles.

The two fits are performed simultaneously using information on F_L from the θ_K distribution to improve the fit to the θ_L distribution. An added benefit of this approach is that this removes the large correlation between the acceptance and F_L that exists if the two angular distributions are fitted independently. The acceptance is treated as parabolic and is described by a single parameter. In the real experiment

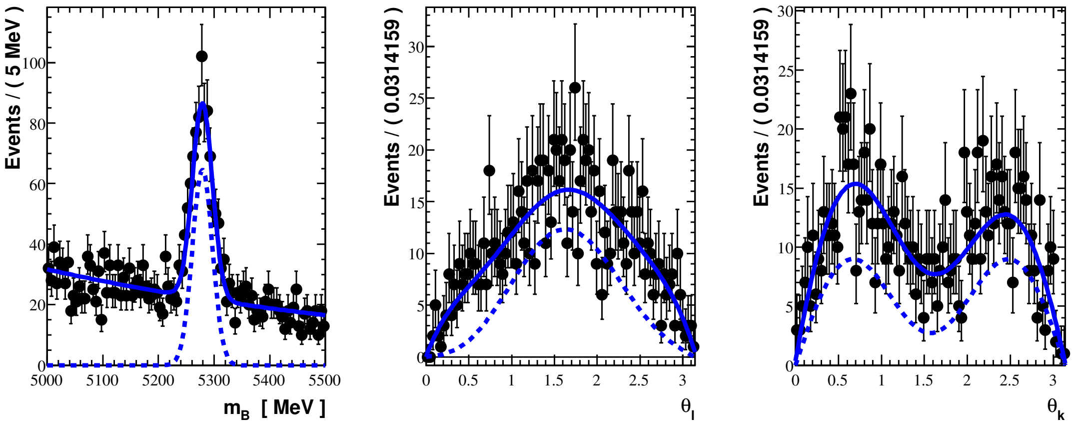

Figure 8.4: Example of the combined signal plus background distributions in m_B, θ_L and θ_K. The θ_L and θ_K distributions cover only the tight mass window. The solid line is the combined data set, the dashed curve the signal contribution and the points an example toy experiment.

the acceptance effect on the angle θ_K will be measured in $B \to K^{*0}J/\psi$ decays. It is likely that any contribution to the error on A_{FB} caused by having to correct the $B_d \to K^{*0}\mu^+\mu^-$ θ_K distribution will be insignificant compared to the other sources of error.

An example of the combined signal and background B mass, θ_L and θ_K distributions is shown in Fig. 8.4. The results of the angular fitting are presented in Sec. 8.4.

8.3.1 Background Subtraction

The background subtraction is performed using an upper ($5079 < m_B < 5179\,\mathrm{MeV}$) and lower ($5329 < m_B < 5379\,\mathrm{MeV}$) sideband in fifteen bins of θ_L and θ_K. The background distribution under the signal is then estimated by interpolating in each bin of θ_L and θ_K between the upper and lower sidebands. It is then weighted to agree with the number of events from the fit to the mass distributions and subtracted from the combined θ_L distribution for the signal and background in the tight mass window. The fit to the background subtracted distribution is a binned least-χ^2 fit over the bins in θ_L and θ_K minimising,

$$\chi^2 = \sum_{i=0}^{15} \frac{(N_i - f(\theta_L, \vec{a}))^2}{N_i} + \sum_{j=0}^{15} \frac{(N_j - f(\theta_K, \vec{a}))^2}{N_j}$$

where $N_{\theta_{L,K}}$ are the number of events in each bin of θ_L or θ_K after the background

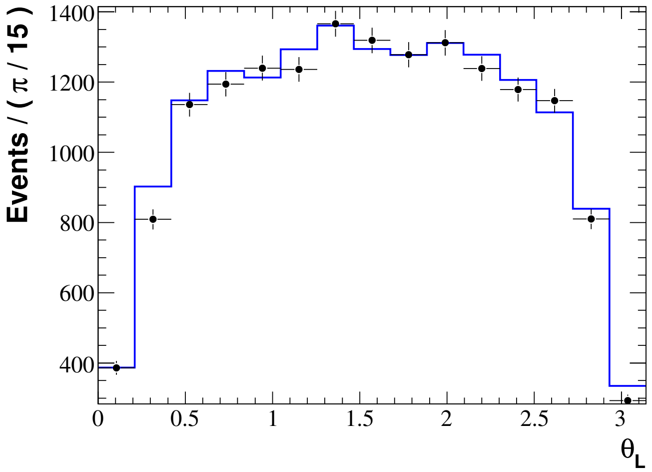

Figure 8.5: The distribution in θ_L of candidates from the $bb \to \mu\mu$ background sample for $4m_l^2 < q^2 < (m_B - m_{K\pi})^2$ in a mass window $m_B \pm 50\,\mathrm{MeV}/c^2$ (*points*) and the estimated background in this signal region using an upper and a lower sideband and performing a sideband subtraction (*line*).

subtraction and $f(\theta_{L,K}, \vec{a})$ is the fitted angular distribution with parameters $\vec{a} = (A_{FB}, F_L, a_1)$.

This background subtraction method has been validated on the loosely selected Monte Carlo sample described in Chapter 7. The points in Fig. 8.5 represent the distribution of background events in the tight-mass window using the full Monte Carlo sample and the line is the estimate from the sidebands for the background in the same window. It is clear that the two distributions are in good agreement. A Kolmogorov-Smirnov test[1] of the distributions estimates the agreement at 96%. In the data the systematic impact of the sideband subtraction can be studied by comparing the predicted background distribution from a number of different sidebands. In this example the background estimate comes from interpolating between an upper and lower sideband but a similar estimate can be made with a different choice of sidebands. For example, by extrapolating from two lower sidebands or by interpolating between three or more sidebands. Each background estimate will be sensitive to a different combination of potential backgrounds (for example, more or less low mass background).

---

[1] The Kolmogorov-Smirnov test is a goodness of fit test, designed to test the compatibility of two distributions. A description of the test can be found, for example, in reference [95].

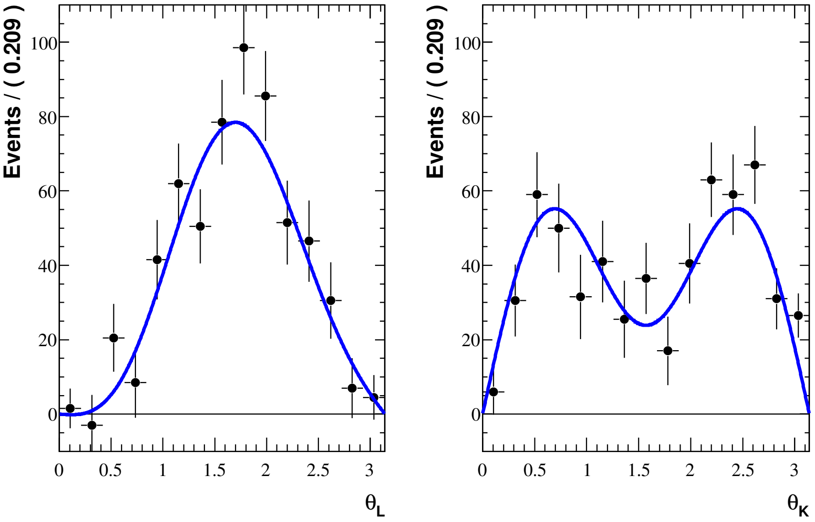

Figure 8.6: An example of the sideband subtracted $2\,\mathrm{fb}^{-1}$ signal distribution in a q^2 bin $5 < q^2 < 6\,\mathrm{GeV}^2$ for θ_L and θ_K. The lines are a fit to the distributions.

8.4 Results from the Fitting

Fig. 8.6 demonstrates typical θ_L and θ_K distributions that remain after the background subtraction of a $2\,\mathrm{fb}^{-1}$ data set. These are now much closer to the true θ_L and θ_K distributions in this bin of q^2 (the dashed lines in Fig. 8.4). The characteristic dip in the θ_K distribution is proportional to F_L and the left-right asymmetry of the θ_L distribution to A_{FB}.

The sensitivity study has been carried out a number of times turning on or off the background contamination and the acceptance effects. The key results are presented in Tables 8.2 and 8.3 and Figures 8.7 and 8.9. There are five different scenarios:

- **A** - The toy MC data is generated according to the $B_d \to K^{*0}\mu^+\mu^-$ angular distribution with no background and no signal acceptance. There is no background subtraction and the fit does not include the acceptance.
- **B** - The toy MC data is generated using the $B_d \to K^{*0}\mu^+\mu^-$ angular distribution folded with the acceptance. There is no background in the generation, no background subtraction and the fit does not include the acceptance.
- **C** - The toy MC data is generated using the $B_d \to K^{*0}\mu^+\mu^-$ angular distribution folded with the acceptance. There is no background in the generation and no background subtraction. The lepton acceptance is included in the fit.

	A_{FB} (fitted)	A_{FB} (counting)	F_L
A	0.16 ± 0.04	0.16 ± 0.06	0.76 ± 0.04
B	0.15 ± 0.05	0.12 ± 0.06	0.82 ± 0.03
C	0.160 ± 0.06	–	0.75 ± 0.04
D	0.159 ± 0.06	–	0.76 ± 0.05
E	0.153 ± 0.09	–	0.77 ± 0.05

Table 8.2: Sensitivity to the Standard Model A_{FB} in the bin of q^2 with the largest acceptance effect ($1 < q^2 < 2\,\mathrm{GeV}^2$). The five different analyses A–E are defined in the text.

- **D** - The toy MC data is generated with no acceptance but now includes background. The background is subtracted.
- **E** - The toy MC data is generated with background contamination and signal acceptance. The background is subtracted and the acceptance is included in the fit.

Table 8.2 details the sensitivity to the A_{FB} in the q^2 bin with the largest acceptance effect. This is $1 < q^2 < 2\,\mathrm{GeV}^2$ and also happens to be the bin with the largest A_{FB}. The sensitivity is estimated by performing 1000 toy experiments and fitting the lepton and kaon angle distributions to obtain A_{FB} and F_L. The estimate from counting the events either side of $\theta_L = \frac{\pi}{2}$ is also included in Table 8.2 for scenarios A and B. The quoted numbers are the mean and Gaussian sigma of the 1000 experiments.

When the acceptance is introduced into the simulation the mean from the counting experiment is significantly biased from $A_{FB} = 0.16$ to $A_{FB} = 0.12$ (A → B). The impact on the fitted A_{FB} is less pronounced, even when fit does not include the acceptance model (scenario B). In this case there is however a significant bias in the measured value of F_L. With no acceptance effect or background in the simulation the fitted value is $F_L = 0.76 \pm .04$. Turning on the acceptance in the simulated events but not including it in the fit to the angular distributions shifts F_L to 0.82 ± 0.03. Fitting simultaneously for A_{FB}, F_L and the acceptance (scenario C) results in an unbiased estimate for both A_{FB} and F_L. There is also very little bias in A_{FB} and F_L when performing the full background subtraction and fitting with the acceptance model in scenario E ($F_L = 0.77 \pm 0.05$). The small shift in the central values is not statistically significant. The sensitivity to the A_{FB} and F_L in all five bins of q^2 is indicated in Fig. 8.7 and 8.8. In Fig. 8.8 the Standard Model prediction for F_L has been included for reference.

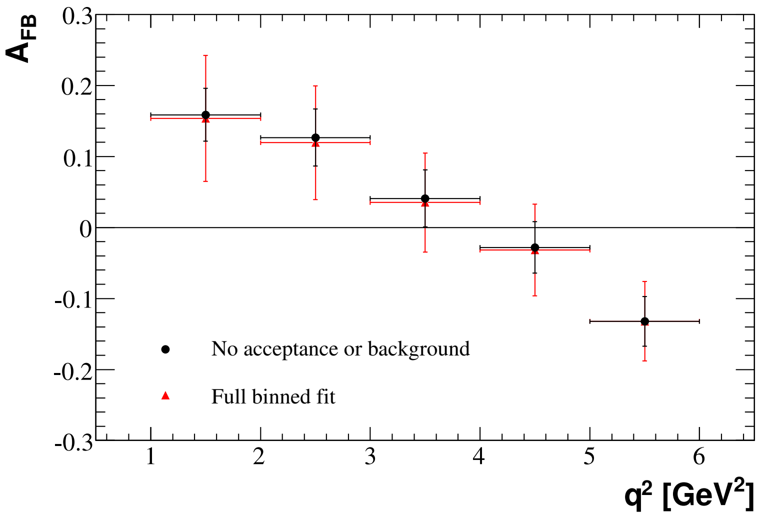

Figure 8.7: The sensitivity to the Standard Model A_{FB} in bins of q^2 in an unbinned fit with no background or acceptance (scenario A) and in the full binned fit (scenario E).

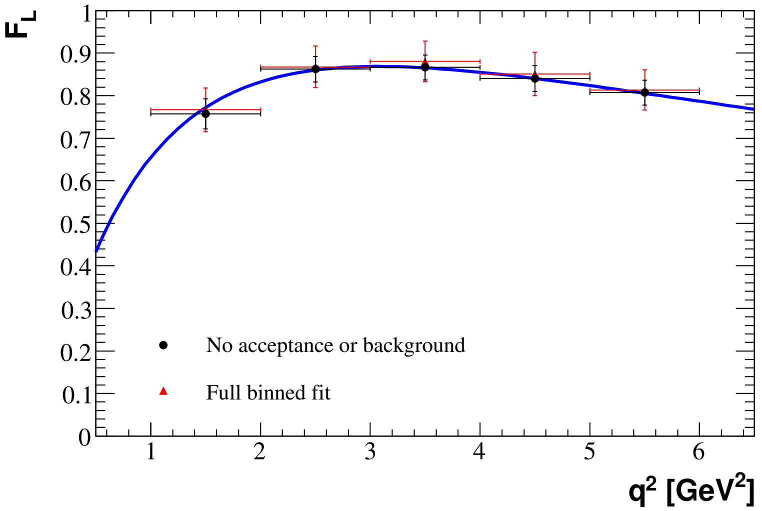

Figure 8.8: The sensitivity to a measurement of F_L in an unbinned fit to the angular distributions with no acceptance or background contamination (scenario A) and in a binned fit subtracting the background and fitting for the angular acceptance (scenario E). The line is the Standard Model prediction for F_L.

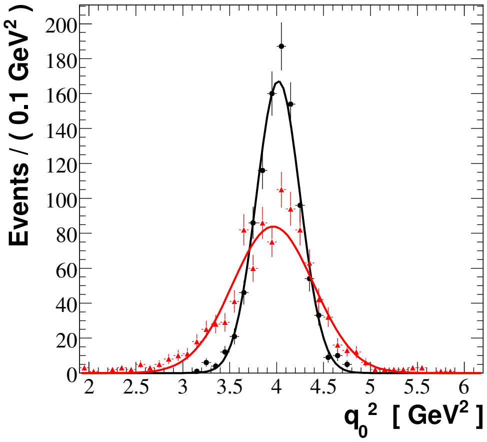

Figure 8.9: The estimated zero crossing point in 1000 MC simulations with no background and acceptance (scenario A) and in a binned background subtraction, fitting for the acceptance (scenario E).

	q_0^2 [GeV^2] (fitted)	q_0^2 [GeV^2] (counting)
A	4.02 ± 0.23	4.00 ± 0.37
B	4.00 ± 0.26	3.92 ± 0.40
C	4.00 ± 0.25	–
D	3.99 ± 0.37	–
E	3.96 ± 0.43	–

Table 8.3: Sensitivity to the zero-crossing point, q_0^2, in 1000 toy experiments.

The effect of the angular acceptance on θ_L is to reduce the measured size of A_{FB} in each bin of q^2. This reduction in A_{FB} is proportional to the size of A_{FB} and so leaves the zero-crossing point where $A_{FB} = 0$ unchanged. In practise the zero-crossing point q_0^2 is estimated by fitting the reconstructed A_{FB} in the five q^2 bins and this can lead to q_0^2 being underestimated by a small amount owing to the q^2 dependence of the acceptance. The underestimate of the A_{FB} is larger at smaller values of q^2 than larger ones. This is demonstrated in Table 8.3, which details the estimated zero-crossing point formed by fitting a straight line between the 2 to 6 GeV^2 q^2 bins. The estimates for q_0^2, from the 1000 experiments, are distributed as a Gaussian with a mean around the Standard Model expectation of $q^2 = 4\,\mathrm{GeV}^2$. The distribution of q_0^2 in the simplest scenario (A), where there is no background contamination and no signal acceptance, and the full fit (scenario E) are shown in Fig. 8.9.

8.5 Towards a Full Angular Fit

The next step would be to look at performing a full angular fit of the three angles (in bins of q^2). This could potentially be done unbinned in q^2 but would add even more complexity to the fit. The unbinned angular fit enables a better measurement of A_{FB} and provides access to new physics observables through correlations in the three dimensional distribution. It is a measurement of the real and imaginary components of the transversity amplitudes (that contain the Wilson coefficients) directly. There are two important complications. Firstly, this requires a model for the three dimensional acceptance functions for the three angles including correlations between them. It would introduce no new problems if it could be assumed that the total acceptance could be factorised as,

$$\varepsilon(\theta_L, \theta_K, \phi) = \varepsilon(\theta_L) \times \varepsilon(\theta_K) \times \varepsilon(\phi) \quad .$$

This is equivalent to the assuming that the muon spectrum doesn't effect the kaon or the pion and vice versa. It has been noted earlier that there should be no acceptance effect on the angle ϕ. If this is true then once again the θ_K acceptance can be extracted from the control channel independently of the θ_L acceptance and the remaining θ_L acceptance included in the fit as before. The efficiency is also q^2 dependent and this will have to be taken into account in a fully unbinned fit.

The second problem is that a full angular fit will require a description of the background in all of the variables. With the full selection cuts applied it is unlikely that there will be enough background events to usefully estimate the background distribution in the three angles under the signal region by performing a background subtraction as before. Whilst LHC*b* may trust its MC to make a measurement of the signal acceptance it is highly unlikely that the MC will ever be useful for estimating the background distributions. Fitting the signal and background distributions over the full mass window will also be problematic. There are already nine free parameters (in each bin of q^2) for the signal that come from the the six complex transversity amplitudes ($A_0^{L,R}$, $A_\parallel^{L,R}$ and $A_\perp^{L,R}$) and three constraints coming from the arbitrary phases. Added to this, the background would have to be described in at least four dimensions (the three angles and the B mass) including correlations between the angles for some of the sources of background.

In numerous angular analyses at the B-Factories, including the $B \to K^{*0} J/\psi$ analysis at *BABAR* [93], they adopt a different approach to background subtraction that is discussed for $B_d \to K^{*0}\mu^+\mu^-$ below.

The data or MC data set is fitted with an unbinned pseudo log-likelihood in the wide mass window, minimising

$$-2\left(\sum_{i=1}^{N_S} \ln\left(P(\vec{x}_i,\vec{a})\right) - \frac{\widetilde{n}_B}{N_B}\sum_{j=1}^{N_B} \ln\left(P(\vec{x}_j,\vec{a})\right)\right)$$

$P(\vec{x}_j,\vec{a})$ is the probability to get a hit at $\vec{x}$ in the possible phase space given an underlying description of the signal with parameters $\vec{a}$. N_S is the total number of events in the signal (tight-mass) window, N_B is the number of events in the sidebands and $\widetilde{n}_B$ is an estimator for the number of background events under the signal. This is equivalent to fitting the signal and background distribution with a description of the signal and asking how much worse the likelihood is because of the background pollution. The estimate for the difference is taken from the sidebands and is valid only if the average over the sidebands fairly represents the background under the signal. $\widetilde{n}_B$ is calculated by fitting an exponential background plus Gaussian signal distribution to the full mass window and integrating the exponential distribution under the signal peak.

As a proof of principle the two dimensional θ_L and θ_K distributions have been fitted along with the background distribution described earlier. The acceptance has been ignored. If the two-dimensional distribution is correctly normalised, by $A_0^2 + A_\parallel^2 + A_\perp^2 = \Gamma(q^2)$, then the distribution is described by two variables, effectively F_L and A_{FB}. The results of the fitting and simulation are shown in Fig. 8.10. The left-hand plot demonstates the precision in each of the five bins of q^2 on A_{FB} and the right-hand plot the expected precision on the zero crossing point.

One of the problems with this technique is that the errors from the covariance matrix are an underestimate of the real error on the fitted value. This is demonstrated in Fig. 8.11. The distributions of the pull on the fitted A_{FB} and F_L has widths of 1.43 ± 0.02 and 1.32 ± 0.02 respectively and indicates that the error on A_{FB} has been underestimated by 30% and on F_L by 24%. Furthermore, there is a bias on the measured value of A_{FB} and F_L of -0.18 ± 0.02 and -0.17 ± 0.02. These lead the zero crossing point to be slightly underestimated at $q_0^2 = 3.90 \pm 0.40$. The errors could be corrected using information from the sidebands.

In short this technique performs worse at LHCb than at the B-Factories. This is mostly due to a reduction in S/B compared to the clean sample of events used for similar analyses at the B Factories.

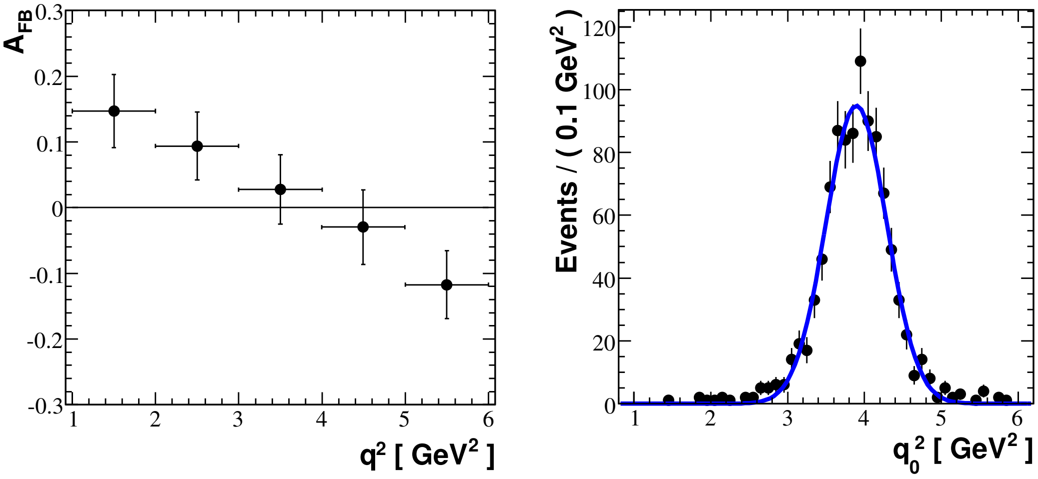

Figure 8.10: The fitted forward backward asymmetry and zero crossing point in 1000 toy experiments using a pseudo log-likelihood fit.

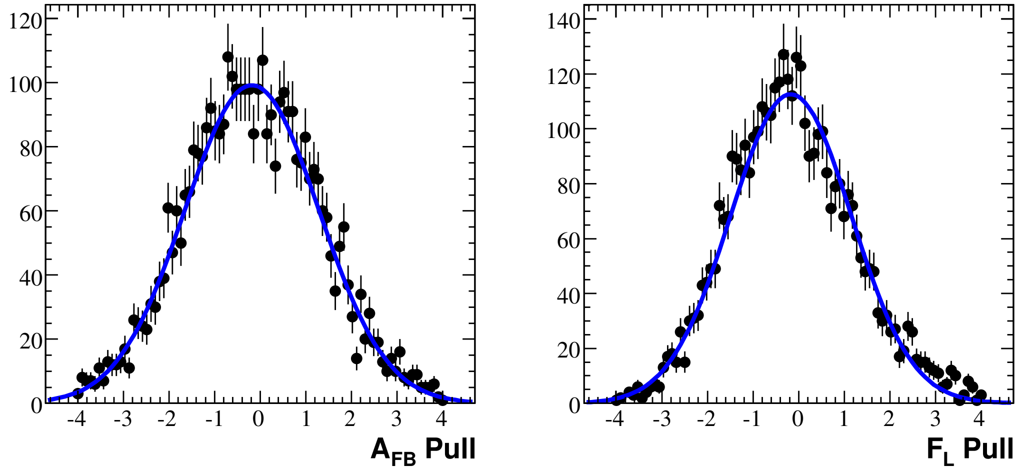

Figure 8.11: The pull on the fit for 1000 toy experiments for F_L and A_{FB}.

8.6 Summary

In this chapter the sensitivity to the measured forward-backward asymmetry and zero-crossing point in the decay $B_d \rightarrow K^{*0}\mu^+\mu^-$ that could be achieved with a nominal year of data has been evaluated. It has shown that by fitting the θ_L and θ_K angles simultaneously there is a large improvement in the error on the measured A_{FB} over what can be achieved by simply counting entries in the θ_L distribution. It is useful to compare the sensitivities quoted in Table 8.3 with the latest theoretical predictions [79],

$$q_0^2 = 4.39^{+0.38}_{-0.35}\,\mathrm{GeV}^2 \quad .$$

The central value has changed somewhat from the $q_0^2 = 4.0$ used in the LHCb MC. The uncertainty on the theory is comparable in size to the (statistical) error on the measured crossing point after one year. It should be noted that any systematic effects due to the choice of binning or the choice of sidebands (for the sideband subtraction) have not been evaluated. Systematic errors introduced by non-resonant $B_d \rightarrow K^+\pi^-\mu^+\mu^-$ [96] events (so far relegated to a footnote) will need to be assessed from the data and could potentially add difficulty to any measurement. However it should be noted that new physics models can look sufficiently different to the SM for LHCb to have sensitibity to new physics within one nominal year of data. Example models have already been presented in Fig. 2.8(a). Here the dashed lines represented Supersymmetric models that have different values of $\mathcal{C}_7$ through $\mathcal{C}_9$. It is even possible, for example if ($\mathcal{C}_7 = -\mathcal{C}_7^{SM}$), for there to be no zero-crossing point at all. This would be a clear departure from the SM.

Chapter 9

Summary and Conclusions

Three years ago the LHCb experimental hall was almost entirely empty, with the exception of the large dipole magnet described in Chapter 3. The hall is now a lot more crowded and the remaining components will be installed in the next few weeks. By the end of the year LHCb should have seen its first proton-proton collisions and the RICH detectors their first Cherenkov rings.

Commisioning the RICH detectors will undoubtedly be challenging but the results described in Chapter 6 (at the CERN SPS) are encouraging. They demonstrate that the RICH detectors can perform in a beam with a 25 ns time-structure, be successfully triggered and read out through the full LHCb computing chain at 1 MHz. Chapter 6 focused on estimating the photon detector and readout efficiency, which at 82% was marginally lower than predicted from laboratory measurements reported in Chapter 5. The second aim of the beam test was to measure the Cherenkov angle precision in the prototype RICH setup. This analysis was not carried out by the author and does not appear in this Thesis. A paper detailing both of the analyses will be released in the forthcoming months.

The beam tests were a culmination of a series of laboratory measurements that have been used to inform the description of the HPDs in the full LHCb simulation and in turn impact the particle ID performance in the MC simulation. The most significant additional information from these measurements was the sizeable increase in the image point spread (PSF) from the older 2004 detector simulation. The increase in PSF will have a small, detrimental, effect on the particle ID performance. Newer detector simulations should also include the reduced efficiency estimate from the beam tests, although this is more than compensated for by an increase in the HPD quantum efficiency in the later production HPDs. The hadronic particle ID provided by the RICH detectors is crucial for many of the precision analyses at LHCb including the flavour tagging of the $B_d \to K^{*0}\mu^+\mu^-$ decays described in this Thesis. All 484 HPDs are now produced, have been qualified through a series of tests similar to those in Chapter 5 and are now installed in the RICH detectors.

Chapters 7 and 8 describe an analysis to estimate the precision LHCb can achieve in measurements of $B_d \to K^{*0}\mu^+\mu^-$. This decay is particularly interesting to study at LHCb as it is a FCNC decay and cannot happen at tree level (highest order) in the SM. It must instead come through some higher order loop (penguin or box) process with a much smaller branching fraction ($\mathcal{O}(10^{-6})$). With no tree process to swamp any new physics contribution there could be a sizeable departure from the SM predictions. The new physics processes are necessarily loop order and can be visualised as replacing the virtual SM particles (the top quark, the W or Z in the loop) with one or more new physics particles. The angular distribution of particles in the decay probes the chiral structure of the new theory and can be particularly sensitive to right-handed currents that are highly suppressed in the SM. Measurements of this exclusive decay suffer from the usual problems of having a large theoretical uncertainty. Instead comparisons between the SM and data are made through asymmetries where the leading uncertainties can be cancelled. There are several observables that can be considered and these are listed in Chapter 2. The focus in this Thesis has been on the forward-backward asymmetry in the direction of the muons with respect to the B. This has good sensitivity to new physics and more importantly can be readily extracted at LHCb. Other asymmetries such as isospin asymmetries will be more challenging. The precision on the forward-backward asymmetry that can be achieved with a nominal year of data is comparable to the theory uncertainty on the SM prediction and much greater than achieved at *BABAR* and Belle (which are limited by statistics). This makes this measurement a promising probe for new physics at LHCb.

References

[1] G. Bertone, D. Hooper, and J. Silk, “Particle dark matter: Evidence, candidates and constraints”, *Phys. Rept.* **405** (2005) 279–390, `hep-ph/0404175`.

[2] A. D. Sakharov, “Violation of CP Invariance, C Asymmetry, and Baryon Asymmetry of the Universe”, *Pisma Zh. Eksp. Teor. Fiz.* **5** (1967) 32–35.

[3] C. S. Wu, E. Ambler, R. W. Hayward, D. D. Hoppes, and R. P. Hudson, “EXPERIMENTAL TEST OF PARITY CONSERVATION IN BETA DECAY”, *Phys. Rev.* **105** (1957) 1413–1414.

[4] J. H. Christenson, J. W. Cronin, V. L. Fitch, and R. Turlay, “Evidence for the $2\ \pi$ Decay of the K_2^0 Meson”, *Phys. Rev. Lett.* **13** (1964) 138–140.

[5] S. L. Glashow, J. Iliopoulos, and L. Maiani, “Weak Interactions with Lepton-Hadron Symmetry”, *Phys. Rev.* **D2** (1970) 1285–1292.

[6] W.-M. Yao *et al.*, “Review of Particle Physics”, *Journal of Physics G* **33** (2006).

[7] F. Halzen and A. D. Martin, “QUARKS AND LEPTONS: AN INTRODUCTORY COURSE IN MODERN PARTICLE PHYSICS”, Wiley, 1984.

[8] M. Kaku, “Quantum field theory: A Modern introduction”, Oxford Univ. Pr., 1993.

[9] M. E. Peskin and D. V. Schroeder, “An Introduction to quantum field theory”, Addison-Wesley, 1995.

[10] S. Weinberg, “A Model of Leptons”, *Phys. Rev. Lett.* **19** (1967) 1264–1266.

[11] A. Salam, “in Elementary Particle Theory”, Almqvist and Wiksell, Stockholm, 1968.

[12] P. W. Higgs, “Spontaneous Symmetry Breakdown Without Massless Bosons”, *Phys. Rev.* **145** (1966) 1156–1163.

[13] T. W. B. Kibble, “Symmetry breaking in non-Abelian gauge theories”, *Phys. Rev.* **155** (1967) 1554–1561.

[14] M. Kobayashi and T. Maskawa, “CP Violation in the Renormalizable Theory of Weak Interaction”, *Prog. Theor. Phys.* **49** (1973) 652–657.

[15] Z. Maki, M. Nakagawa, and S. Sakata, “Remarks on the unified model of elementary particles”, *Prog. Theor. Phys.* **28** (1962) 870.

[16] L. Wolfenstein, “Parametrization of the Kobayashi-Maskawa Matrix”, *Phys. Rev. Lett.* **51** (1983) 1945.

[17] Heavy Flavor Averaging Group (HFAG) Collaboration, E. Barberio *et al.*, “Averages of b-hadron properties at the end of 2006”, `hep-ex/0704.3575v1`.

[18] CKMfitter Group Collaboration, J. Charles *et al.*, “CP violation and the CKM matrix: Assessing the impact of the asymmetric B factories”, *Eur. Phys. J.* **C41** (2005) 1–131, `hep-ph/0406184`.

[19] CDF Collaboration, A. Abulencia *et al.*, “Observation of B_s anti-B_s oscillations”, *Phys. Rev. Lett.* **97** (2006) 242003, `hep-ex/0609040`.

[20] BABAR Collaboration, B. Aubert *et al.*, “Improved measurement of CP asymmetries in $B^0 \to (c\bar{c})K^{*0}$ decays”, `hep-ex/0607107`.

[21] Belle Collaboration, K. F. Chen *et al.*, “Observation of time-dependent CP violation in $B^0 \to \eta' K^0$ decays and improved measurements of CP asymmetries in $B^0 \to \phi K^0, K_S^0 K_S^0 K_S^0$ and $B^0 \to J/\psi K^0$ decays”, *Phys. Rev. Lett.* **98** (2007) 031802, `hep-ex/0608039`.

[22] BABAR Collaboration, B. Aubert *et al.*, “Observation of CP violation in $B^0 \to K^+\pi^-$ and $B^0 \to \pi^+\pi^-$”, *Phys. Rev. Lett.* **99** (2007) 021603, `hep-ex/0703016`.

[23] BABAR Collaboration, B. Aubert *et al.*, “Updated measurement of the CKM angle alpha using $B^0 \to \rho^+\rho^-$ decays”, `hep-ex/0607098`.

[24] Belle Collaboration, H. Ishino *et al.*, “Observation of Direct CP-Violation in $B^0 \to \pi^+\pi^-$ Decays and Model-Independent Constraints on ϕ_2”, *Phys. Rev. Lett.* **98** (2007) 211801, `hep-ex/0608035`.

[25] A. Somov *et al.*, “Measurement of the branching fraction, polarization, and CP asymmetry for $B^0 \to \rho^+\rho^-$ decays, and determination of the CKM phase phi(2)”, *Phys. Rev. Lett.* **96** (2006) 171801, `hep-ex/0601024`.

[26] BABAR Collaboration, B. Aubert *et al.*, “Measurement of the CKM angle gamma in $B^\pm \to D^* K^\mp$ decays with a Dalitz analysis of $D^0 \to K^0_S\pi^+\pi^-$ ”, `hep-ex/0607104`.

[27] BaBar Collaboration, B. Aubert *et al.*, “Measurement of CP violation parameters with a Dalitz plot analysis of $B^\pm \to D(\pi^+\pi^-\pi^0)K^\pm$”, *Phys. Rev. Lett.* **99** (2007) 251801, `hep-ex/0703037`.

[28] Belle Collaboration, A. Poluektov *et al.*, “Measurement of phi(3) with Dalitz plot analysis of $B^+ \to D^* K^{*+}$ decay”, *Phys. Rev.* **D73** (2006) 112009, `hep-ex/0604054`.

[29] A. J. Buras, “Weak Hamiltonian, CP violation and rare decays”, `hep-ph/9806471`.

[30] S. P. Martin, “A supersymmetry primer”, `hep-ph/9709356`.

[31] P. Ball *et al.*, “B decays at the LHC”, `hep-ph/0003238`.

[32] F. Kruger and J. Matias, “Probing new physics via the transverse amplitudes of $B^0 \to K^{*0}(\to K^-\pi^+)l^+l^-$ at large recoil”, *Phys. Rev.* **D71** (2005) 094009, `hep-ph/0502060`.

[33] P. Koppenburg, “Selection of $B^+ \to K^+\mu^+\mu^-$ at LHCb and sensitivity of R(K)”, April, 2007. CERN-LHCB-2007-034.

[34] G. Hiller and F. Kruger, “More model-independent analysis of $b \to s$ processes”, *Phys. Rev.* **D69** (2004) 074020, `hep-ph/0310219`.

[35] T. Feldmann and J. Matias, “Forward-backward and isospin asymmetry for $B \to K^* l^+l^-$ decay in the standard model and in supersymmetry”, *JHEP* **01** (2003) 074, `hep-ph/0212158`.

[36] “LHCb technical design report: Reoptimized detector design and performance”, 2003. CERN-LHCC-2003-030.

[37] "The LEP Design Report, Vol II: The LEP Main Ring", 1984. CERN-LEP-84-1.

[38] "LHC Design Report", 2004. CERN-LHCC-2004-3.

[39] M. Brice, "The first interconnection of the LHC. La première interconnection du LHC", May, 2005.

[40] E. Norrbin and T. Sjostrand, "Production and hadronization of heavy quarks", *Eur. Phys. J.* **C17** (2000) 137–161.

[41] E. Rodrigues, "The LHCb Kalman Fit", 2007. CERN-LHCb-2007-014.

[42] "LHCb: Vertex Locator technical design report", 2001. CERN-LHCC-2001-028.

[43] O. Callot *et al.*, "VELO tracking for the high level trigger", April, 2003. CERN-LHCb-2003-027.

[44] M. Brice, "Assembling the last module of the vertex locator for LHCb. Assemblage en salle propre de l'expérience LHCb du 42e et dernier module du VELO (Localisateur du vertex)", March, 2007.

[45] T. Versloot *et al.*, "Position reconstruction and charge distribution in LHCb VELO silicon sensors", December, 2007. CERN-LHCb-2007-119.

[46] "LHCb: Inner Tracker technical design report", 2003. CERN-LHCC-2003-009.

[47] "LHCb: Outer Tracker technical design report", 2001. CERN-LHCC-2001-041.

[48] G. W. van Apeldoorn, S. Bachmann, T. H. Bauer, E. Bos, Y. Guz, T. Haas, J. Knopf, J. Nardulli, T. Ketel, A. Pellegrino, T. Sluijk, N. Tuning, U. Uwer, P. Vankov, and D. Wiedner, "Beam Tests of Final Modules and Electronics of the LHCb Outer Tracker in 2005", Tech. Rep. LHCb-2005-076. CERN-LHCb-2005-076, CERN, Geneva, Oct, 2005.

[49] "LHCb: Magnet technical design report", 2000. CERN-LHCC-2000-007.

[50] M. Brice, "LHCb experiment magnets. Aimants de l'expérience LHCb", April, 2004.

[51] "LHCb: Calorimeters technical design report", 2000. CERN-LHCC-2000-049.

[52] "LHCb Trigger system technical design report", 2003. CERN-LHCC-2003-031.

[53] L. Fernández and P. Koppenburg, "Exclusive HLT Performance", Tech. Rep. LHCb-2005-047. CERN-LHCb-2005-047, CERN, Geneva, Mar, 2006. revised version submitted on 2006-08-09 12:16:25.

[54] TA2 Collaboration, M. Alemi *et al.*, "First operation of a hybrid photon detector prototype with electrostatic cross-focussing and integrated silicon pixel readout", *Nucl. Instrum. Meth.* **A449** (2000) 48–59.

[55] K. Wyllie *et al.*, "Front-end pixel chips for tracking in ALICE and particle identification in LHCb", Prepared for PIXEL 2002: International Workshop on Semiconductor Pixel Detectors for Particles and X-Rays.

[56] M. Adinolfi *et al.*, "The front-end (Level-0) electronics interface module for the LHCb RICH detectors", *Nucl. Instrum. Meth.* **A572** (2007) 689–697.

[57] B. G. Taylor, "TTC distribution for LHC detectors", *IEEE Trans. Nucl. Sci.* **45** (1998) 821–828.

[58] D. Breton and D. Charlet, "SPECS: the Serial Protocol for the Experiment Control System of LHCb", Tech. Rep. LHCb-2003-004, CERN, Geneva, Jan, 2003.

[59] S. Easo *et al.*, "Simulation of LHCb RICH detectors using GEANT4", *IEEE Trans. Nucl. Sci.* **52** (2005) 1665–1668.

[60] R. Forty and O. Schneider, "RICH pattern recognition", April, 1998. CERN-LHCb-98-040.

[61] N. Kanaya, G. Aglieri Rinella, T. Gys, D. Piedigrossi, and K. Wyllie, "Performance study of hybrid photon detectors for the LHCb RICH", *Nucl. Instrum. Meth.* **A553** (2005) 41–45.

[62] M. Moritz *et al.*, "Performance study of new pixel hybrid photon detector prototypes for the LHCb RICH counters", *IEEE Trans. Nucl. Sci.* **51** (2004) 1060–1066.

[63] S. Jolly, *Development of Ring Imaging Cherenkov Detectors for the LHCb Experiment.* PhD thesis, Imperial College London, June, 2004.

[64] "http://www.ni.com/labview/."

[65] C. Iselin, “Solution to Poisson’s or Laplace’s equations in Two-Dimensional Regions.” CERN-IT-ASD T604.

[66] G. Wendt, “SUR LE POUVOIR SEPARATEUR DU CONVERTISSEUR D’IMAGES A CHAMPS HOMOGENES ELECTORSTATIQUE ET MAGNETIQUE”, *ANNALES DE RADIOELECTRICITE* **39** (1955) 74–82.

[67] E. Darlington, “Backscattering of 10-100keV electrons from thick targets”, *J. Phys. D.* **8** (1975) 85–93.

[68] T. Tabarelli de Fatis, “Light spectra sum rule”, *Nucl. Instrum. Meth.* **A385** (1997) 366–370.

[69] S. M. Sze, “Physics of semiconductor devices”, Wiley, 2007.

[70] P. B. Coates, “The origins of afterpulses in photomultipliers”, *J. Phys. D.* **6** (1973) 1159–1166.

[71] P. B. Coates, “A theory of afterpulse formation in photomulitpliers and the prepulse height distribution”, *J. Phys. D.* **6** (1973) 1862–1869.

[72] V. O. Altermose, “Helium Diffusion through Glass”, *J. Appl. Phys.* **32** (1961) 1309–1316.

[73] G. Aglieri Rinella *et al.*, “Characterisation and compensation of magnetic distortions for the pixel Hybrid Photon Detectors of the LHCb RICH”, *Nucl. Instrum. Meth.* **A553** (2005) 120–124.

[74] J. McCarron, *Characterisation of Hybrid Photon Detectors for the LHCb and an analysis of the rare decay* $B_s^o \rightarrow \phi\phi$. PhD thesis, University of Edinburgh, 2007.

[75] M. Adinolfi *et al.*, “Performance of the LHCb RICH photodetectors in a charged particle beam”, *Nucl. Instrum. Meth.* **A574** (2007) 39–49.

[76] R. Jacobson, “The Final LHCb Readout Supervisor ‘ODIN”’, *8th Workshop on Electronics for LHC Experiments* (2001).

[77] H. W. Atherton *et al.*, “PRECISE MEASUREMENTS OF PARTICLE PRODUCTION BY 400-GeV/c PROTONS ON BERYLLIUM TARGETS”, CERN-80-07.

[78] “LHCb online system technical design report: Data acquisition and experiment control”, 2001. CERN-LHCC-2001-040.

[79] M. Beneke, T. Feldmann, and D. Seidel, “Systematic approach to exclusive $B \to Vl^+l^-, V\gamma$ decays”, *Nucl. Phys.* **B612** (2001) 25–58, `hep-ph/0106067`.

[80] C. Bobeth, T. Ewerth, F. Kruger, and J. Urban, “Analysis of neutral Higgs-boson contributions to the decays anti-$B_s \to l^+l^-$ and anti-$B \to Kl^+l^-$”, *Phys. Rev.* **D64** (2001) 074014, `hep-ph/0104284`.

[81] E. . Hewett, Joanne L. *et al.*, “The discovery potential of a Super B Factory. Proceedings, SLAC Workshops, Stanford, USA”, `hep-ph/0503261`.

[82] BABAR Collaboration, B. Aubert *et al.*, “Measurements of branching fractions, rate asymmetries, and angular distributions in the rare decays $B \to Kl^+l^-$ and $B \to K^*l^+l^-$”, *Phys. Rev.* **D73** (2006) 092001, `hep-ex/0604007`.

[83] A. Ishikawa *et al.*, “Measurement of forward-backward asymmetry and Wilson coefficients in $B \to K^*l^+l^-$”, *Phys. Rev. Lett.* **96** (2006) 251801, `hep-ex/0603018`.

[84] “LHCb computing technical design report”, 2005. CERN-LHCC-2005-019.

[85] T. Sjostrand *et al.*, “High-energy-physics event generation with PYTHIA 6.1”, *Comput. Phys. Commun.* **135** (2001) 238–259, `hep-ph/0010017`.

[86] D. J. Lange, “The EvtGen particle decay simulation package”, *Nucl. Inst. Meth.* **A462** (2001) 152–155.

[87] S. Agostinelli *et al.*, “GEANT4 a simulation toolkit”, *Nucl. Inst. Meth.* **A506** (2003) 250.

[88] A. Ali, P. Ball, L. T. Handoko, and G. Hiller, “A comparative study of the decays $B \to (K, K^*)l^+l^-$ in standard model and supersymmetric theories”, *Phys. Rev.* **D61** (2000) 074024, `hep-ph/9910221`.

[89] J. Dickens, V. Gibson, C. Lazzeroni, and M. Patel, “Selection of the decay $B_d \to K^{*0}\mu^+\mu^-$ at LHCb”, April, 2007. CERN-LHCB-2007-038.

[90] H. Skottowe and M. Patel, “$B_d \to K^{*0}\mu^+\mu^-$ Selection.” http://indico.cern.ch/conferenceDisplay.py?confId=34251, 2008. Talk given at internal working group meeting.

[91] H. Skottowe and M. Patel, “Selection of $B_d \to K^{*0}\mu^+\mu^-$ in DC06.” http://indico.cern.ch/conferenceDisplay.py?confId=26408, 2008. Talk given at internal working group meeting.

[92] I. Dunietz, H. R. Quinn, A. Snyder, W. Toki, and H. J. Lipkin, “How to extract CP violating asymmetries from angular correlations”, *Phys. Rev.* **D43** (1991) 2193–2208.

[93] BABAR Collaboration, B. Aubert *et al.*, “Measurement of decay amplitudes of $B \to (c\overline{c})K^*$ with an angular analysis, for $(c\overline{c}) = J/\psi$, $\psi(2S)$ and χ_{c1}”, `hep-ex/0607081`.

[94] Verkerke, W. and Kirkby, D., “The RooFit Toolkit for Data Modeling”, in *Statistical Problems in Particle Physics, Astrophysics and Cosmology*, Lyons, L. and Karagöz Ünel, M., ed., pp. 186–+. 2006.

[95] R. J. Barlow, “Statistics: A Guide to the Use of Statistical Methods in the Physical Sciences”, Wiley, 1989.

[96] B. Grinstein and D. Pirjol, “Factorisation in $B \to K\pi\ell^+\ell^-$ decays”, *Phys. Rev.* **D73** (2006) 094027, `hep-ph/0505155`.